RUPRECHT-KARLS-UNIVERSITÄT HEIDELBERG

Christian Rumpf

New minimally-invasive laser treatment in orthopaedics on spinal deformations and bone tumours

Dissertation

HD-KIP-01-12

KIRCHHOFF-INSTITUT FÜR PHYSIK

Dissertation
submitted to the
Combined Faculties of the Natural Sciences and for Mathematics
of the Rupertus Carola University of
Heidelberg, Germany
for the degree of
Doctor of Natural Sciences

New minimally-invasive laser treatment in orthopaedics on spinal deformations and bone tumours

presented by

Diplom-Physicist: Christian Rumpf
born in: Groß-Umstadt, Germany

Heidelberg, 31/01/2001

Referees: Prof. Dr. Josef F. Bille
Prof. Dr. Wolfgang Schlegel

Abstract

Three completely new, minimally-invasive laser operation techniques were developed and extensive investigations were carried out for a clinical application in orthopaedics. With a focus on laser tissue interactions, this work covers a broad range of different applications from cw to femtosecond laser systems. Throughout this work, the emphasis was put on laser tissue interaction and the optimisation of laser parameters with regard to safety and efficiency. Two effects, laser ablation and laser coagulation, were investigated with regard to minimal thermal damage to collateral structures.

The main part was the development of a completely new laser-induced operation technique for the minimally-invasive treatment of spinal deformities in young patients. The method is based on endoscopic laser treatment with an anterior (thoracoscopic) surgical approach. During extensive in vivo experiments, the Ho:YAG laser proved to be a powerful tool for the precise, fast and effective ablation of cartilage tissue and, thus, a new gentle operation technique for the treatment of idiopathic scoliosis. In 75% of all cases, the desired effect of inhibiting growth on one side, i.e. the side with laser hemiepiphysiodesis, could be achieved.

In a second application, experiments with a picosecond and a femtosecond-laser system showed that plasma-mediated tissue ablation of cortical bone is possible with sufficiently high ablation rates and accuracy for the clinical application of microsurgical treatment. In comparison with longer picosecond laser pulses from the Nd:YAG laser, the ablation with the Ti:Sapphire femtosecond pulses was found to be more efficient.

In a third application, we demonstrated the feasibility of laser-induced interstitial thermotherapy (LITT) of bone tissue as a minimally-invasive treatment of bone tumours (osteoid osteoma). After evaluating three lasers (Ho:YAG, Nd:YAG and diode (λ = 940 nm)), we found that thermal penetration and, thus, coagulation of bone tumours is possible for tumour sizes up to 2 cm.

New fast magnetic resonance imaging (MRI) sequences for online temperature monitoring were developed in cooperation with the German Cancer Research Centre. Measurements showed that the T_1-method is the most reliable method, although results from the diffusion method and the PRF (proton resonance frequency) are more sensitive. The results demonstrated that visualization and control of the heating procedure during LITT as well as data acquisition is possible within 1.5 seconds.

Contents

List of Figures

List of Tables

Chapter 1

Introduction

Along with the efforts of clinics and physicians to reduce the costs of medical care, new operation techniques have to be found that allow for an effective treatment with short operation times and fast mobilization, so as to minimize the need for intensive aftercare. One way to achieve this goal is to use minimally-invasive operation techniques that, in contrast to conventional methods, result not only in faster mobilization of the patients and, thus, shorter hospitalization times, but also provide much better cosmetic results and reduce pain. Although a variety of endoscopic treatments have been carried out for many years already, thoracoscopic surgery on the spine is a fairly new operation technique. With the advent of video technology, thoracoscopy offers a minimally-invasive operative approach to accomplish thoracic surgical procedures previously performed through open techniques [Kee93].
Another aspect is the clinical application of laser light in the treatment of a broad number of diseases. Apart from technical improvements with regard to reliability and laser size as well as application devices such as fibres, articulated mirror arms or endoscopic systems, the number of clinical laser applications has increased immensely during the last few years. Nowadays, there are a vast number of applications for almost any region of the body, where a laser-based treatment is superior to conventional methods. Significant advances in laser technology have also been important in the growing use of video-assisted thoracic surgery (VACS).

In bringing these two aspects together, i.e. combining endoscopic surgery and high-tech laser applications, a variety of new, powerful clinical applications are opened up. Focussing on the physics of laser-tissue interaction, this work presents three completely new clinical applications of minimally-invasive laser treatment.

The main emphasis was put on the development of a new laser based operation technique for the minimally-invasive treatment of spinal deformities in young patients (*idiopathic scoliosis*[1]). This study is a product of the cooperation between the Kirchhoff-

[1]The term "scoliosis" was first used by Galen (AD 131-201) in "De moto maerculorum", although spinal deformation was previously described by Hippocrates 470 BC.

Institute of Physics and the Orthopaedic Clinic, both of the University of Heidelberg, Germany.

1 to 3% of young people develop idiopathic scoliosis due to a malfunction in spinal growth which results in an extreme curvature of the spine to one side mostly accompanied by a rotation of the spine. In contrast to the existing treatment, in which bolts and rods are fixed inside the vertebral bodies to apply a mechanical strength, our aim is to treat these patients using a laser to remove the epiphyseal cartilage of the vertebra.
The method focusses on minimally-invasive endoscopic laser treatment using an anterior (thoracoscopic) surgical approach. It is known that an early partial ablation of the epiphyseal growth plate (*hemiepiphysiodesis*) over several vertebrae can cause scoliotic growth [Bis40] [Can79] [Haa39] [Pac39] [Roa60]. Furthermore, in 1924 Wittek first showed on young scoliotic patients with sufficient growth potential that a hemiepiphysiodesis on the **convex** side of the curvature over several vertebrae resulted in a straightening of the spine [Wit24].
In contrast to Wittek, who used mechanical instruments (chisel) to remove the epiphyseal growth plate in open surgery, our new method is based on precise minimally-invasive laser ablation. Therefore, the aim of this work is to show that our treatment model is capable of inducing a change in spinal growth, i.e. of producing a scoliosis. Hence, if laser hemiepiphysiodesis on the spine is capable of inducing such a scoliotic growth, the opposite, i.e. **laser ablation** on the **convex side** over several vertebrae in young patients with **sufficient growth potential**, should result in a straightening of the spine.

In chapter 5, the complete development from a preliminary evaluation of different laser systems (see section 5.3) to an application on animals (foxhounds) is described. The aim of the initial evaluation was to find a suitable laser which met all of the requirements for effective clinical treatment with maximum safety for the patient producing **less pain** and **excellent cosmetic results** and, thus, allowing a **faster mobilization** and shorter hospitalization.

Whereas laser hemiepiphysiodesis with the Ho:YAG laser is based on the rapid evaporation of the water inside the tissue, other mechanisms of laser-tissue interaction, such as plasma-induced tissue ablation, offer a new field of clinical applications based on very precise ablation, such as photo-refractive surgery on the cornea of the eye [Bil97],[Mül97],[Lub99], glaucoma treatment [Keß00] or ablation of neural tissue [Göt96]. Since plasma-mediated laser ablation is capable of removing only small volumes of tissue, its application in clinical treatment has been limited until now. However, due to the development of new powerful pico- and femtosecond laser systems, the number of applications is increasing. Another advantage of plasma-mediated ablation is the independence of tissue structure. Therefore, even hard tissue like cortical bone can be removed easily using this technique. In chapter 6, the main interest lies in the clinical application of **laser-micro-surgery** (LMS) used for the treatment of stenosis on vertebral foraminae and necrosis of the head of femur [Bon99]. For these applications, precision in tissue

ablation and non-thermal laser-tissue interaction are essential requirements, whereas the ablation rate itself is of secondary importance.
Two powerful ultra-short-pulse laser systems were compared with regard to their ablation rates and precision of plasma-mediated ablation of cortical bone tissue (bovine thigh bone). This is the first evaluation of plasma-mediated ablation of bone tissue, which allows for very clean and well-defined removal of tissue without evidence of thermal or mechanical damage to collateral structures.

Another rapidly growing field of clinical laser applications is the minimally-invasive treatment of tumours.
Chapter 7 describes the first experiments towards a clinical application of a new minimally-invasive laser treatment of benign bone tumours. It is the first work which uses online MRI temperature monitoring for the laser-induced interstitial thermotherapy (LITT) of bone tissue.

There are many types of benign and malignant bone tumours of which the **osteoid osteoma** (OO) is the most common of the benign ones.
To date, only one research group is known to use LITT as a treatment for OO [Gan98]. Their method is based on the inactivation of the tumour cells with laser photo-coagulation, using a bare fibre and thereby destroying all tumour cells without the removal of bone tissue. The necrotic cells are absorbed and replaced with new bone cells (osteocytes). They use computer tomography (CT) for intra-operative guidance, which exposes the patient to additional radiation. In addition, online temperature monitoring is not possible using this technique.
The aim of our new laser treatment was to inactivate the OO by the photo-coagulation of the tumour (nidus) using a laser fibre and thereby destroying all tumour cells without removal of bone tissue.
During the study, 3 different laser systems including a Nd:YAG laser, a Ho:YAG laser and a compact diode laser (λ = 940 mn) were evaluated with regard to their suitability for LITT. A new fully MR compatible puncture system was developed to facilitate the puncture of the nidus and assure precise needle placement,.
Nowadays, magnetic resonance imaging (MRI) is one of the most important tools in clinical diagnostics. It allows for non-invasive investigation of anatomical structures with a very high spatial resolution and excellent soft tissue contrast. Images of any orientation within the whole body can be acquired. New fast imaging techniques and the improvement of contrast medium have led to a vast range of new MRI applications such as MR angiography [Boc00], investigation of brain function and perfusion, MR urography [Sch93] and MR pulmonary imaging [Bac96].
Our newly invented minimally-invasive laser treatment of OO is performed under MRI guidance and uses the latest imaging technique for fast non-invasive online temperature control of the coagulation process. This allows for a precise puncture of the tumour and safe laser treatment with the possibility of stopping the laser if the tumour volume has been coagulated, thus, avoiding thermal damage to collateral healthy structures.

Non-invasive MR temperature imaging is based on a change in the parameters T_1 (relaxation time), D (diffusion coefficient) or PRF (proton resonance frequency).

Chapter 2

Fundamentals of laser-tissue interaction

The crucial issue for all clinical laser applications is the medical indication and the expected benefit. Therefore, knowledge of how laser light interacts with different types of biological tissue is the key to finding new and effective applications for lasers in medicine. Along with technical improvements in reliability and size, and application devices such as fibres, articulated mirror arms or endoscopic systems, the number of clinical laser applications has increased immensely in the last few years. Today, laser-tissue interactions are the subject of many investigations in almost all types of tissue. This chapter gives an overview of the different aspects of laser-tissue interaction. The emphasis thereby is put on thermal laser-tissue interactions, since most of the clinical laser applications presented in this work are based on this type of interaction. For a deeper insight to the field of laser-tissue interaction, reference should be made to [Bou86][Nie96].

2.1 Classification

The variety of interaction mechanisms that occur when applying laser light to biological tissue is manifold. Specific tissue characteristics as well as laser parameters contribute to this diversity. The most important optical tissue properties are the coefficients of reflection, absorption and scattering, as well as heat conduction and heat capacity. On the other hand, the laser parameters such as wavelength, pulse duration, pulse energy and spot size determine the kind of interaction. Among these, the exposure time is a very important parameter when selecting a certain type of interaction.
In 1986 Boulnois presented a classification of four different types of laser-tissue interaction, which has been accepted ever since [Bou86]. He distinguishes *photochemical interactions*, *thermal interactions*, *photoablation* and *plasma-induced ablation (photodisruption)*. Fig. 2.1 shows a double logarithmic map with the different interaction types as a function of pulse duration (*irradiance*) and power density. According to this chart, the different interaction mechanisms are connected to certain time scales: continuous wave or exposure times $>$ 1 s for *photochemical interactions*, 1 min down to 1 μs for *thermal interactions*,

1 μs down to 1 ns for *photoablation*, and < 1 ns for *plasma-induced ablation* (*photodisruption*). However, adjacent interaction types cannot always be strictly separated. In addition to characterization concerning irradiance and power density, the wavelength of the laser light is also very important for interaction mechanisms. Lasers operating in the near infrared (NIR) at wavelengths between 700 and 1100 nm are characterized by their applicability in the so called "therapeutic window". At these wavelengths, most types of tissue have high transmission rates, thus, laser photons can penetrate deep into the tissue. The high water content of soft tissue is a decisive factor for the low absorption coefficient, since water has a low absorption coefficient in this wavelength interval (fig. 2.2).

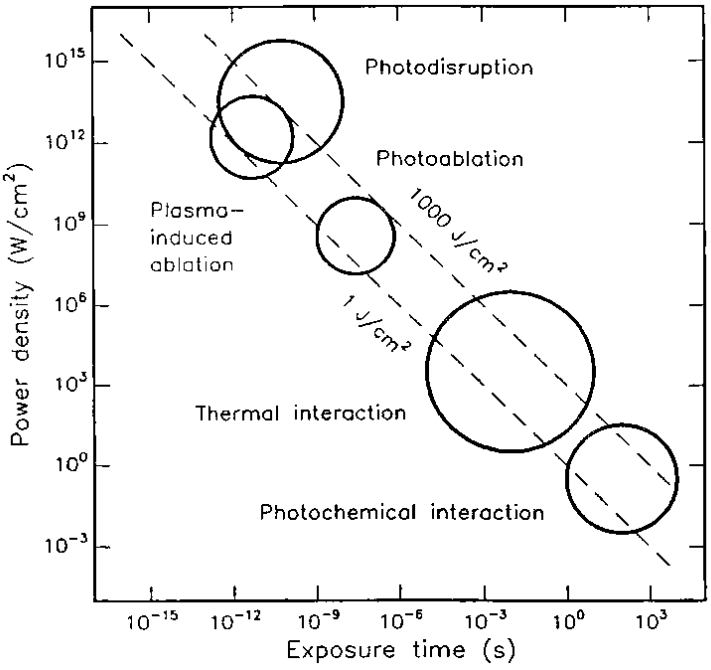

Fig. 2.1: Classification of laser-tissue interactions with respect to pulse duration and power density [Nie96].

Photochemical interaction takes place at very low power densities (typically 1 W/cm^2) and during long exposure times ranging from seconds to continuous wave. This field of clinical laser applications such as *photodynamic therapy* and *biostimulation*, - mostly using dye lasers, which can be adjusted to the optimum wavelength,- has expanded over the last few years, especially in the field of cancer treatment, due to the development of new efficient photosensitizers [Dou83]. Photochemical laser-tissue interaction and photoablation are not part of this work. A detailed description can be found in [Nie96].

2.2 Thermal interaction

The majority of the therapeutic use of lasers in medicine is in the field of thermal applications. A detailed overview of thermal laser application is given in [Ber92]. The term "thermal interaction" denotes a variety of processes that lead to a local rise in temperature depending on the tissue parameters, as well as on the laser wavelength, pulse duration and power density. Typical power densities are in the range of 10 - 10^6

W/cm^2 with pulse durations of 1 μs to a few minutes.
At a microscopic level, the photothermal effect originates from the transfer of electromagnetic energy to thermal energy i.e. molecular vibration and rotation bands inside the tissue. This can be expressed as a two-step process. Firstly, the absorption of a photon with an energy $h\nu$ promotes the molecule A to an excited state A*:

$$h\nu + A \rightarrow A^*, \tag{2.1}$$

then secondly, inelastic collisions with the adjacent molecule B lead to the deactivation of A* and a simultaneous increase of the kinetic energy of B:

$$A^* + B(E_{kin}) \rightarrow A + B(E_{kin} + \Delta E_{kin}) \tag{2.2}$$

The kinetic energy of biomolecules at room temperature is about 0.025 eV, whereas thermal lasers such as the CO_2 laser ($\lambda = 10.6\ \mu m$) have a photon energy of 0.117 eV i.e. five times higher. The Argon-ion laser ($\lambda = 514$ nm) has a photon energy of 2.4 eV i.e. almost 100 times higher. Therefore, laser energy can be absorbed only due to the extremely high number of vibrational and rotational bands of biomolecules (10^3 to 10^5) and the high cross section for the collision (10^{-18} cm^2 to 10^{-17} cm^2) of the excited state A*.

The spatial extent and degree of tissue damage depends primarily on magnitude, exposure time, and placement of deposited heat inside the tissue. The deposition of laser energy, however, is not only a function of laser parameters, but also depends strongly on optical tissue parameters such as *absorption* and *scattering coefficients*, *heat capacity* and *thermal conductivity*.

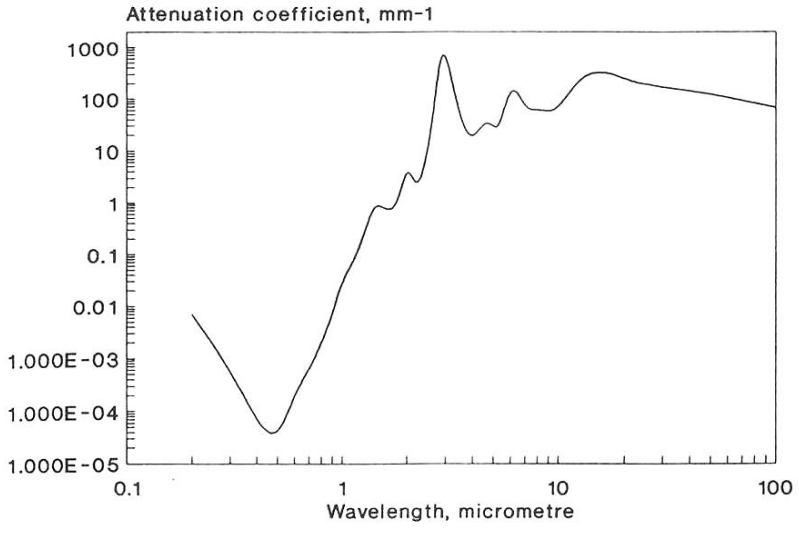

Fig. 2.2: Optical absorption coefficient α for water from 200 nm to 100 μm [Duc90]. Note the low absorption coefficient for the wavelengths between 700 and 1100 nm ("therapeutic window").

In most biological tissue, absorption is mainly due to the presence of free water molecules, pigments (e.g. melanin) and proteins. The optical absorption coefficient of water is plotted in fig 2.2. It can be seen that, toward the IR range of the spectrum, absorption increases by several orders of magnitude (logarithmic scale) with a peak at about 3 μm. It originates from symmetric and asymmetric vibrational modes of the water molecule [Poh76] with resonance frequencies at $1.13 \cdot 10^{14}$ and $1.08 \cdot 10^{14}$ respectively. Thus, the family of Er^{3+} doped lasers (Er:YAG at 2.94 μm, Er:YLF at 2.8 μm and Er:YSGG at 2.79 μm) is a typical thermally-acting laser with a very high ablation power on the tissue surface due to strong absorption, but with low penetration depth. The Ho:YAG laser at 2.12 μm also matches an absorption peak of water, although its interaction properties are somewhat different to the Er:YAG laser (see section 5.5.1).

2.2.1 Heat generation

Deposition of heat in the tissue for in vitro studies is due only to light absorbed according to *Lambert-Beer's law*

$$I = I_0 \, exp\{-\mu_\alpha(\lambda) z\} \tag{2.3}$$

with the penetration depth $d(\lambda)=\mu_\alpha(\lambda)^{-1}$.

For a light flux in z-direction in a non-scattering medium, the local heat deposition per unit area and time in a thickness Δz is given by

$$S(r,z,t) = \frac{I(r,z,t) - I(r,z+\Delta z,t)}{\Delta z} \quad \left[\frac{W}{cm^3}\right] \tag{2.4}$$

and with $\Delta z \to 0$,

$$S(r,z,t) = -\frac{\delta I(r,z,t)}{\delta z} = \mu_\alpha(\lambda) I(r,z,t) \tag{2.5}$$

Since μ_α is strongly wavelength-dependent, the same applies for S.

If scattering is taken into account, *Lambert-Beer's law* has to be modified by

$$I(r,z) = I_0(r,z) \, exp\{-\mu_t z\} \tag{2.6}$$

with the total attenuation coefficient $\mu_t = \mu_a + \mu_s$ and the scattering coefficient μ_s. The *optical penetration depth* is then given by

$$d = (\mu_t)^{-1} \tag{2.7}$$

Although this simple approach is a good approximation for a collimated laser beam, this model can no longer be applied to many applications using fibre optics or special laser applicators with diffusing distal tips, as used in LITT.

If phase transitions do not occur, an alternation in heat content dQ induces a linear change in temperature dT according to a basic law of thermodynamics

$$dQ = m\,c\,dT \tag{2.8}$$

where m is the mass and c is the specific heat capacity in units of $\mathrm{kJ\,kg^{-1}\,K^{-1}}$. During thermal laser therapy, the main cause of the resulting tissue damage is the heat transport. There are losses based on either *heat conduction*, *heat convection* or *heat radiation* [Ada88]. The latter is described by *Stefan-Boltzmann's law*, which states that the radiated power is related to the fourth power of temperature. Due to the moderate temperature achieved in most laser-tissue interactions, and the much higher heat transfer rates from convection and conduction, heat radiation can be neglected. Nevertheless there are LITT simulations which take heat radiation into account [Stu95].

2.2.2 Heat transport

Heat conduction is the primary mechanism by which heat is transferred to adjacent tissue structures. With the temperature conductivity defined by

$$\kappa = \frac{\lambda}{\rho c} \qquad \left[\frac{m^2}{s}\right] \tag{2.9}$$

where λ is the heat conductivity in units of $[\mathrm{Wm^{-1}K^{-1}}]$, ρ is the density and c is the specific heat capacity in units of $[\mathrm{kJkg^{-1}K^{-1}}]$, heat conduction can be derived using the inhomogeneous *heat conduction equation*

$$\dot{T} = \kappa \Delta T + \frac{1}{\rho c} S(r, z, t) \tag{2.10}$$

with an additional heat source S(r,z,t) [Wm^{-3}] which represents the sum of the outer heat density from laser radiation (equation 2.5) and the inner heat produced by the body cells (metabolic heat). The latter can be neglected in comparison with the externally applied heat during thermotherapy and is zero for in vitro applications.
The solution of the inhomogeneous heat equation depends strongly on the temporal and spatial dependencies of S(r,z,t). An analytical solution can be derived if the heat source function S(r,z,t) is approximated by a point source $S(z,t) = S_0\delta(z-z_0)\delta(t-t_0)$. In this case, the inhomogeneous differential equation (equation 2.10) can be solved using the theory of *Green's function* [Hon95], which is given by

$$G(z-z_0, t-t_0) = \frac{1}{\sqrt{4\pi\kappa(t-t_0)}}\, exp\left\{-\frac{(z-z_0)^2}{4\kappa(t-t_0)}\right\} \tag{2.11}$$

Using this function, the solution is determined by

$$T(t,z) = \frac{S_0}{\rho c}\frac{1}{(4\pi\kappa t)^{3/2}}\, exp\left\{-\frac{z^2}{4\kappa t}\right\} \tag{2.12}$$

It is possible to derive the spatial extent of heat transfer by the time-dependent *thermal penetration depth* from this

$$z_{therm}(t) = \sqrt{4\kappa t} \tag{2.13}$$

The term "thermal penetration depth" originates from the argument of the exponential function in equation 2.11. Thus, z_{therm} is the distance in which the temperature has decreased to 1/e of its peak value. In water, heat diffuses by approximately 0.7 mm in 1 s. In cortical bone tissue, $z_{therm} \approx 0.9$ mm for t = 1 s.
The *thermal relaxation time* is obtained by equating the optical penetration depth d as defined by equation 2.7 to the thermal penetration depth z_{therm}, hence

$$\tau_{therm} = \frac{d^2}{4\kappa} \tag{2.14}$$

During thermal decomposition, τ_{therm} becomes very important since it measures the thermal susceptibility of the tissue. For laser pulse durations, $\tau < \tau_{therm}$, i.e. for short pulse lasers, heat does not even diffuse to the distance given by the optical penetration depth *d*. Hence, thermal damage to non-decomposed tissue is negligible (see chapter 6). For $\tau > \tau_{therm}$, i.e. for cw-mode lasers, heat can diffuse to a multiple of the optical

penetration depth, i.e. thermal damage to tissue adjacent to the decomposed volume occurs. In this case, the solution to the inhomogeneous heat conduction equation 2.10 cannot be given analytically, but must be derived numerically, for instance, by using the *finite difference method* or *recursion algorithms*. Detailed simulations were performed in [Wei84], [Rog93], [Ols98] and [Kli99]. According to equation 2.14, the wavelength-dependence of d^2 is transferred to τ_{therm}. Figure 2.3 shows the thermal relaxation times for water calculated from fig. 2.2 and equation 2.14. The shortest relaxation time of approximately 1 μs occurs for the absorption peak at 3 μm. This value is also referred to as the "1 μs rule" stating that lasers operating at a pulse duration $\tau < 1\,\mu s$ should cause no thermal damage in the tissue. This applies for most types of tissue apart from tissue with a low water content. Thus, cortical bone has to be regarded differently (see section 4.3).
For cortical bone tissue, the thermal relaxation time can be estimated at $1.2 \cdot 10^5\,\mu s$ [Cha90].

A high repetition rate of the laser pulses, however, can lead to an additional increase in temperature if the rate of heat transport is less than the rate of heat generation. This is an important aspect, especially for tissue with low thermal conductivity such as cortical bone ($\lambda = 0.3$ $\mathrm{Wm^{-1}K^{-1}}$).

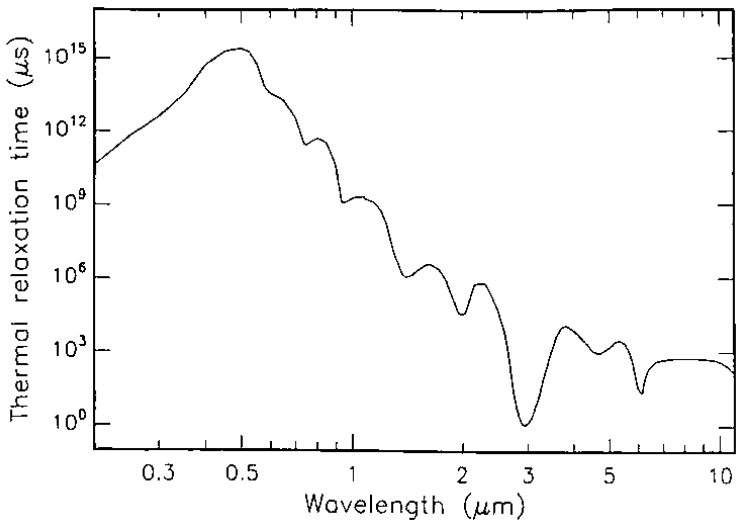

Fig. 2.3: Thermal relaxation times of water according to [Nie96].

During in vivo experiments, a major part of heat convection in tissue is heat transfer due to blood flow. In addition, during minimally invasive clinical laser applications, irrigation plays an important role with regard to heat convection. These two effects may vary during treatment and are, therefore, difficult to describe. Only for blood flow through capillaries, which can be estimated as nearly constant, can heat convection be considered as an additional term in the heat conduction equation leading to

$$\dot{T} = \kappa \Delta T + \frac{S}{\rho c} + \frac{v_b \rho_b c_b}{\rho c}(T_b - T) \tag{2.15}$$

equation 2.15 is called the **"bioheat-transfer-equation" (BHTE)**. The index b refers to the blood with v_b as the blood flow rate [s^{-1}]. In this approximation, it is assumed that all capillaries have the same parameters. For larger vessels, however, the heat transfer equation has to be solved separately for every sort of tissue (vessels, normal tissue) considering the corresponding boundary conditions [Wym95].

2.2.3 Heat effects

The first mechanism by which tissue is thermally affected can be attributed to conformational changes in the molecules. These effects, accompanied by bond destruction and membrane alternations, are summarized in the term "*hyperthermia*" ranging from 42°-50°C. If hyperthermia lasts for several minutes, a significant percentage of tissue will undergo necrosis[1] as described by the *Arrhenius formalism* [Nie96]. A measurable reduction in enzyme activity is observed beyond 50°C, resulting in a reduced energy transfer within the cell, immobility and a disturbance in the cell's repair mechanisms. At 60°C, denaturation of proteins and collagen occurs, which leads to coagulation of tissue and necrosis of cells (tissue paling). At even higher temperatures (>80°C), membrane permeability is drastically increased, thereby destroying the otherwise maintained chemical concentrations. At 100°C, water molecules start to vaporize. The large vaporization heat of water (2257 kJ/kg) is advantageous since the vapour generated carries away excess heat and helps to prevent any further increase in the temperature in adjacent tissue. Due to the large increase in volume, gas bubbles are formed inducing mechanical ruptures and thermal decomposition of the tissue fragments (see section 5.5.1). If all of the water has been vaporized the increase in temperature proceeds. In excess of 150°C, carbonization occurs, which can be seen by the blackening of the tissue and the escaping of smoke. However, the tissue may be cooled with water or gas to avoid carbonization, [Iva98][Sch92]. Beyond 300°C, melting occurs depending on the target material (see chapter 4.3).
The exact temperature for the onset of cell necrosis is rather difficult to determine in general. In addition, not only the temperature reached, but also the duration of this temperature is essential for the induction of irreversible tissue damage (see fig. 2.4). Of course, these values vary between the different sorts of tissues. According to Lundskog [Lun72] and Tillotson [Til89], irreversible necrosis of bone cells (osteocytes) can be achieved with a temperature exceeding 50°C over a period of at least 30 seconds.

Due to heat diffusion and other effects, no constant temperature profile is achievable within the tissue sample. Thus, during laser treatment, several thermal effects coincide at

[1] Morphological changes that occur after the breakdown of cell functions (cell death). Depending on localization and the extent of the necrosis, there might be healing (restitutio ad integrum), development of a scar or a pseudocyst.

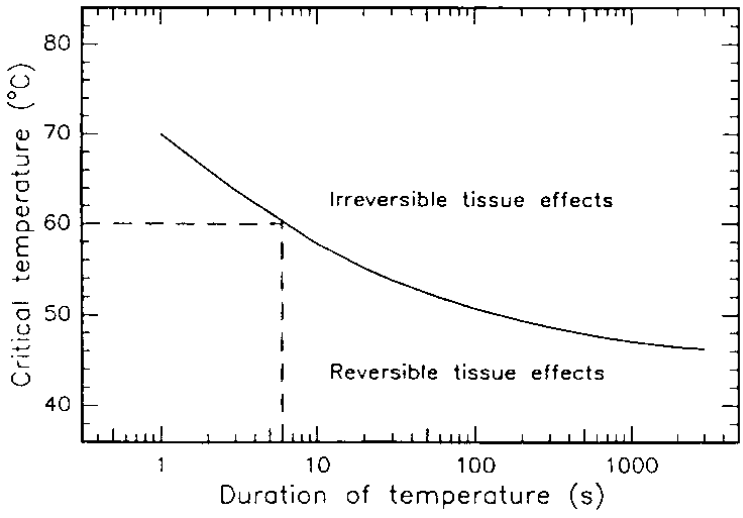

Fig. 2.4: Critical temperatures for the occurrence of cell necrosis [Nie96].

different depths resulting in a temperature gradient as shown in fig. 2.5 for a collimated laser beam.

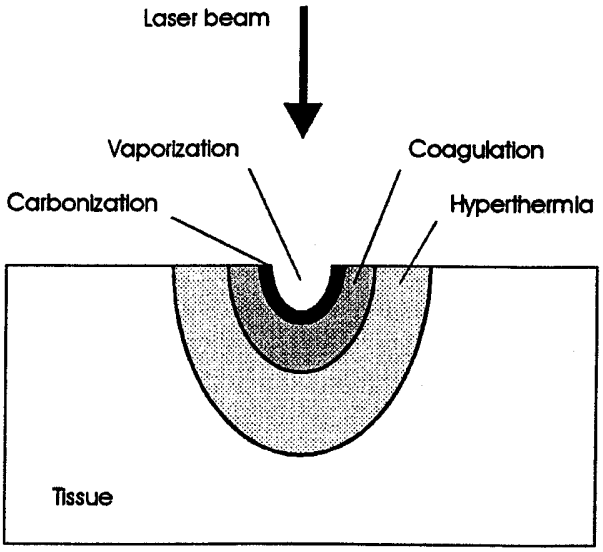

Fig. 2.5: Location of different thermal effects inside biological tissue [Nie96].

2.2.4 Laser-induced interstitial thermotherapy (LITT)

The principle idea of LITT is to position an appropriate laser applicator inside the tissue to be coagulated, e.g. a tumour, and achieve necrosis by heating the cells. The most common lasers for LITT are either Nd:YAG lasers at 1064 nm or different types of diode lasers at 800-920 nm since light penetrates deep into tissue at these wavelengths (see fig. 2.2). Typical parameters of the procedure are 1-5 W of cw laser power for a period of several minutes. The spatial extent of the damage zone depends primarily on laser power, laser exposure, geometry of the laser applicator, and thermal and optical tissue properties. At the start of an LITT procedure, the catheter is placed inside the tumour with the assistance of either ultrasound, computer tomography (CT) or magnetic resonance imaging

(MRI).
The whole procedure can be performed either intra-operatively or percutaneously as done in this work for the treatment of bone tumours (see chapter 7). If no online temperature monitoring is provided, the treatment should be preceded by suitable irradiation planning using input parameters like extent, topology and blood flow as well as optical and thermal tissue parameters. Although computer simulations might lead to a result in agreement with the initial tissue properties, during the process of coagulation, the optical properties of the tissue change leading to higher scattering, but nearly the same absorption. Therefore, direct temperature monitoring is much more precise and allows the physician to react and, if necessary stop the laser treatment immediately. Using new ultrafast MRI sequences, online temperature monitoring becomes an important tool during LITT. The minimally-invasive treatment of bone tumours described in chapter 7 is the first work that uses online MRI temperature monitoring for LITT of bone tissue.

2.3 Plasma-induced interaction

If power densities on the tissue surface exceed 10^{11} W/cm^2 (10^{14} W/cm^2 in air), a plasma, i.e. a highly ionized state, is induced. This phenomenon is also called *optical breakdown*. It is accompanied by a sudden adiabatic rise in temperature to values of up to a few 1000 K. Very clean and well-defined removal of tissue without evidence of thermal or mechanical damage can be achieved by means of plasma-induced ablation if the appropriate laser parameters are chosen.
The most important parameter of plasma-induced ablation is the local electric field strength **E**. If it exceeds a certain threshold value, it forces the ionization of molecules and atoms. Typical values are approximately 10^7 V/cm, which is comparable to the average atomic or intramolecular *Coulomb* electric field. The initiation of plasma generation can be twofold [Pul84]; with pulses in the nanosecond range, e.g. generated by a Q-switched laser, the tissue initially heats up to more than 1000 K leading to thermal ionization (*thermionic emission*) with high plasma temperatures often accompanied by non-ionizing side effects. In mode-locked laser pulses, i.e. pulse durations in the picosecond and femtosecond range, the high photon density allows coherent absorption of several photons, which provides enough energy for ionization (*multi-photon ionization*). In either case, a few so called "lucky" electrons absorb energy from the photon in the presence of an atom and accelerate (*inverse Bremsstrahlung*[2]). The accelerated electrons collide with other atoms and ionize them, thereby initiating an avalanche effect. Within a few picoseconds, the plasma is formed leading to electron densities of typically 10^{21} cm^{-3}.
From the mathematical model [Nie96] using *Maxwell's equations* and equation 2.3, the absorption coefficient α_{pl} is a non-linear function of the free electron density

[2]In ordinary "Bremsstrahlung", the opposite occurs, i.e. electrons are accelerated in the electromagnetic field of an atom thereby emitting radiation.

$$\alpha_{pl} \sim N^2 \tag{2.16}$$

The condition for plasma growth and sustainment is that losses - such as inelastic collisions and free electron diffusion - do not quench the avalanche process. The critical density N_{crit}, at which a net amount of energy is not converted to plasma energy any further, is reached when the plasma frequency becomes equal to the frequency of the incident electro-magnetic wave

$$N_{crit} = \frac{\epsilon_0 m_e}{e^2}\omega^2 \tag{2.17}$$

For a laser in the near infrared ($\omega \simeq 3 \times 10^{14}$ Hz), the electron density may, thus, reach up to 10^{20} cm^{-3}.
The temporal behaviour of the free electron density $N(t)$ is described by

$$\frac{\partial N}{\partial t} = [\beta - \gamma N(t)]N(t) - \delta N(t) \tag{2.18}$$

with the rate parameters β for *avalanche ionization*, γ for *inelastic collision* and δ for *electron diffusion*. A square root dependence of the threshold power density on pulse duration was observed in several studies when using picosecond or nanosecond laser pulses [Koe92]. Numerical calculations and measurements from [Nie95][Lös95] show a dependence of the threshold power density on pulse duration

$$E_{th} \sim \tau^x \tag{2.19}$$

with

$x < 0.1$	for	τ <100fs
$x = 0.4...0.6$	for	4 ps< τ <8 μs
$x > 0.8$	for	τ >300 μs

2.3.1 Photodisruption

New investigations have shown that, at higher pulse energies - and thus higher plasma energies-, shock waves and other mechanical side effects such as *cavitation*, and *jet formation* become more significant and might even determine the global effect upon the tissue [Ste89][Nie95][Juh94]. Due to the fact that tissue is split by mechanical forces, this interaction mechanism is called photodisruption and is distinguished from plasma-mediated ablation.
The plasma volume determines the fraction of incident energy to be converted to shock waves or cavitations. If the plasma volume is large - like in plasmas induced by picosecond or femtosecond pulses - more energy is required for ionizing and vaporization of matter.

Hence, this amount of energy can no longer contribute towards the generation of potential shock waves or cavitations. Once the plasma has formed, it absorbs and scatters further incident light thereby "shielding" underlying structures (plasma shielding).

2.3.1.1 Shock wave generation

Due to high kinetic energy, the plasma electrons are not confined to the focal volume of the laser beam, but rather diffuse into the surrounding medium. When the inert ions follow with a certain time delay, mass is moved which is the basic origin of shock wave generation. This shock wave soon separates from the boundary of the plasma. It initially moves at hypersonic speed and eventually slows down to the speed of sound. The initial pressure at the boundary of the laser plasma thereby reaches several kbar. It was observed by Vogel et al. [Vog94] that the shorter the pulse, the smaller the width of shock waves and thus, the size of cavitation bubbles. This is extremely important for applications of plasma-mediated laser tissue ablation where a smooth surface is essential for the treatment to be sucessful, e.g. LASIK (laser in situ keratomileusis) [Hei00].

2.3.1.2 Cavitation

Cavitation is an effect that occurs when focusing the laser beam not on the surface of a tissue, but into it. The focal volume is vaporized by means of high plasma temperatures. Therefore, cavitation bubbles consist mainly of water vapour and carbon oxides. Within less than a millisecond, the bubble implodes again as a result of the outer static pressure, compressing the content again and leading to a rebound of the bubble. A second transient is emitted and the whole sequence may repeat a few times until all of the energy is dissipated and all gases are absorbed by surrounding tissue [Lau72]. As cavitation bubbles may be up to a few millimetres in diameter, macroscopic photodisruptive effects inside originate primarily from the combined action of cavitation and jet formation.

2.3.1.3 Jet formation

When cavitation bubbles expand in the vicinity of a solid boundary, a high-speed liquid jet directed towards the wall is produced. If the bubble is in direct contact with the solid boundary during its collapses, the jet can cause a high-impact pressure against the wall. Thus, bubbles attached to solids have the largest damage potential. When the bubble collapse due to external pressure, the surrounding fluid is accelerated towards the centre of the bubble. The damaging effect is enhanced if gas bubbles remaining from an earlier pulse are hit by acoustic transients generated by subsequent pulses. Therefore, ultrashort pulse lasers which generate smaller cavitation bubbles can be operated at higher repetition rates compared to Q-switched laser systems.

These four effects - plasma formation, shock wave generation, cavitation and jet formation - all take place on a different timescale. This is schematically illustrated in fig. 2.6. Plasma formation begins during the laser pulse and lasts for a few nanoseconds. This

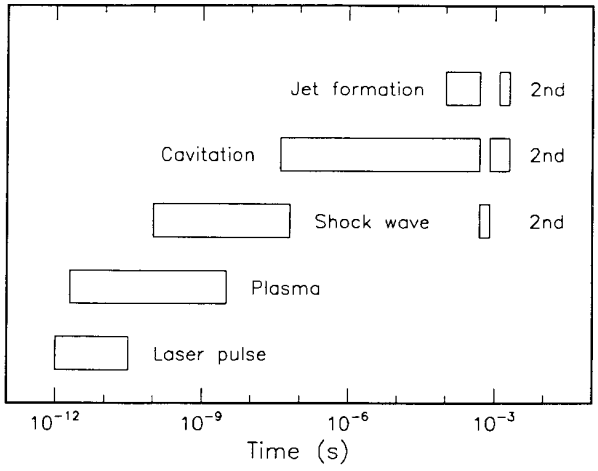

Fig. 2.6: Approximate time scale for all processes contributing to photodisruption. Assumed is a 30 ps laser pulse. The first and second occurrence of shock wave, cavitation and jet formation are indicated. [Nie96]

is the time needed by the free electrons to diffuse into the surrounding medium. Shock wave generation is associated with the expansion of the plasma and, thus, already starts during plasma formation. However, the shock wave then propagates into adjacent tissue and leaves the focal volume. Approximately 30-50 ns later, it has slowed down to an ordinary acoustic wave. Cavitation, finally, is a macroscopic effect starting roughly 50-150 ns after the laser pulse. The time delay is caused by the material during the process of vaporization. Usually, the cavitation bubble performs several oscillations of expansion and collapses within a period of a few hundred milliseconds. Since the pressure inside the bubble increases during collapse, each rebound of the cavitation bubble is accompanied by another shock wave.

Chapter 3

Interventional magnetic resonance imaging (IMRI)

Today, magnetic resonance imaging (MRI) is one of the most important tools in clinical diagnostics. It allows non-invasive investigation of anatomical structures with a very high spatial resolution and excellent soft tissue contrast. Images of any orientation within the whole body can be acquired. New fast imaging techniques and the improvement of contrast medium have given way to a vast range of new MRI applications such as MR angiography [Boc00], investigation of brain function and perfusion, MR urography [Sch93] as well as MR pulmonary imaging [Bac96].
During the last few years the use of new compact superconducting coils and the progress in high frequency technology have allowed clinical operations under online MRI control, on either open MRI scanners with two magnets facing each other aligned in a c-shaped set-up or so-called "doughnut" systems where the scanner consists of a pair of separate coils similar to a *Helmholtz*-coils set-up. Both systems allow the physician to access to most parts of the body.
The main advantage compared with conventional techniques using x-ray or ultrasound is the absence of ionizing radiation and the excellent image resolution. Nevertheless, IMRI is still rather costly compared with other operation techniques due to the fact that all surgical instruments must be non-ferromagnetic.
In this chapter the fundamentals of magnetic resonance imaging and its application for fast, i.e. online temperature monitoring are described. Detailed quantum-mechanical and technical descriptions can be found in [Abr61], [Kre88], [Sli89], [Lis90], [Rei90] and [Mor95]. Details of MR thermometry are described in [Haa86], [Haa90], [Ste95] and [Boh99].

3.1 Fundamentals of nuclear magnetic resonance (NMR)

In medical applications of NMR, the focus is put on protons, mostly from free water molecules, which make up over 55% of the volume of the human body. Liquid water

molecules are characterized by their stochastic rotational and translational movements. The coupling of nuclear spins is relatively weak compared to the coupling to external fields. Thus, in a first approximation, the proton can be considered as a separatet system coupled to an external heat bath. Atomic nuclei with an odd number of nucleons possess an angular momentum $\hbar\vec{I}$, the nuclear spin. It is linked to the magnetic dipole momentum $\vec{\mu}$ according to

$$\vec{\mu} = \gamma\hbar\vec{I} \tag{3.1}$$

were γ is the gyromagnetic ratio (for the proton $\gamma/2\pi = 42.577$ MHz/T).

The hamiltonian for a particle in a magnetic field $\vec{B}_z$ parallel to the z-axis is given by

$$\langle H\rangle = -\vec{\mu}\vec{B}_z = -\gamma\hbar B_z I_z. \tag{3.2}$$

Due to the high number of particles ($6.7\cdot\ 10^{19}/\mathrm{mm}^3$), their behaviour can be described using *Boltzmann*-statistics

$$N_{m-1}/N_m = exp\{-\gamma\hbar B_z/k_B T\} \tag{3.3}$$

with k_B being the *Boltzmann-constant* ($k_B = 1.38 \cdot 10^{-23} J/K$). The system energy for spins parallel to the static field B_z is somewhat smaller than those for the spins anti-parallel to B_z, leading to a surplus of protons ($\approx 1 \cdot 10^{-3}$) that contribute to the NMR signal. This number seems very small, but due to the vast number of water molecules ($3.3{\cdot}10^{19}/\mathrm{mm}^3$), the signal is detectable. However, tissue with a low water content like cortical bone is nearly "non-visible" to MRI (see section 4.3).
At room temperature, the *Zeemann energy* $E_m = -\gamma \cdot \hbar \cdot B_z$ is much smaller than the thermal energy $k_B T$, thus eq. 3.3 can be written as linear equation. According to equation 3.1 this results in a macroscopic magnetic dipole momentum (equilibrium magnetization)

$$M_0 = \frac{N\gamma^2\hbar^2 B_z}{4k}\frac{1}{T} \tag{3.4}$$

with N = number of spins. This corresponds to *Curie's law*, with the magnetization being proportional to $1/T$.
During the NMR experiment, an additional alternating magnetic field $\vec{B}_1(t)$, perpendicular to $\vec{B}_z$, is applied. This results in an angular momentum $\vec{m} \times \vec{B}$ to the probe, with $\vec{B} = \vec{B}_z + \vec{B}_1(t)$. According to the conservation law of angular momentum, this leads to a temporal change in angular momentum $d\vec{M}(t)/dt = \vec{\omega} \times \vec{M}(t) = \gamma\vec{M}(t) \times \vec{B}(t)$ leading to the fundamental relation

$$\omega_L = \gamma B_z \tag{3.5}$$

where ω_L is called the *Lamor frequency*. Thus, in the case of a resonant irradiation of the circular polarized $\vec{B}_1(t)$ over a time t_{RF}, the magnetization is flipped by an angle

$$\alpha = \gamma B_1(t) t_{RF} \quad (0^\circ < \alpha \leq 180^\circ) \tag{3.6}$$

following a precession with ω_L around the static field B_z (similar to precessing children top in the earth's gravitational field).

3.1.1 Relaxation processes

After the RF pulse, the magnetization relaxes due to the interactions of the spins with the static field until the magnetic momentum is parallel to B_z (see fig.3.1). This relaxation is called *spin-lattice relaxation*. Due to the interaction of the spins, the magnetization perpendicular to B_z also shows a relaxation called the *spin-spin relaxation*.

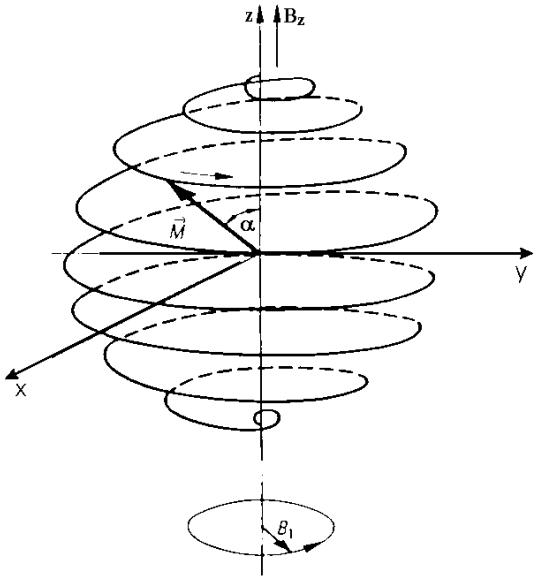

Fig. 3.1: Movement of nuclear magnetic momentum $\vec{M}$ in the static magnetic field $\vec{B}_z$ and the circular polarized RF field $\vec{B}_1(t)$. [Mor95]

According to Bloch [Blo46], these two processes can be written as

$$\frac{dM_z}{dt} = \gamma(\vec{M} \times \vec{B})_z + \frac{(M_0 - M_z)}{T_1} \tag{3.7}$$

$$\frac{dM_{x,y}}{dt} = \gamma(\vec{M} \times \vec{B})_{x,y} - \frac{M_{x,y}}{T_2} \tag{3.8}$$

leading to

$$M_z = M_0(1 - exp\{-t/T_1\}) M_\perp = M_0(1 - exp\{-i\omega_L t - t/T_2\}) \tag{3.9}$$

with $M_\perp = M_x + iM_y$ and the tissue-dependent time constants T_1 and T_2 respectively[1]. In biological tissue, however, protons are not only bound to water molecules, but also to proteins and other macromolecules, resulting in a shorter relaxation time T_1 (see section 4.1). Relaxation times vary strongly between different sorts of tissues leading to an excellent tissue contrast in MR images.

3.2 Magnetic resonance imaging (MRI)

During MRI, the patient or tissue sample is placed in the centre of the static field coil. In order to be able to assign the MR signal to a selected volume element (voxel), three gradient fields $\vec{B_x}, \vec{B_y}$ and $\vec{B_z}$ are superimposed on the static field.

3.2.1 Spatial coding

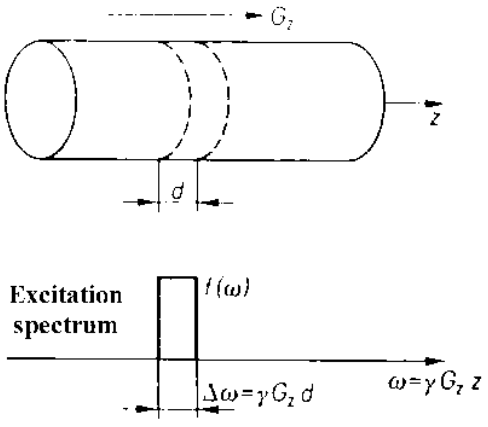

Fig. 3.2: Selective excitation of a small layer within a cylindrical object. The spectrum of the RF pulse determines the location and thickness of the layer. [Mor95]

With a field gradient in z-direction $\Delta B_z = G_z \cdot \Delta z$, the Lamor frequency becomes z dependent (see fig.3.2). Thus, with $\omega(z) = \gamma(B_z + G_z \cdot z)$, an RF pulse (sinc-pulse) with a bandwidth $\Delta\omega$ excites spins only in a layer

$$\Delta z = \frac{\Delta\omega}{\gamma G_z} \tag{3.10}$$

To compensate the phase shift from the different ω_L along G_z, a refocusing gradient is applied.

3.2.2 Phase and frequency coding

To assign the signal from the spins in x direction, a field gradient G_x is switched for a short time t_p. During this time, the spins precess with different frequencies depending on their x-position $\Phi(x, t_p) = \gamma \cdot G_x \cdot x \cdot t_p$. After the gradient field has been switched off, all

[1]Due to inhomogeneities ΔB_z of the static field, the actual relaxation time T_2 has to be replaced by $T_2^* = T_2/(1 + T_2\gamma\Delta B_z)$

spins have the same frequency, but different phases $ph_p = exp\{i \cdot \gamma \cdot G_x \cdot x \cdot t_p\}$ (see fig. 3.3).

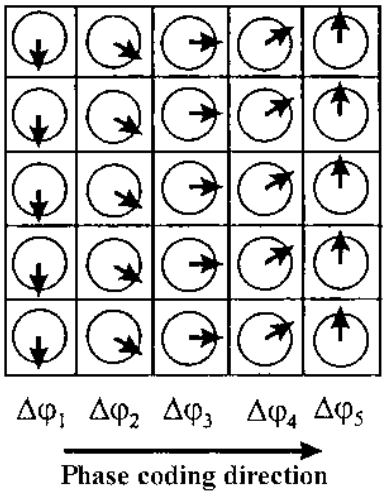

Fig. 3.3: Model of spin orientation after phase coding. [Boh99]

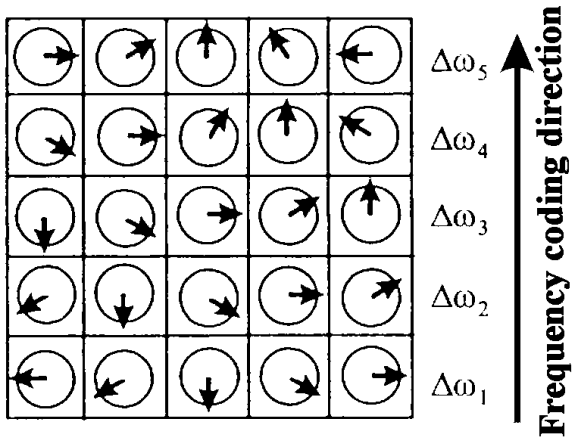

Fig. 3.4: Model of spin orientation after frequency coding. [Boh99]

After phase coding, the data acquisition of the induction signal is started. During data acquisition, a gradient G_y is switched in y-direction. Thus, the spins precess with different Lamor frequencies, depending on their y-position. Data acquisition is carried out with a rate of $1/\Delta t$ leading to a phase difference after a time $m\Delta t$: $ph_f = exp\{i\gamma[G_y y m\Delta t]\}$ (see fig. 3.4).

3.2.3 Image reconstruction

A local coil is used for the acquisition of the MR signal placed close to the structures under investigation (e.g. head coil, spine coil). After data acquisition, image reconstruction is performed using a two-dimensional *fast Fourier transform* (FFT). Thus, data from the frequency domain is transformed into grey-scale images. Two pulse sequences are used for clinical MRI. For T_2-weighted images, a *spin-echo sequence* is used. It consists of a 90° pulse followed by a time TE/2 during which the transversal magnetization decreases due to spin-spin interaction (see section 3.1.1). Then a 180° pulse is applied along the x-direction resulting in a reflection of the magnetization related to the x-z-plane (rotating system). The spins are inverted thereby, but their sense of rotation is conserved in such a way that they are all in phase again after another TE/2, leading to the so called *"spin-echo"* (see fig.3.5). The total acquisition time is given by $t_{acq} = TR \cdot N_{ph} \cdot N_{acq}$, where TR is the time between two acquisitions, N_{ph} is the number of phase coding steps, i.e. the image resolution, and N_{acq} is the number of acquisitions. This leads to acquisition times of several minutes for a diagnostic MR image.

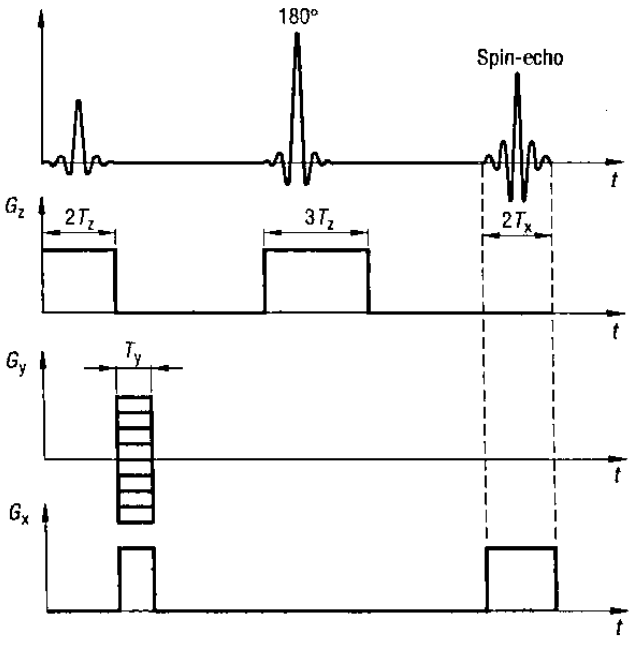

Fig. 3.5: Typical spin-echo sequence (see text for details).

3.3 Real-time MRI temperature control

Spin-echo sequences are unsuitable for fast temperature control with update rates of one or two seconds due to their long acquisition time. Therefore another, faster pulse sequence has to be used, the *gradient-echo sequence*. During data acquisition, the signal drops rapidly, hence, before data acquisition is started (after the initial 90° RF pulse, and phase and frequency coding), an inverse frequency coding gradient is switched over half the acquisition time and then, with reverse polarity, switched again, in such a way that the signal reaches its maximum in the middle of the acquisition (*gradient-echo*). In addition, with short initial RF pulses, i.e. small flip angles, *fast low angle shot* (FLASH) sequences can be performed. The pulse sequence for a FLASH image is shown in figure 3.6. With short repetition times, TR (TurboFLASH) and the latest ultrafast gradient systems, data acquisition and, thus, update times can be reduced to a few milliseconds.

3.3.1 T_1-method

After saturation with a 90° pulse, the T_1 time recovers during a variable time period T_{rec} followed by a FLASH sequence with small flip angles (10-15°) and is, therefore, called saturation-recovery TurboFLASH (SRTF) [Haa90]. At an initial temperature T_0, the magnetization is then given by [Boh99]

$$S(T_0) = S_\infty(T_0)[1 - exp\{-T_{rec}/T_1(T_0)\}] \tag{3.11}$$

$S_\infty(T_0)$[2] contains the steady-state magnetization, which is, according to *Curie's law* (eq.

[2]The index ∞ expresses that, after a sufficiently long period of time, the longitudinal magnetization has reached its initial value → steady-state magnetization.

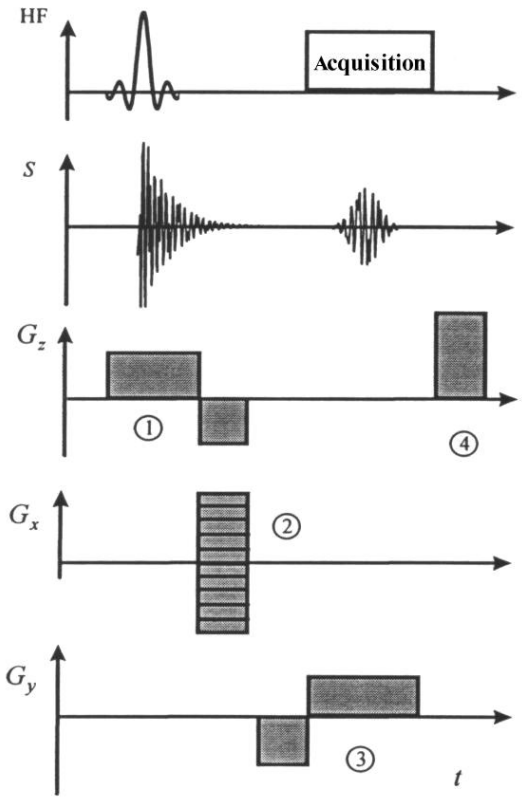

Fig. 3.6: FLASH sequence. (1) is the spatial selection gradient, (2) represents the phase coding gradient, (3) shows the gradient for frequency coding and echo generation (see text). (4) is a spoiler gradient to destroy transversal magnetization. This sequence is repeated N_{ph} times with different phase coding gradients. [Boh99]

3.4) proportional to 1/T, leading to

$$S_\infty(T_0 + \Delta T) = \frac{S_\infty(T_0)}{1 + (\Delta T/T_0)} \tag{3.12}$$

Assuming a linear dependence of T_1 with temperature $T_1(T_0 + \Delta T) = T_1(T_0) + m\Delta T$, the signal intensity is then given by

$$S(T_0 + \Delta T) = S_\infty(T_0) \cdot \underbrace{\frac{1}{1 + \Delta T/T_0}}_{I} \cdot \underbrace{\frac{1 - exp\{-T_{rec}/(T_1(T_0) + m\Delta T)\}}{1 - exp\{-T_{rec}/T_1(T_0)\}}}_{II} \tag{3.13}$$

Expression I shows the temperature dependence of the equilibrium magnetization. Temperature dependence of the relaxation time is given by expression II. A recovery time T_{rec} is chosen, thereby, leading to a maximum temperature sensitivity. The tissue-dependent parameters from equation $T_1(T_0)$ and $m = dT_1/dT_0$ have to be calculated from calibration measurements. Several SRTF sequences with different T_{rec} have to be acquired for every type of tissue . Fitting T_{rec} against the signal amplitude according to eq. 3.11 using a least-square algorithm [Mar63] leads to a mean value of T_1. Repeated at different temperatures, one gets the parameters $T_1(T_0)$ and $m = dT_1/dT_0$ and, thus, a value for $T_1(T)$. Fast data acquisition is essential for online temperature monitoring. Before the measurement is started, a temperature table is calculated from a reference image using equation

3.13. The actual temperature map is then calculated online with update times of 2-3 seconds. A quasi real-time temperature monitoring can be achieved thereby.

3.3.2 Proton resonance frequency (PRF) or chemical shift

The term *chemical shift* is used to describe the influence of the molecular environment on local magnetic field B_{loc} at the location of the nucleus. The local field B_{loc} can be described as

$$B_{loc}(T) = (1 - \sigma(T))B_z \tag{3.14}$$

where $\sigma(T)$ is the screening constant of the molecule [Ber98]. The proton resonance frequency is linearly dependent on temperature with a sensitivity of approximately 0.01 ppm/°C [Jak97][Mul97][Mac96]. The PRF changes can be determined by a phase image of a spoiled gradient-echo sequence. For the calculation of local temperature changes ΔT(r), this approach determines the local phase difference $\Delta\phi$(r) between a reference scan and the actual scan. The thermally-induced phase difference is proportional to the temperature difference, the magnetic field strength B_z and the echo time TE. The temperature-related dependence of the phase difference $\Delta\phi$(r) is then given by

$$\Delta\phi(\mathbf{r}) = \gamma \cdot TE \cdot \alpha \cdot \Delta T(\mathbf{r}) \cdot B_z \tag{3.15}$$

where γ is the gyromagnetic ratio of the proton and α the proportionality constant of the linear temperature dependence of the screening constant σ [Poo95]. Thus, at 1.5 T, an echo time of 20 ms results in a phase change of $\approx$ 4.6 ppm/°C. However, these changes are relatively small and the method puts high demands on the temporal stability of the external magnetic field.

3.3.3 Diffusion method

A third method to determine thermal changes during MRI is the temperature dependence of molecular diffusion due to *Brownian motion*. Diffusion induces an amplitude attenuation of the MR signal caused by a loss of phase coherence among precessing spins that move randomly along the direction of the gradient. This amplitude attenuation A depends only on the diffusion coefficient D and the gradient, so that $A = exp\{-b \cdot D\}$, where b is a factor that can be calculated from gradient characteristics (strength and duration)[Bih89]. Molecule diffusion mapping is based on two MR images differently sensitized to diffusion by the presence of specially designed gradient pulses. Under these conditions, the diffusion image $D_{x,y}$ is derived from the relation

$$D_{x,y} = \frac{log(A_{1x,y}/A_{0x,y})}{b_0 - b_1} \tag{3.16}$$

where b_0 and b_1 are the calculated gradient factors of both images and A_1/A_0 is the amplitude attenuation ratio in each pixel. A map of temperature changes $(T-T_0)_{x,y}$ can, thus, be obtained from two diffusion images $D_{x,y}$ and $D_{0x,y}$, one acquired at the reference temperature $T_0(D_{0x,y})$ and one obtained at a different temperature $T(D_{x,y})$ such that

$$(T - T_0)_{x,y} = (kT_0^2/E_a) \cdot [(D - D_0)/D_0]_{x,y} \tag{3.17}$$

assuming small temperature variations ($T - T_0 \ll T_0$) and that E_a (activation energy for translational molecular diffusion) is approximately constant.

Chapter 4

Bone tissue

Throughout this work laser-tissue interaction is concentrated on bone tissue. This chapter gives an overview of the anatomical and physiological structure of bone and its physical properties. Detailed information about the development and growth of bone tissue is given in [Ker98] [Sch99] [Ben93].
Further information about optical and thermal properties can be found in [Duc90] [Lun72] [Mil52].

4.1 Fundamentals of bone structure

Bone is superbly engineered to provide great strength yet minimal weight, protection, locomotion (with muscles) and it acts as a repository for hemopoietic[1] tissues and as storage facility for calcium and phosphorus. Bone is a dynamic, living tissue that is constantly turning over - i.e. older bone is resorbed but is continuously replaced by deposition of new bone [Ker98].
As an organ, bone consists of bone tissue (mineralized connective tissue), cartilage, bone marrow and fat. Macroscopically, two types of bone can be distinguished. Cortical bone (also known as compact or dense bone) is hard and represents about 80% of skeletal weight. The inner cancellous bone (also known as spongy or trabecular bone) forms a honeycomb-type network enclosing cavities filled with bone marrow. It resembles a scaffold with a large surface area, the orientation of trabeculae relating to mechanical loads placed upon the bone (see fig. 4.1).
Bone is about **90% extracellular matrix** and **10% water** by weight. The matrix is **60-70% inorganic mineral**[2]. The organic component of the matrix is of type I collagen.

[1] blood forming

[2] predominantly microcrystalline calcium phosphate, which is similar to hydroxyapatite ($Ca[Ca_3(PO_4)_2]_3OH_2$), with traces of sodium, magnesium, fluoride and other ions

4.2 Development and growth of bone

Bone can normally be formed only by deposition on a suitable, pre-existing, naturally occuring matrix (e.g. bone matrix or calcified cartilage) or solid surface (e.g. prothesis) that is in close proximity to a blood supply.

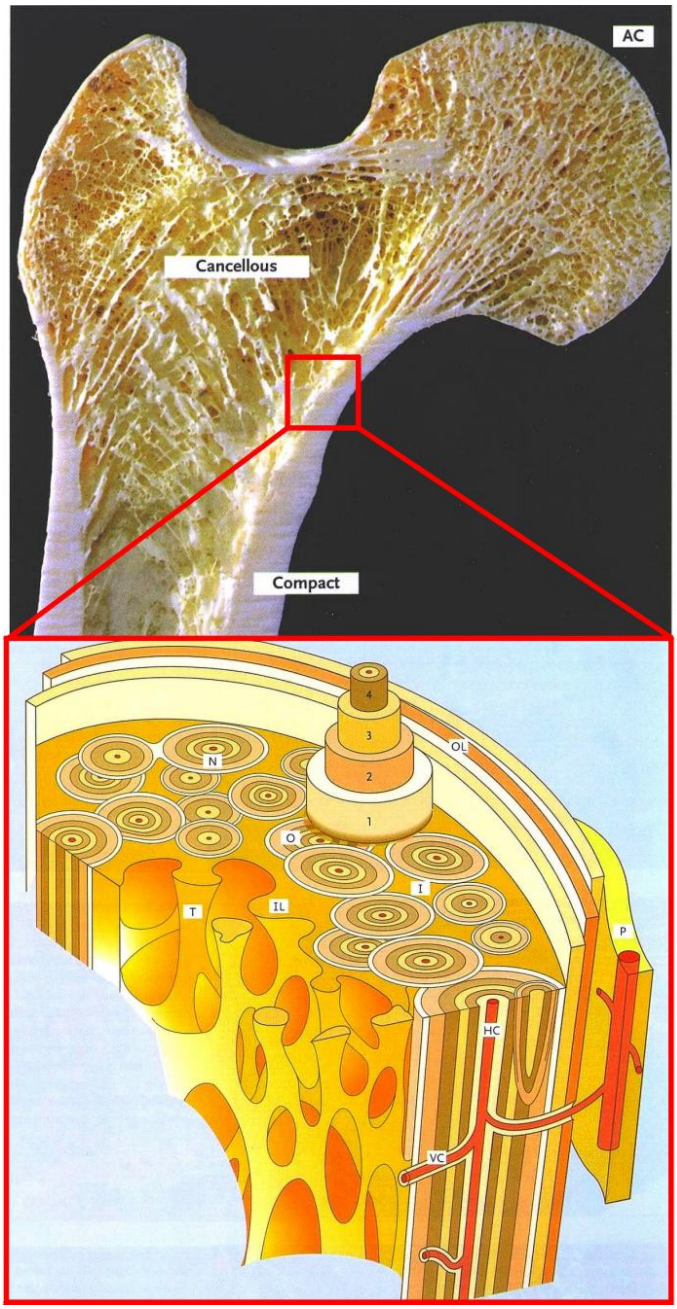

Fig. 4.1: Section through a dried thigh bone (femur) showing its internal macroscopic architecture. Two types of bone are noted: compact (cortical) and cancellous (spongeous or trabecular) bone. The enlarged region shows the typical structure of the cortical bone with osteons (O), overlapped by more recently formed, i.e. newer osteons (N). Interstitial lamellae (I) lie between the osteons. The external surface, covered by periosteum (P), transmits blood vessels to the Harvesian canals (HC), which connect with adjacent osteons via the Volkmann's canals (VC). The endosteal surfaces (towards bone marrow) face the trabeculae (T) of cancellous bone. Concentric lamellae in each osteon (1,2,3,4,) contain collagen fibres oriented perpendicular to each other. [Ker98]

These two criteria place limitations on the shape and size of developing bone, i.e. newly formed bone is deposited in layers with a variety of shapes (flat, curved, undulating) and mineralization sites must be within 200 μm of a capillary to receive nutrients via diffusion. Skull, facial and clavicular bones form by intramembranous ossification in areas of mesenchyme. The axial and appendicular skeleton, especially the long bones, forms by enchondral ossification in areas of cartilage.

4.2.1 Enchondral ossification

Bones of the fetal skeleton and developing limbs require growth in length and diameter and, in order to achieve this, cartilage is formed as an intermediary tissue between the initial appearance of mesenchyme[3] and the formation of bone.
Growth of the ribs, long bones and vertebrae is achieved by forming a miniature but enlarging cartilage model, which is gradually replaced by bone normally in a precise manner. In the centre the oldest cells hypertrophy and degenerate and their surrounding cartilage matrix becomes calcified by formation of mineral deposits. This represents the future site where bone deposition takes place.

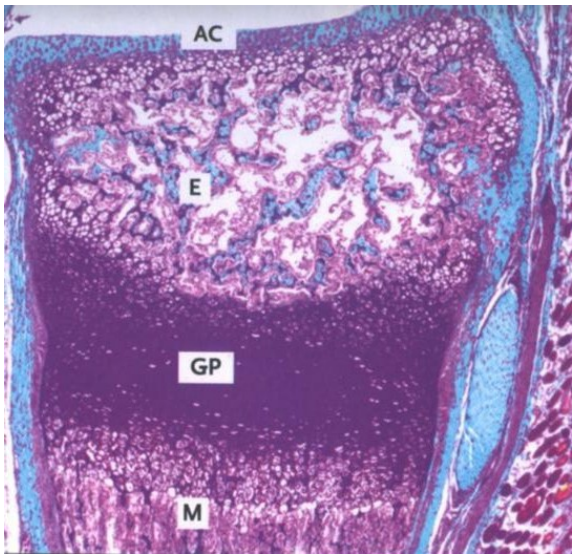

Fig. 4.2: Enchondral development, showing how the epiphysis (E) constains cancellous bone with branching trabeculae containing darkly staining cores of calcified cartilage. Below the growth plate (GP), spicules of darkly stained calcified cartilage are covered by newly deposited woven bone, the latter laid down by osteoblasts derived from blood vessels coursing through the metaphysis (M). [Ker98]

Newly formed central cancellous woven bone is partly resorbed, leaving a medullary cavity for hemopoietic tissue. The shaft of diaphysis of the model is gradually replaced by bone and marrow, but the two ends, still made entirely of cartilage, become the epiphysis. Where the bone of the shaft meets a region of epiphyseal cartilage, a special zone of hyaline cartilage is formed. This is recognized as the epiphyseal growth plate.

4.2.2 Epiphyseal growth plate

In the growth plate, chondrocytes align into columns and represent the functional units of longitudinal bone growth. The extensions of calcified cartilage provide a suitable surface for bone to be deposited on [Pas96].

Epiphyseal growth plates allow the epiphysis to be pushed apart without being replaced by new bone. The continuous production of cartilage tissue (at the epiphyseal side) and its elimination (at the metaphyseal side) maintains the depth of the growth plate and causes a shift of the epiphysis away from the bone centre, the diaphysis being fixed. The only tissue surviving from the migrating growth plate is the mineralized

[3]Mesenchymal cells are stem cells (pluripotent cells) which are capable of division and development into more specialized cells.

calcified matrix, which forms longitudinal septa upon which osteoid is deposited by osteoblasts. When chondrocytes stop dividing, the growth plate is converted into bone and in adult bones it may be visible on radiographs as an indistinct line in the region of the previous growth plate.

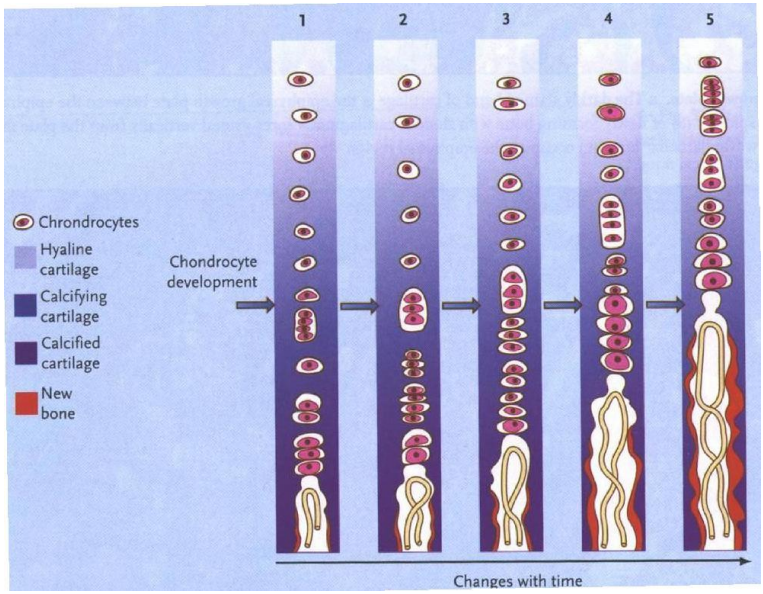

Fig. 4.3: Zones of epiphyseal growth plate. Sequences of events with time (1-5) representing the migration of the columns of chondrocytes away from the metaphysis and central region of a long bone. [Ker98]

As condrocytes hypertrophy, the interterritorial matrix begins to calcify, becoming mineralized toward the ossification zone. The invading metaphyseal capillaries are associated with pluripotent perivascular mesenchymal cells, which differentiate into osteolasts. These cells lay down new bone (osteoid) on the calcified cartillage via apatite crystals within special vesicles, although direct focal calcification of the collagen component of the matrix is also a possible contributor. Only about one-third of calcified septa serve as platforms for bone deposition, the rest are resorbed by chondrocytes associated with the capillaries [Hor93].

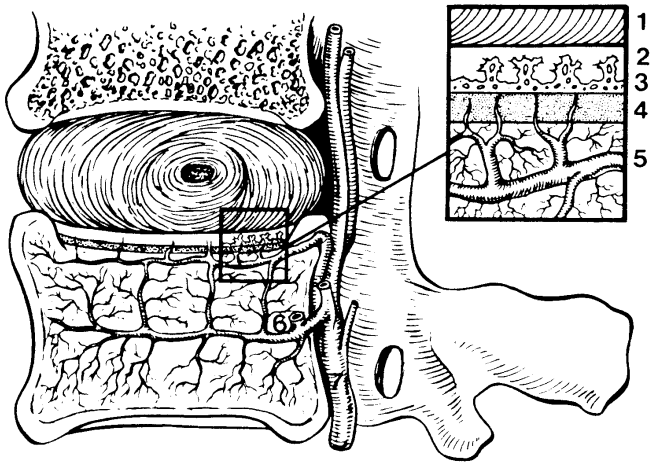

Fig. 4.4: Illustration of intravertebral venous system. (1) discus intervertebralis, (2) capillary bed in articular cartilage, (3) subchondral, postcapillary net, (4) vertebral epiphysis with vertical vein, (5) horizontal subarticulary collecting vein, (6) basivertebral vein, (7) anterior part of vertebral vein plexus. [Cro73]

Fig. 4.4 shows the collecting veins in the region of the epiphyseal plate and the centre of the vertebral bodies which run horizontally from the anterior side to the dorsal vertebral

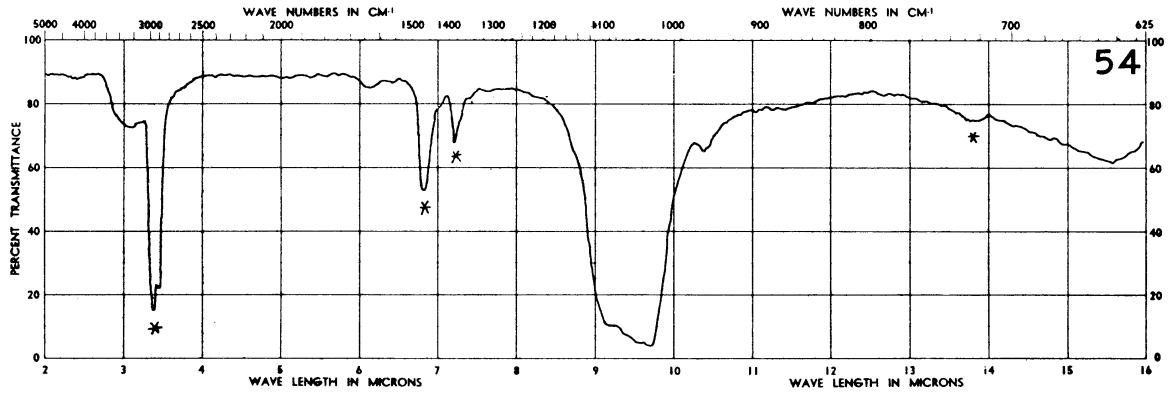

Fig. 4.5: Absorption spectrum of tribasic Calcium phosphate ($Ca_3(PO_4)_2$) which represents 80% of bone mineral.[Mil52]

veins.

4.3 Physical properties of bone tissue

Knowledge of physical properties of bone tissue such as thermal conductivity, heat capacity, density and absorption coefficient is essential for the calculation of laser-tissue interaction (see section 2.2). For online MRI temperature monitoring T_1 and T_2 relaxation times are important. Although bone tissue does not have a homogeneous structure (see section 4.1), physical properties can be determined as a mean value for macroscopically distinguishable components of compact (cortical) bone and spongeous (trabecular) bone. There are, however, some differences between in vitro and in vivo experiments.
The water content of the tissue is the most important parameter for thermal laser-tissue interaction especially in the infrared spectrum. The higher the water content the stronger the energy absorption, as can be seen from experiments with the Ho:YAG laser ($\lambda = 2.12$ μm (see fig. 2.2)). Cartilage tissue has a high water content of approximately **55-85%** and therefore strongly absorbs Ho:YAG laser light. This allows for an effective ablation of cartilage tissue as described in chapter 5.

In contrast, cortical bone contains only 10-15% of water. Thus, fast and efficient laser ablation of bone tissue can only be achieved with lasers operating at wavelengths which correspond to the absorption peaks of bone tissue. The absorption coefficient μ_α of pure hydroxyapatite at wavelengths of the CO_2 laser ($\lambda = 9.6$ μm and 10.6 μm) ranges from 3500 to 5500 cm^{-1} [Nyq71]. Since the organic matrix of hydroxyapatite consists mainly of tribasic Calcium Phosphate ($Ca_3(PO_4)_2$)[New77] the absorption coefficient for the Ho:YAG laser ($\lambda = 2.12$ μm) can be determined to be $\mu_\alpha \approx 500$ cm^{-1}, corresponding to the absorption spectrum shown in fig. 4.5. The absorption coefficient is about 7 times higher than that for H_2O. Thus, bone matrix absorbs most of the laser energy and may become very hot ($T_{melt} = 1280$ °C). Using known thermal and optical constants [Duc90], thermal relaxation time τ of cortical bone for a wavelength of 2.12 μm can be estimated

	cortical bone	trabecular bone	cartilage	water
μ_a [cm^{-1}]	≈ 500 ($\lambda = 2.120\ \mu m$) see fig. 4.5		1200 ($\lambda = 1.06 \mu m$)	see fig. 2.2
λ [$Wm^{-1}K^{-1}$]	0.2 - 0.3	0.3 - 0.4	0.6	0.7
c [$Jg^{-1}K^{-1}$]	1.2 - 1.3	1.2 - 2.4	3.5 - 3.8	4.18
ρ [gcm^{-3}]	2	1.1	1.1	1
χ [m^2s^{-1}]	0.8×10^{-7}	1.2×10^{-7}	1.5×10^{-7}	1.7×10^{-7}
τ [μs]	$\approx$ 400 - 800 μs ($\lambda = 2.12\ \mu m$)			see fig. 2.3

Table 4.1: Comparison of optical and thermal parameters for cortical and trabecular bone, cartilage and water.

to be $\approx$ 1.2 ms.
Table 4.1 gives an overview of the optical and thermal parameters of cortical and trabecular bone, cartilage and water.

Chapter 5

Minimally-invasive laser treatment of spinal deformities

The main emphasis of this work was put on the development of a completely new laser-induced operation technique for the minimally-invasive treatment of spinal deformities in young patients (*idiopathic scoliosis*[1]). This study was carried out in cooperation between the University of Heidelberg's Kirchhoff-Institute of Physics and it's orthopaedic clinic. The method is based on minimally-invasive endoscopic laser treatment under an anterior (thoracoscopic) surgical approach.
This chapter describes the complete development from a preliminary evaluation of different laser systems (see section 5.3) to a first application on animals (foxhounds). The aim of the initial evaluation was to find a suitable laser meeting all of the requirements for effective clinical treatment with maximum safety for the patient.
In contrast to the conservative surgical scoliosis treatment used at present [Har62], [Alv77], [Lon95], [Zie76], the new operation technique can be performed using modern minimally-invasive endoscopic surgery in combination with laser light and is thought to benefit both the surgeon as it is a straightforward operation technique and the patient as at causes **less pain** and produces **excellent cosmetic results**, thus leading to **faster mobilization** and briefer hospitalization.

5.1 Idiopathic scoliosis

In contrast to the normal physiological curvature of the spine, scoliosis represents the severe lateral curvature that is often accompanied by a rotational component.

Most people have small deviations of the spine that are without any consequences for their health or well-being. The severe deformities of scoliotic spines, however, do not only affect the patients' appearance, but also have a major impact on their life expectancy.

[1]The term "scoliosis" was first used by Galen (AD 131-201) in "De moto maerculorum", although spinal deformity had been described previously by Hippocrates 470 BC

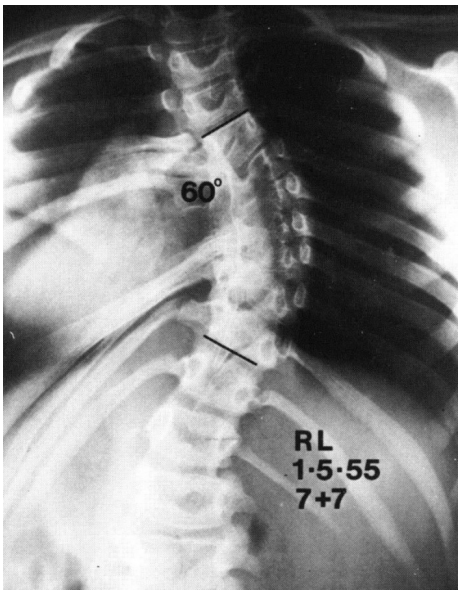

Fig. 5.1: X-ray image of a 7-year-old patient with juvenile idiopathic scoliosis [Lon95].

Most scoliosis are left-sided in the region of the thoracic spine and, thus, the vital functions of the heart and the lung are heavily affected. Since the thorax is reduced in volume on the concave side of the curvature, the heart may be compressed and the lung has no sufficient space to fully inflate (see fig.5.1).
Idiopathic scoliosis is the most common of all forms of lateral deviation of the spine which occurs during the growing years [Lon95]. These deformities are thought to result mainly from malfunctions in vertebral growth (see section 4.2.1), since curves progress rapidly during the adolescent growth spurt, which occurs at age 12 years in girls and a year or two later in boys.

5.1.1 Vertebral and spinal growth

Spinal growth does not proceed in a uniform linear pattern. There are two periods of rapid growth : the first is from birth to age 3 and the second takes place at the adolescent growth spurt. The point of maximum growth velocity occurs at a mean age of 14 years. The main growth thereby comes from the cartilage of the epiphyseal plates of each vertebra (see fig. 4.2.2).

5.1.2 Evolution of scoliosis treatment

Hippocrates (460 BC) was the first to write extensively on spinal deformity and described different forms and types. He noted that the severity of the deformity was related to the age at which it appeared. He also invented the first treatment by applying a mechanical tension alongside the body axis as shown in fig. 5.3

Today, most surgical treatment of spinal deformities centres on invasive mechanical

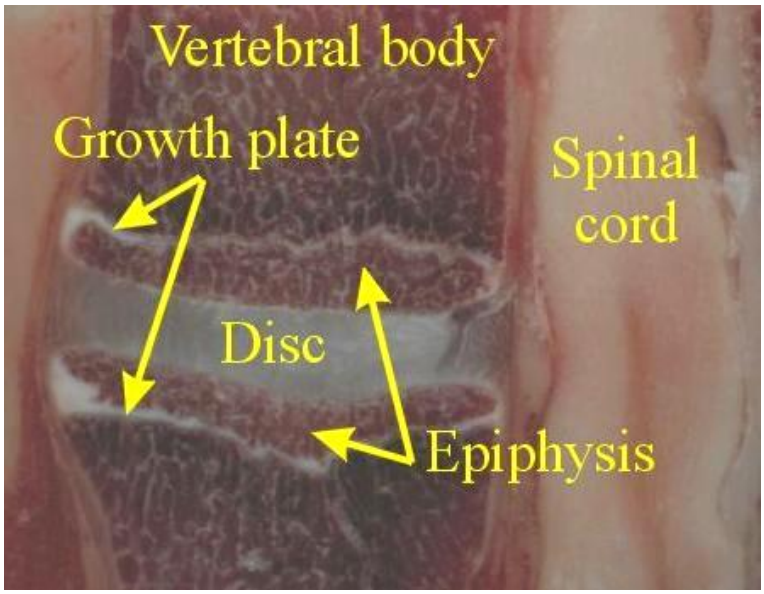

Fig. 5.2: Coronal cut with cryomicrotome showing the vertebral body, the intervertebral disc, the epiphysis and the spinal cord. The growth results mainly from the thin cartilage of the epiphyseal growth plate.

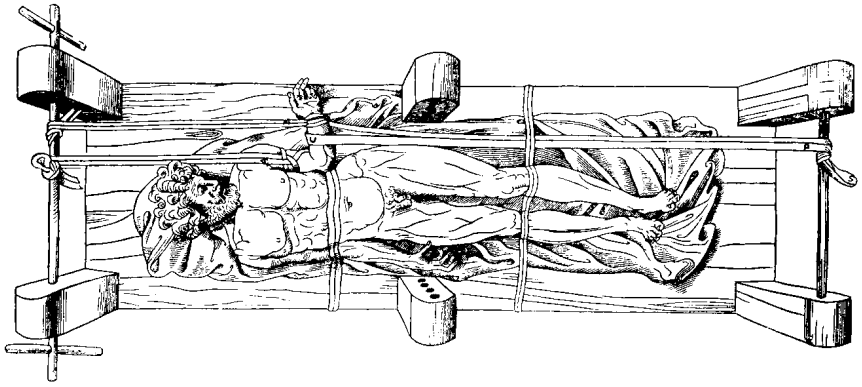

Fig. 5.3: The machine invented by Hippocrates. It was used in a like manner for torso distraction.[Lon95]

techniques with long operation times and major effects on the patient's mobility. In most cases, a posterior (dorsal) approach is chosen to achieve a solid arthrodesis by the insertion of rods in the vertebral bodies. These rods are then fixed with bolts along the spine in order to apply a mechanical force to the vertebral bodies and, thus, to straighten the spine (see fig. 5.4).

5.2 Laser hemiepiphysiodesis on the spine

It is known that an early partial ablation of the epiphyseal growth plate (*hemiepiphysiodesis*) over several vertebrae can cause scoliotic growth [Bis40],[Can79],[Haa39],[Pac39],[Roa60]. Furthermore, in 1924 Wittek first showed on young scoliotic patients with sufficient growth potential that a hemiepiphysiodesis on the **convex** side of the curvature over several vertebrae resulted in a straightening of the

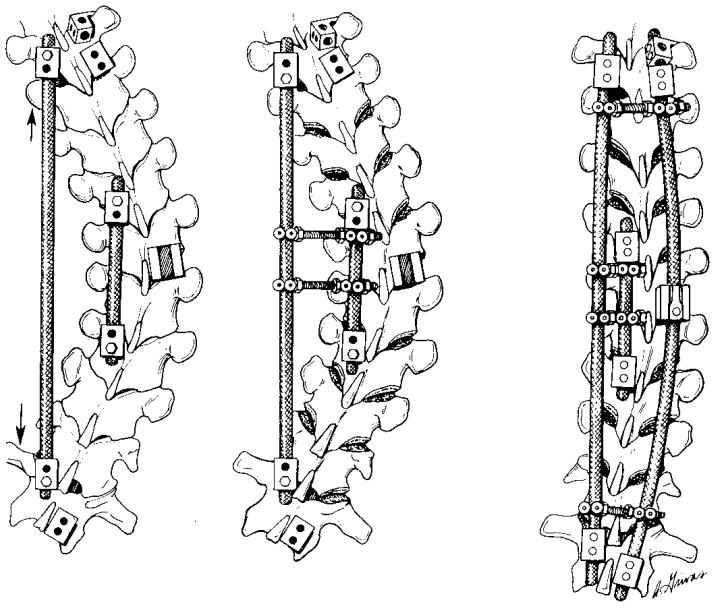

Fig. 5.4: Posterior treatment of spinal deformities using rods and bolts that are fixed in the vertebral bodies to apply a mechanical force to the spine.[Lon95]

spine [Wit24].
In contrast to Wittek, who used mechanical instruments (chisel) to remove the epiphyseal growth plate in open surgery, our new method is based on minimally-invasive, precise laser ablation. Therefore, the aim of this work is to show that our treatment model is capable of inducing a change in spinal growth, i.e. of producing a scoliosis. Hence, if laser hemiepiphysiodesis on the spine is capable of inducing such a scoliotic growth, the opposite, i.e. **laser ablation** on the **convex side** over several vertebrae in young patients with **sufficient growth potential**, should result in a straightening of the spine. It is assumed that only the complete destruction of the growth plate is sufficient to affect spinal growth. Therefore, a simple coagulation (see section 2.2.3) of the tissue, as done during laser-induced interstitial thermotherapy (LITT), is considered to be insufficient. In addition, laser ablation has to be precise due to the fact that the epiphyseal growth plate is very small (see fig. 5.2), and thermal damage to adjacent structures has to be minimized since the intervertebral disc is separated from the growth plate only by a small layer of cortical bone (epiphysis). In particular, the heat exposure to the spinal cord must not exceed 42°C.

5.3 Evaluation of four different laser systems

In order to evaluate which laser best meets these requirements, i.e. precise, efficient, fast and safe removal of the epiphyseal growth plate, a first study involved a comparison of four different laser systems including an argon ion, two Nd:YAG (Q-switched and cw) and a Ho:YAG laser with respect to **thermal damage** to adjacent structures, especially the nerve roots, the vessels, the disc and the spinal canal, **ablation rates**, **efficiency** and **laser handling**.
This evaluation is part of my diploma thesis and is described in detail in [Rum98]. Only

those results that are relevant to the in vivo measurements will be mentioned in this section. Table 5.1 gives an overview of the laser parameters.

5.3.1 Materials and methods

The first laser system examined was an argon-ion laser (Innova 300, Coherent, USA) driven in the cw-mode (λ =514 nm) at an average power between 1 and 2 W. A BK7 lens (f=125 mm) was used to focus the laser beam down to a spot diameter of 30 μm, which allowed for easy adjustment and, thus, a precise tissue ablation. The average power density reached 3×10^5W/cm^2.

Laser system	Wavelength	Power density	Energy	Pulse duration
Nd:YAG	1064 nm		4 mJ, 1 kHz	12-14 ns
Nd:YAG (2)	532 nm		2 mJ, 1 kHz	12-14 ns
Nd:YAG (3)	355 nm		1 mJ, 1 kHz	12-14 ns
Ar^+	514 nm	1.5 W		cw
Nd:YAG	1064 nm	20 W		cw
Ho:YAG	2120 nm		800 mJ	250 μs

Table 5.1: Overview of the parameters of the four lasers evaluated.

The second laser was a compact diode-pumped Nd:YAG laser system at 1064 nm (*Starline*, Lambda Physik, Germany). It was driven in the Q-switch mode with repetition rates up to 1 kHz and pulse durations of 10 ns. Through this non-linear lithium borate (LBO) crystals, the system could also generate the second harmonic at 532 nm and the third harmonic at 355 nm. As with the argon-ion laser set-up, the beam was first widened and then focused onto the tissue surface. The beam waist in the focal plane was measured to be 100 μm at 1064 nm with a pulse energy of 4 mJ leading to a power density of up to 5.1×10^9 W/cm^2. At 532 nm, the focal beam width reached 180 μm with a mean pulse energy of 2 mJ and, at 355 nm the spot size decreased to 70 μm with pulse energies of 1 mJ leading to power densities of 7.8×10^8 W/cm^2 and 2.5×10^9 W/cm^2 respectively.
The power density of 2.5×10^9 W/cm^2 in combination with laser light in the UV range led to photoablation [Nie96] [Bou86] in which molecular bindings are broken by single photons (see fig. 5.6).

The other two laser systems in the study were a cw Nd:YAG laser at 1064 nm (*Medilas 4060N*, Dornier, Germany) and a pulsed Ho:YAG laser at 2120 nm (*Medilas H*, Dornier, Germany). In contrast to the set-up described above, the laser light was transferred through a plastic-clad silica optical fibre with a core diameter of 800 μm for the Nd:YAG laser and 600 μm for the Ho:YAG laser. The Nd:YAG laser had a maximum power of

20 W and, therefore, reached a power density of 4×10^4 W/cm^2, whilst the Ho:YAG laser was run in the pulse mode with a pulse duration of 250 μs and a pulse energy of 800 mJ at 8 Hz leading to a power density of 1.1×10^6 W/cm^2.

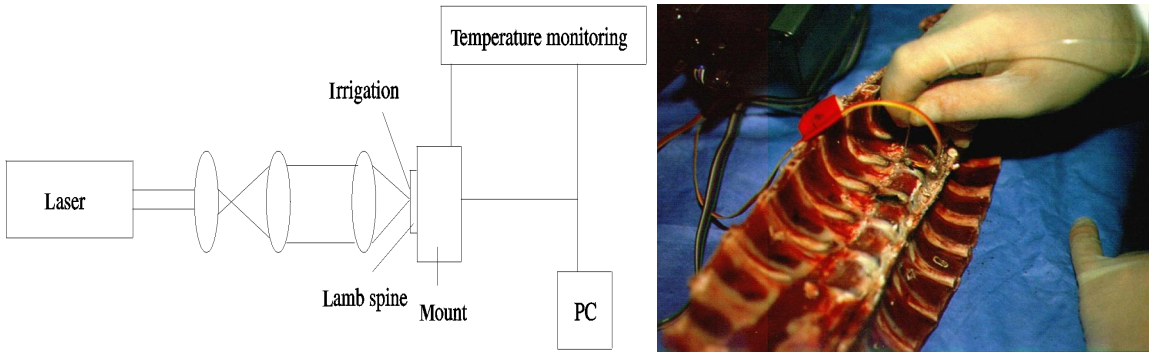

Fig. 5.5: Set-up of experiments with the Q-switched Nd:YAG and argon-ion laser (left) and the cw Nd:YAG and Ho:YAG laser (right).

5.3.2 In vitro investigations

The spines of three- to four-month-old lambs were used for in vitro investigation. Lambs' spines were chosen because their anatomical structures are similar to those of the target group of young patients. Preparation was done by cutting off the spinal muscles, the aorta and fat tissue in order to expose the vertebrae, the disc and the epiphyseal growth plate. Before laser treatment was performed, the size of each vertebra was determined using MRI (1 Tesla Gyroscan, Philips, The Netherlands). The turbo spin-echo sequence (see section 3.2.3) turned out to be the most suitable for this purpose using the following parameters: TR=3000 ms, TE=130 ms, TH=3 mm and FOV=210 mm.

The set-up for the experiments with the argon-ion and the Q-switched Nd:YAG lasers is shown in the diagram side in fig. 5.5. The laser beam was first widened and then focused onto the tissue surface in order to get a small focal spot. The spine was fixed in a special mount that could be moved in the x-y plane by means of computer-controlled stepping motors. During laser action, the sample was moved in a rectangular pattern and the desired area was ablated in multiple sections. After each layer, the whole mount was moved in the z-direction and the pattern was repeated until the calculated depth had been reached.
In order to remove the debris and cool the tissue, additional irrigation with isotonic saline solution was applied using a 5 ml injection every 30 seconds or more often if intense carbonization occurred.
Small semiconductor probes were inserted into the disc, the vertebral body and the spinal canal for temperature monitoring and to determine the thermal damage which the laser might cause in the corresponding area. The data were digitally read by computer

via an ADC.

The set-up for measurements using the Nd:YAG and Ho:YAG laser is shown in the photograph in fig. 5.5. Here, the spine was placed on a germ-free table and the laser was applied by moving the fibre tip over the tissue. It was established that the most effective way of applying the energy was to insert the tip steadily into the tissue until the desired depth was reached and then repeat the procedure along the growth plate until all cartilage tissue has been removed. Again, the temperature probes were fixed in the vertebrae, the disc and the spinal canal.

After laser treatment, the spine was examined using MR and x-ray imaging to see whether the ablation had been complete and the important parts of the growth plate had been removed.

A further, very useful means of examination was the cryomicrotome[2]. For preparation, the spine had to be dissected into three pieces so that coronal, sagittal, and transversal cuts could be made. The specimens were embedded in a special mount filled with gel. After 2 days in the freezer, the mount was fixed in the microtome and cut with a slice thickness of 50 μm.
Small pieces were also prepared from each spine for additional histological and scanning electron microscope (SEM) examination.

5.3.3 Results and discussion

No carbonization could be observed at an energy level of 2.5×10^9 W/cm^2 using the third harmonic of the Q-switched Nd:YAG laser, i.e. with its high photon energy at 355 nm, the laser exceeded the threshold of photoablation, which allows for very precise tissue removal without heating up adjacent structures. However, the ablation rate was only 2-3 mm^3/min corresponding to a low efficiency of 0.04 mm^3/J.
Q-switched that time.
With the second harmonic at 532 nm, massive heating was observed leading to vaporization and carbonization. Once the tissue was carbonized, heat absorption was much stronger resulting in even greater carbonization. Although irrigation could reduce the rise in temperature, the tissue was buckled at the edge of the ablation zone. The ablation rate was about 6 mm^3/min with an efficiency of 0.06 mm^3/J.

At the fundamental wavelength of 1064 nm, similar results concerning heat production and carbonization could be observed. The ablation rate of 9.3 mm^3/min was somewhat higher, leading to the same efficiency of 0.06 mm^3/J, taking the increase in pulse energy into account. Fig. 5.6 shows the difference between thermal ablation on the left with massive carbonization and photoablation on the right without any sign of carbonization.

[2]In contrast to conventional microtome cuts, the tissue has to be frozen in a special liquid. The cryomicrotome makes it easy to cut especially large samples of hard tissue, e.g. cortical bone.

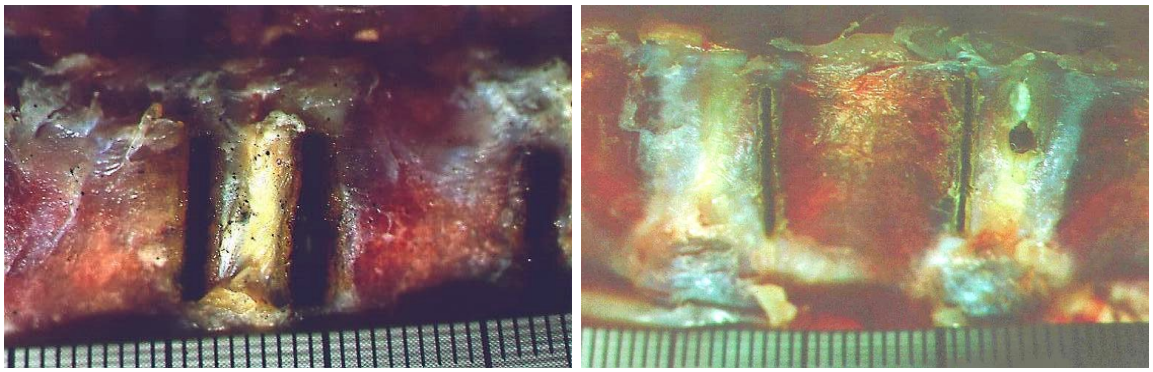

Fig. 5.6: Comparison of tissue ablation with the Q-switched Nd:YAG laser after thermal ablation (left) and photoablation (right).

The argon-ion laser was able to ablate very precisely due to the small beam waist of 30 μm. However, heating was very strong in the disc, which meant that the pulse energy had to be reduced. Under intense irrigation, the temperature could be decreased by 10°C. At an average power of 1.2 W, a compromise between thermal damage and ablation was found. This power level led to an ablation rate of 8.3 mm^3/min. The good beam quality of the argon laser made it the most efficient (0.11 mm^3/J) of the four laser systems.
The cw Nd:YAG laser used with the bare fibre, showed good results in ablation speed and handling. The fibre could be moved easily to the appropriate region. However, tissue removal could be achieved only with a relatively high laser power of about 16 to 20 W. This again led to major carbonization and thermal damage to the adjacent tissue. The ablation rate of 12.5 mm^3/min is high enough for operational use, but heat and carbonization may cause damage to the nerve roots. Since the bare fibre allows only beam diameters of more than 700 μm, the efficiency was very low with only 0.01 mm^3/J. In addition, the uneven fibre tip led to diffraction and reflection, which heated up the fibre tip to such an extent that the plastic coating caught fire. This could be avoided only by intermediate laser action and intense irrigation. This still caused a high rise in temperature in the adjacent tissue of more than 35°C.

The high pulse energy of the Ho:YAG laser led to high ablation rates of 15 mm^3/min with an efficiency of 0.06 mm^3/J. In addition, the heat transfer to adjacent tissue was much less than that of the cw-mode lasers due to the pulse duration of 250 μs, which is much shorter than the average thermal relaxation time of cartilage tissue (τ = 0.12 s). With intermediate laser application and irrigation, the heating of adjacent tissue could be retained at a non-critical level (see fig. 5.7) of less than 45°C. Fig. 5.8 provides a comparison of the parameters of each laser system.

Considering the ablation rate, handling and thermal damage to collateral tissue, the Ho:YAG laser turned out to be the most suitable laser system of the four lasers tested and was, therefore, chosen for ongoing in vivo investigations on young foxhounds.

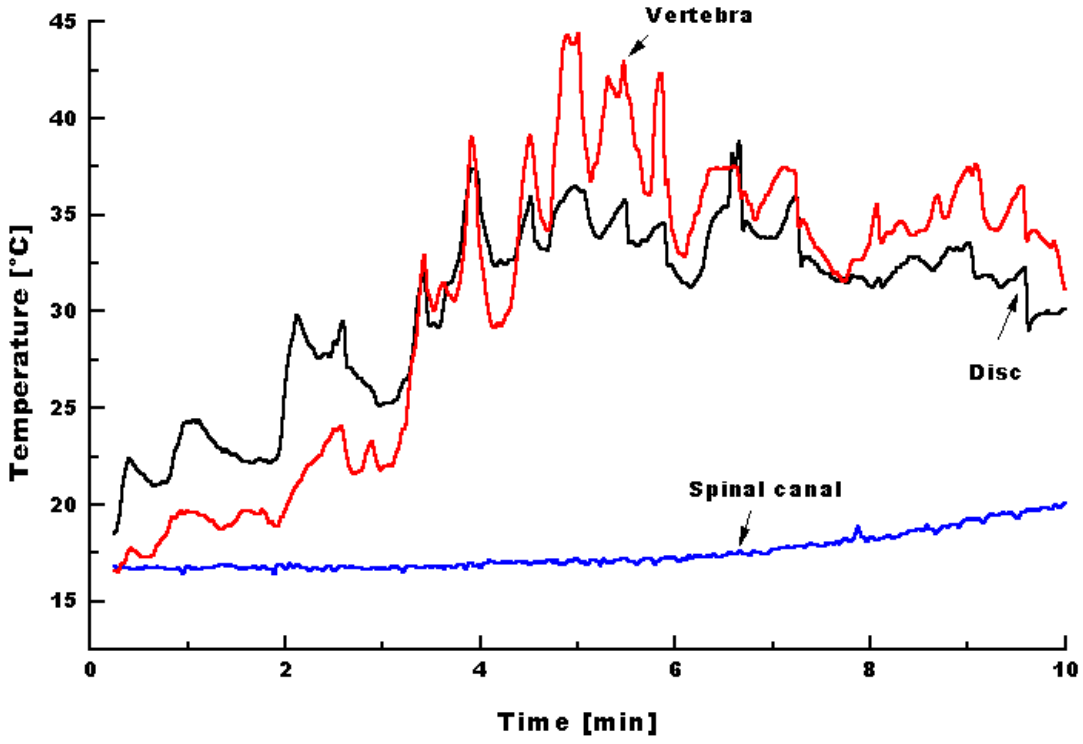

Fig. 5.7: Comparison of the rise in temperature during laser ablation with the Ho:YAG laser using a pulse energy of 800 mJ and a repetition rate of 8 Hz (see text for details).

5.4 MRI temperature control

Although temperature measurements with small probes are sufficiently accurate and give precise information about the rise in temperature, it would be more convenient to have a non-invasive method of temperature monitoring, especially during in vivo experiments. Inserting a probe into the disc or spinal canal during in vitro experiments is reasonable, but it is impossible during in vivo measurements. To overcome this problem non-invasive MRI experiments were carried out at the German Cancer Research Centre (DKFZ) in Heidelberg using a TOM SP 4000 scanner (1.5 T, Siemens, Germany). For this investigation, a part of the spine was mounted in a water tank, the temperature of which could be adjusted and controlled externally.
Data acquisition was carried out using a specially developed saturation recovery turboFLASH (SRTF) sequence [Ste95] with recovery times between 60 and 4000 ms and centric phase encoding. This leads to a magnetization dependence on T_{rec}, according to

$$M(T_{rec}) = M_0 sin(\alpha)(1 - e^{-\frac{T_{rec}}{T_1}})e^{-\frac{TE}{T_2^*}} \tag{5.1}$$

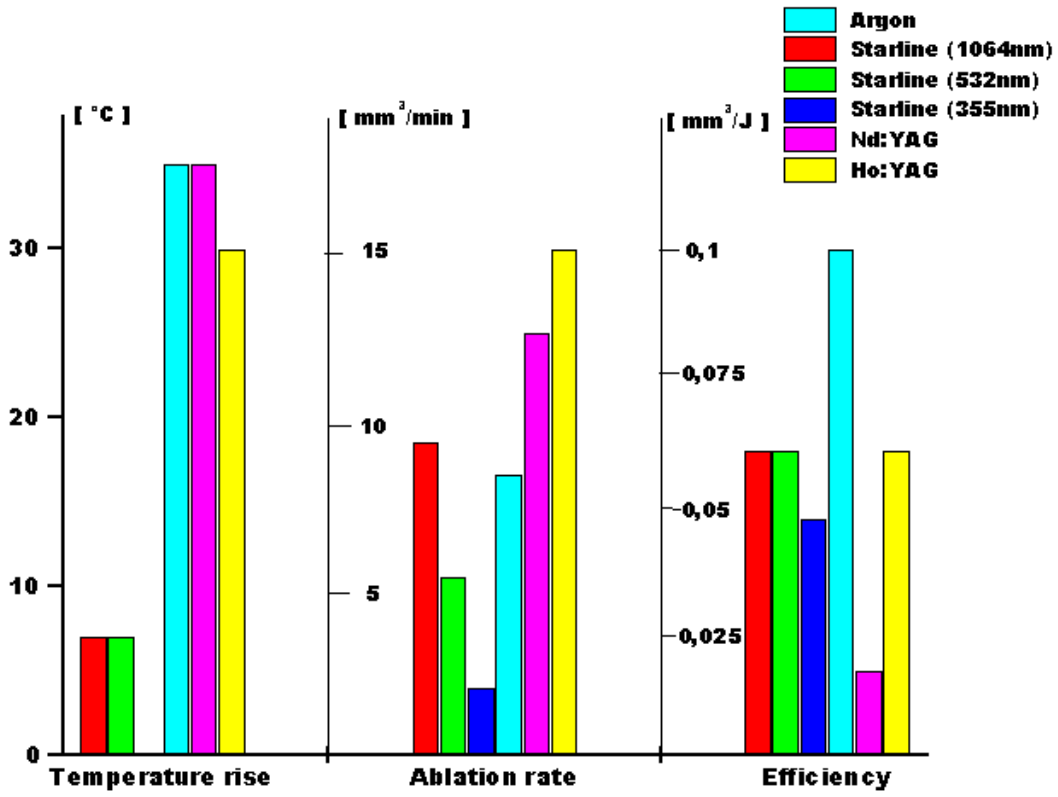

Fig. 5.8: Comparison of the rise in temperature (with irrigation), the ablation rate and the efficiency of the four laser systems evaluated. The cw-lasers (argon-ion and Nd:YAG) show a high rise in temperature of more than 35°C. The argon-ion laser reached was the most efficient due to its small spot size.

where $\sin(\alpha)$ corresponds to the small angle stimulation (see section 3.3). The term $\exp(-\frac{TE}{T_2^*})$ describes the free induction decay (FID) with the effective transversal relaxation time T_2^*. The T_1 relaxation time was derived starting at a temperature of 20°C. After each measurement, the water temperature was increased by 5°C using the following parameter for data acquisition: TE = 4 ms, $\alpha = 12°$, TH = 7 mm, FOV = 128 mm. The data acquired were plotted using Marquardt-Levenborg leastsquare algorithms. The results are shown in fig. 5.9.

5.5 Minimally-invasive scoliosis treatment with a Ho:YAG laser

The second step was to perform the proposed minimally-invasive operation technique during **in vivo** experiments on young foxhounds using the *Medilas H* Ho:YAG laser with

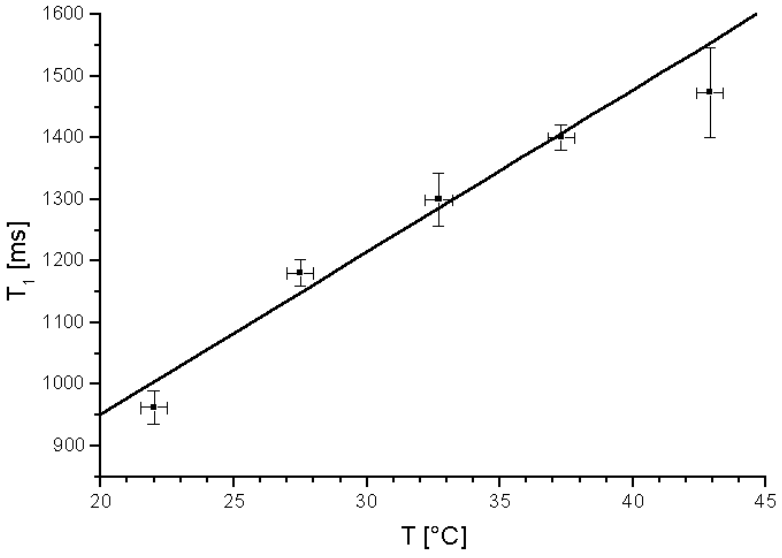

Fig. 5.9: Temperature dependence of T_1 time in the disc. The slope of the linear regression fit is 24 ± 3 ms/°C.

a 3-D thoracoscopic approach. During these operations, temperature monitoring was carried out using fibre-optic fluorescent probes.

5.5.1 The Ho:YAG laser

The *Medilas H* laser system is designed for clinical use with a compact mobile housing and closed cooling system making it an autonomous turn-key system. For safety reasons, the system can only be operated if the pilot laser (Helium-Neon laser, $\lambda = 633$ nm) is switched on.

The laser medium consists of a Holmium doped Ytterbium Aluminium Garnet ($Yb_3Al_5O_{12}$) crystal with doping rates of approximately $10^{19} - 10^{22}$ cm^{-3}. Population inversion is reached from the absorption of Cr^{3+} to a metastable level of $^3F_4$ and the upper $^3H_4$-level of the Tm^{3+} ion is populated from a non-radiative decay. Laser emission takes place as a decay from the $^5I_7$ -level to the $^5I_8$ -level ($\lambda = 2120$ nm).

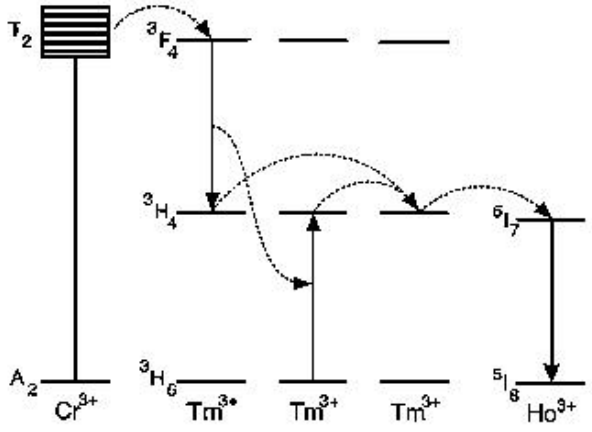

Fig. 5.10: Energy level chart of a Ho:YAG laser. The upper $^3H_4$-level of the Tm^{3+} ion is populated from a non-radiative decay. Laser emission takes place as a decay from the $^5I_7$ -level to the $^5I_8$ -level ($\lambda = 2120$ nm).

The zone of thermal damage due to carbonization from the Ho:YAG laser varies between the different sorts of tissues according to their water content. For cartilage tissue with a water content of $\approx 70\%$, ablation is dominated by laser absorption of the water molecules ($\alpha_{H_2O} \approx 50$ cm^{-1} at 2120 nm). Thus, due to the high pulse energies of up to 1800 mJ, the first pulses already lead to a strong deposition of energy within a small tissue volume (thermal penetration depth $\approx 250\ \mu m$), which is converted into heat through vibrational and rotational energy states of the water molecules (refer to section 2.2). This leads to a sudden vaporization of water inside the tissue resulting in micro explosions that also eject tissue fragments with high kinetic energy, carrying away a vast amount of the pulse energy. After all of the water within the focal volume has evaporated, subsequent pulses lead to a rapid heating of the tissue. The same occurs in tissue with a low water content, such as cortical bone. These high temperatures lead to a charring of the tissue surface within a zone of $\approx 50\ \mu m$ [Sch92] which results in even stronger light absorption and thus speed up the heating of the tissue. The temperature within the thermal volume may rise up to several thousand °C within a few microseconds, thereby igniting a thermal plasma [Hel92], [Kuh98]. This is accompanied by a typical noise and intense fluorescent light. In keeping the tissue surface covered with a thin water layer, e.g. by irrigation, the total lateral thermal damage can be reduced to 100 - 200 μm.

5.5.2 Video-assisted thoracoscopic spinal surgery (VATS)

With the advent of video technology, thoracoscopy offers a minimally-invasive operative approach for accomplishing thoracic surgical procedures previously performed through open techniques [Kee93].
A 3-D thoracoscopic system was used for minimally-invasive operations (Richard Wolf, Germany). The distal end of the thoracoscopic system is rigid with an outer diameter of 10 mm. The video signal from the CCD camera of the endoscope with two objective lenses at the distal end (see right-hand photograph in fig. 5.12) is connected via a video signal processor to a monitor with a refresh rate of 100 Hz. This processor sends alternating images from the left and the right channel. Through wearing special shutter glasses (see fig. 5.15) synchronized with the monitor frequency, the surgeon gets a three-dimensional image of the operation field. Fig. 5.11 shows the assembly of the endoscope.

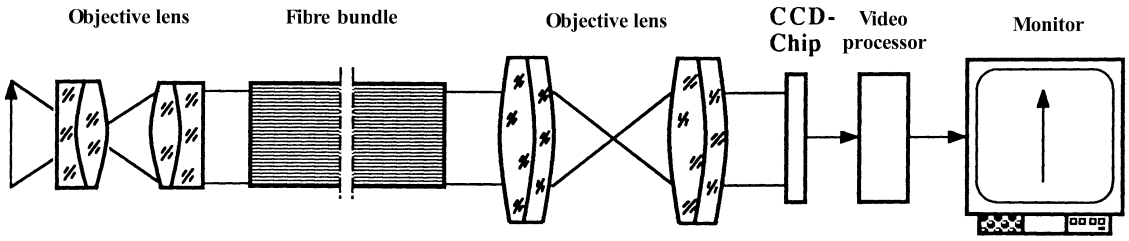

Fig. 5.11: Components of a typical endoscopic system [Bit92].

During long operations, a useful alternative is a so called “head-mounted display”

(HMD). The left image in fig. 5.12 shows an HMD with displays mounted on a helmet-like system. The video signal is sent to an LCD in front of each eye. This is very convenient for the surgeon as he can rest his head in a relaxed position throughout long endoscopic sessions, instead of having to concentrate permanently on a monitor. In addition, any sort of image, such as x-rays, and CT or MRI images can be shown on the LCD using the microphone attached to the HMD.

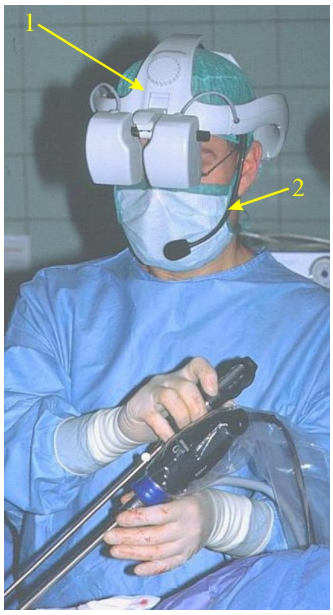

Fig. 5.12: Top: Distal end of 3D thoracoscope with two objective lenses and irrigation canal. Left: Head mounted liquid cristal display (LCD) for endoscopic operations (1). The microphone (2) can be used to load any type of image, i.e. x-rays, and CT or MRI images.

Careful evaluation of the pre-operative MRI scan is important for planning trocar placement and reducing the time required to localize the area of spinal pathology.
Another new piece of technology is the interventional video tomography (IVT) in which computer-generated structures are fused with the endoscopic video images in real time allowing 3-D reconstruction from any kind of medical planar imaging data, such as ultrasound, CT or MRI [Tru95].

5.5.3 In vivo investigations

It is known that lambs do not have a thoracic septum which is necessary to make sure that, during the operation, only one half of the lung collapses. Having consulted a veterinarian, we therefore decided to use foxhound puppies for in vivo investigation. Foxhounds were considered appropriate because they easily tolerate anaesthesia during long operation times and their thorax is of a size comparable to that of young patients. All experiments were carried out at a specially-equipped animal operation section of the orthopaedic clinic of Heidelberg.
Before each operation, the foxhounds were examined using MRI scans (1 T Gyroscan, Philips, The Netherlands) to provide sufficient information about their anatomical structures and the size of their thorax (see left-hand photograph in fig. 5.13). For data acquisition, the foxhound was placed in its left side on a receiver coil for spinal investigation (synergy spine coil) (see right-hand photograph in fig. 5.13). The width and the

length of the trachea was measured for later intubation . The images were also a means of orientation for the surgeon during the operation.

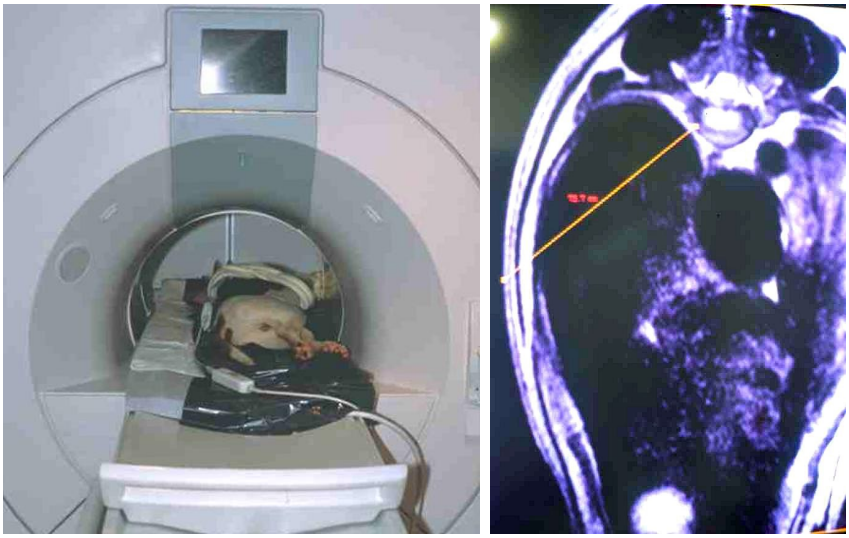

Fig. 5.13: On the left: MRI investigation of a 3-month-old foxhound lying on its left side using a synergy spine coil for local signal acquisition. On the right: transversal MRI (TSE) of 3-month-old foxhound. The image was used to determine the length of the trachea and to measure the size of the thorax. The marked line represents a length of 19.7 cm and roughly shows the direction of the surgical approach.

5.5.4 Experimental surgical set-up

Catheters were inserted into the jugularis externa vein, the metatarsalis dorsalis artery and the ureter to control blood and urine circulation under anaesthesia . To gain additional information about the intra-operative stress, the following parameters were monitored continuously:

- ECG, heart frequency
- arterial blood pressure
- central venous pressure
- capnography (endexpiratory CO_2-level)
- pulseoxymetry (%-oxygen saturation of peripheral haemoglobin)
- vital capacity
- respiration frequency

Discontinuous monitoring included body temperature (rectal) and blood gas analysis. An additional 2-D bronchoscopic system was used for intubation. The set-up for the thoracoscopic laser hemiephysiodesis in the operation room is shown in fig. 5.14.

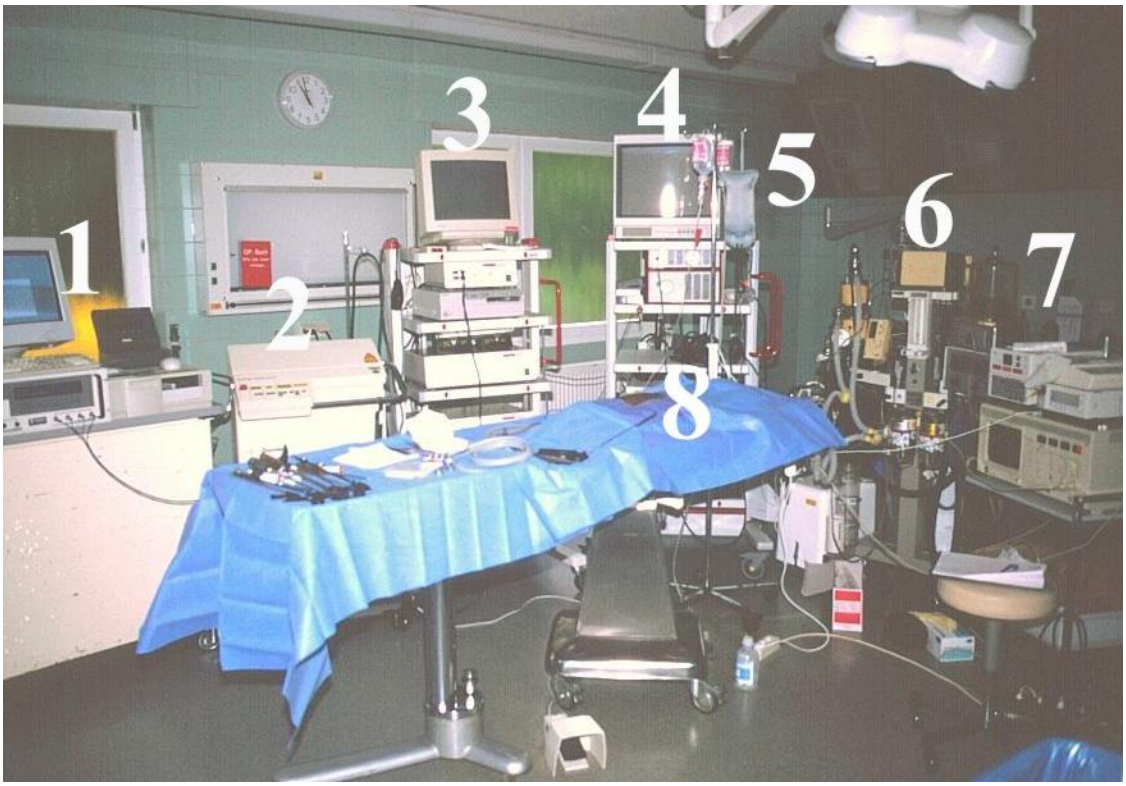

Fig. 5.14: Experimental set-up during an in vivo operation. From left to right: fluoroptic temperature control (1), Ho:YAG laser (2), 3-D endoscopic system (3), 2-D endoscopic system (4), suction/irrigation unit (5), anaesthesia system (6), ECG monitor (7) and operating table in the centre with foxhound (8).

Throughout the entire operation, the video signal for the 3-D thoracoscopic system was recorded on tape (S-VHS, PAL) and individual photographs were taken using a video-printer. During the operation, the foxhound lay on one side, mostly the left side, due to the fact that 90% of scoliosis are left-concave scoliosis. Bronchial blocking under bronchoscopic control permitted isolation and the distal parts of the ipsilateral lung (the side facing the surgeon) to be collapsed. The first trocar insertion into the chest cavity is usually made in the sixth intercostal space in the mid-to posterior axillary line through a small skin incision. Ventilation to the side involved is stopped and the lung is collapsed. The collapsed lung provides enough space for the surgeon to perform thoracoscopic surgery. Then, four to five additional cannulae of 10 mm diameter were placed in such a way that the 3-D endoscope, the lung retractor, the irrigation and suction as well as the laser applicator could be inserted allowing complete manipulation and examination of the entire thoracic spine. After the operation, only a few scars of about 2 cm in length will remain, which is a major advantage compared with common dorsal fixation techniques.

The pleura parietalis was cut along with simultaneous coagulation of the crossing segmental vessels. The vertebral body, the intervertebral disc and the rip heads were

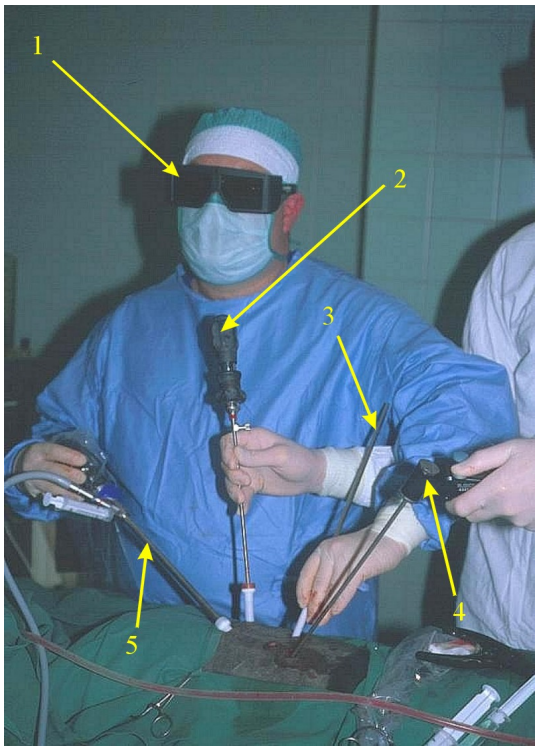

Fig. 5.15: Minimally-invasive laser hemiepiphysiodesis on young foxhound puppies using a 3-D thoracoscope. The surgeon is wearing shutter glasses (1) to get a 3-D view of the operation field. He is holding the 3-D thoracoscopic camera (5) in one hand and endoscopic forceps or the laser applicator (3) in the other. The assistant is holding the suction and irrigation system (4) and the lung retractor (2).

preserved over a length of five vertebrae in doing so. Any bleeding occurring could be stopped using monopolar endoscopic forceps. Considering postoperative MRI, no vessel clips were used.

After preservation of the vertebral bodies, the laser fibre was inserted in a sterile protective cover and laser calibration was performed using the internal automatic energy meter of the Medilas system. A special fibre applicator has been developed to protect the distal end of the fibre from mechanical stress and to provide safe and easy handling for the surgeon. As shown in fig. 5.17, the applicator consists of a hollow tube (stainless steel) of 4 mm outer diameter with a removable tip to allow easy insertion of the fibre. After the surgeon has determined the desired ablation depth from the MR image, the fibre is fixed with a screw in such a way that the distal end of the fibre exceeds the applicator by the length determined.

In imitation of the ablation technique developed from the in vitro investigations, the fibre tip was first of all moved along the surface of the epiphyseal plate with the laser being operated with short pulses to produce only little tissue ablation. Using this technique, the surgeon produced a small trace of ablated tissue which served as a marker for the epiphyseal growth plate allowing good orientation without causing bleeding from the vertebral bodies. The surgeon then performed the hemiepiphysiodesis along this trace, using longer laser intervals of about 20-30 seconds with pulse energies of 0.8 to 1 Joule and a repetition rate of 8 Hz leading to an average power of 6-8 W.

During laser action, the endoscopic objective lens and the tissue surface had to be rinsed every few seconds because of the intense deposition of debris from the laser abla-

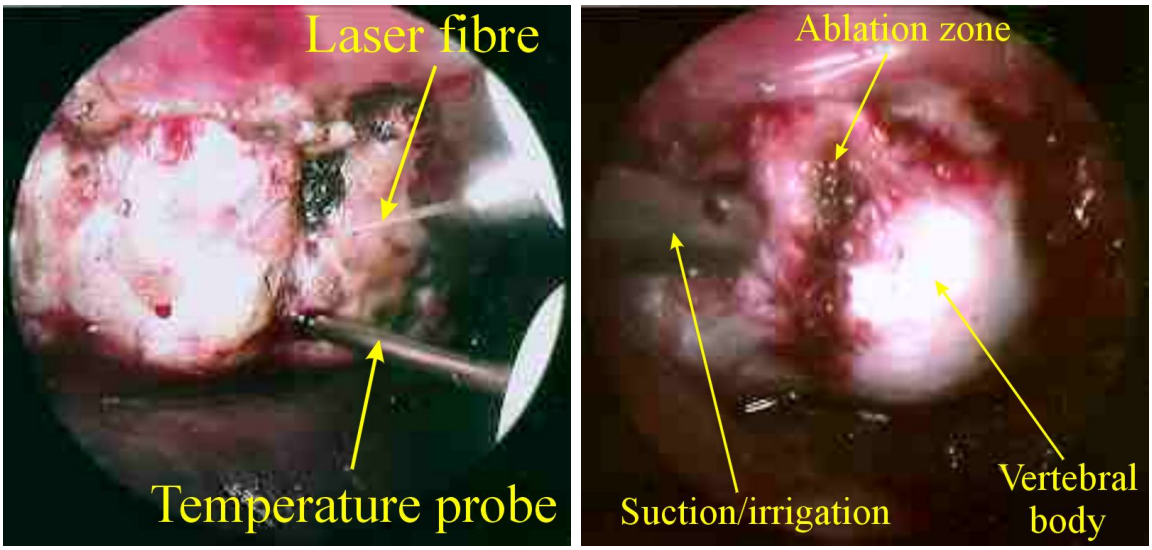

Fig. 5.16: Videoscans of laser hemiepiphysiodesis under a thoracoscopic approach. On the left: laser applicator and fibre-optic temperature probe inside the vertebral body. On the right: the suction and irrigation unit and the epiphyseal plate after laser hemiepiphysiodesis.

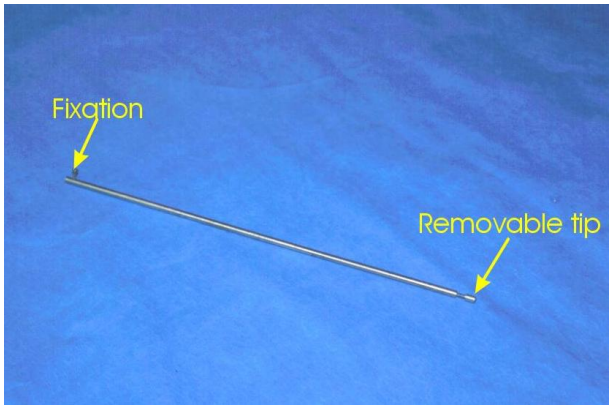

Fig. 5.17: Fibre applicator used for laser hemiepiphysiodesis. The tip can be removed to enable an easy insertion of the fibre during the operation.

tion as well as minor bleeding from the vertebral bodies, extending the operation time for each growth plate by up to about 15 minutes. Fig. 5.16 shows two online video scans of the hemiepiphysiodesis during the operation.
In two cases, the relatively small cranial part of the thorax allowed only treatment of 3-4 epiphyseal growth plates. In all other cases, 5-6 epiphyseal growth plates could be removed. In one case, the laser could not be calibrated and, in another case, the foxhound got respiratory problems so that the operation had to be abandoned and the animals served as a comparison group. In total, 8 foxhounds were treated using the laser hemiepiphysiodesis technique.

5.5.5 Temperature monitoring

A fluoroptic fibre thermometer (Model 3000, Luxtron, USA) was used instead of semiconductor probes for in vivo temperature control during the laser treatment. Data trans-

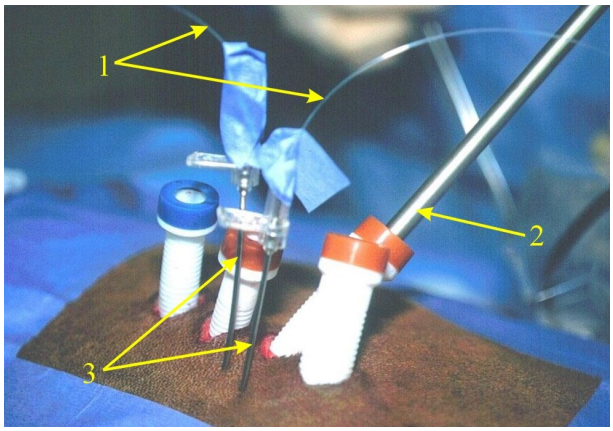

Fig. 5.18: Fixation of fibre-optic temperature probes (1) inside the syringe (3) to protect them from mechanical and laser damage. (2) shows the laser applicator.

mission to a PC was performed via a serial link so that data could be stored for later analysis. A xenon flash lamp, located within the fluoroptic thermometer, produces an exciting pulse of blue light which is transmitted down the fibre to the sensor tip (magnesium fluorogermanate) causing it to fluoresce in the red. This fluorescence is transmitted back to the instrument through the same fibre and is focused onto a photodetector. After the exciting pulse of blue light has terminated, the exponential rate of decay of the fluorescence is measured and correlated with temperature. In contrast to the in vitro experiments, the probes could be fixed only in the vertebra and the intervertebral disc using a syringe to allow stable positioning and protect the fibre against breakage (see fig. 5.18). In both cases, the laser was used to drill the holes for fixing the syringe to the vertebral body and the disc.

5.5.6 Post-operative treatment

After the operation, the animals were extubated and remained in a kennel within the operation building under veterinary supervision for at least 2 hours. They were then brought back to the farm where they grew up together with other animals. Their health and well-being was checked regularly. After 6 months, the foxhounds were x-ray examined to determine whether they already showed scoliotic growth. In almost every case only minor changes in spinal growth could be observed at that time.

The foxhounds were fully grown one year after the operation, so that there was no more growth potential in the epiphyseal plates. A final examination was therefore carried out using x-ray and MRI investigations. Following the examination, the foxhounds were put down and their spines were dissected for additional histological investigations and cryomicrotome cuts.

5.5.7 Results and discussion

The trachea of the three-month-old foxhounds was too long for a double-lumen endotracheal intubation. It turned out though that a bronchoscopically-controlled bronchial blocking under elimination of only the distal parts of the lung provided enough space

for a thoracoscopic laser treatment. The foxhounds tolerated anaesthesia for 4-5 hours without any problems. In total, eight puppies were treated in this study with an additional control group of eight foxhounds without treatment (matched pair technique).

5.5.7.1 Temperature measurements

The results from the temperature measurements showed a slighter rise in temperature than the in vitro data throughout all operations. The temperature thereby varied strongly depending on the position of the probes, thus, direct comparison of the temperature data between the different measurements was difficult. Two typical curves of temperature development during laser hemiepiphysiodesis are shown in fig.5.19 and fig.5.20.

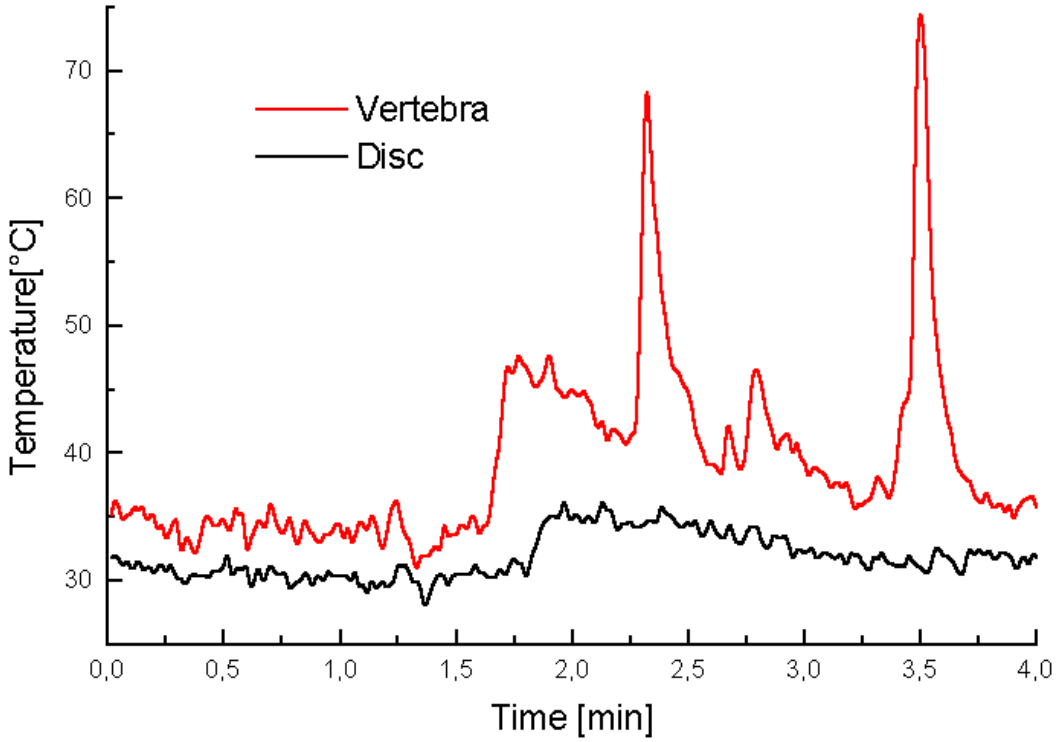

Fig. 5.19: Development of temperature inside the vertebral body and the adjacent disc during in vivo Ho:YAG laser ablation. The distance between the probe and the fibre tip was about 2 mm.

Fig. 5.19 represents the development of the temperature inside the vertebra at a distance of 2 mm from the growth plate and the temperature in the adjacent intervertebral disc. The temperature in the disc thereby remains far below that in the vertebra, showing no peaks. This results mainly from the lower thermal conductivity of the cortical tissue of the epiphysis compared with the more spongiform tissue of the diaphysis. The peaks are thought to originate from blood perfusion inside the vertebral body (see section 4.2.2 and

fig. 4.4). In fig. 5.20, the development of the temperature at a distance of about 4 mm to the fibre tip is shown. It can be seen that the high temperature peaks have vanished and that the overall temperature is about 30°C lower than at half the distance. It can, thus, be assumed that the temperature does not exceed a critical level at a distance of about 4-5 mm from the fibre tip. The curves also show that, in contrast to the in vitro data, the temperature fell rapidly down to a value close to the body temperature immediately after the laser had been switched off. This is due to blood flow and the irrigation liquid. During the in vitro experiments, the temperature remained at a relatively high level after the laser had been switched off due to the lack of blood flow. Although the peak temperature in the vertebral body reached around 75°C during the in vivo experiments, it fell very quickly so that no lasting effects to the nerve roots in the vertebral bodies and the spinal cord are to be expected. None of the animals showed any neurological disorders.

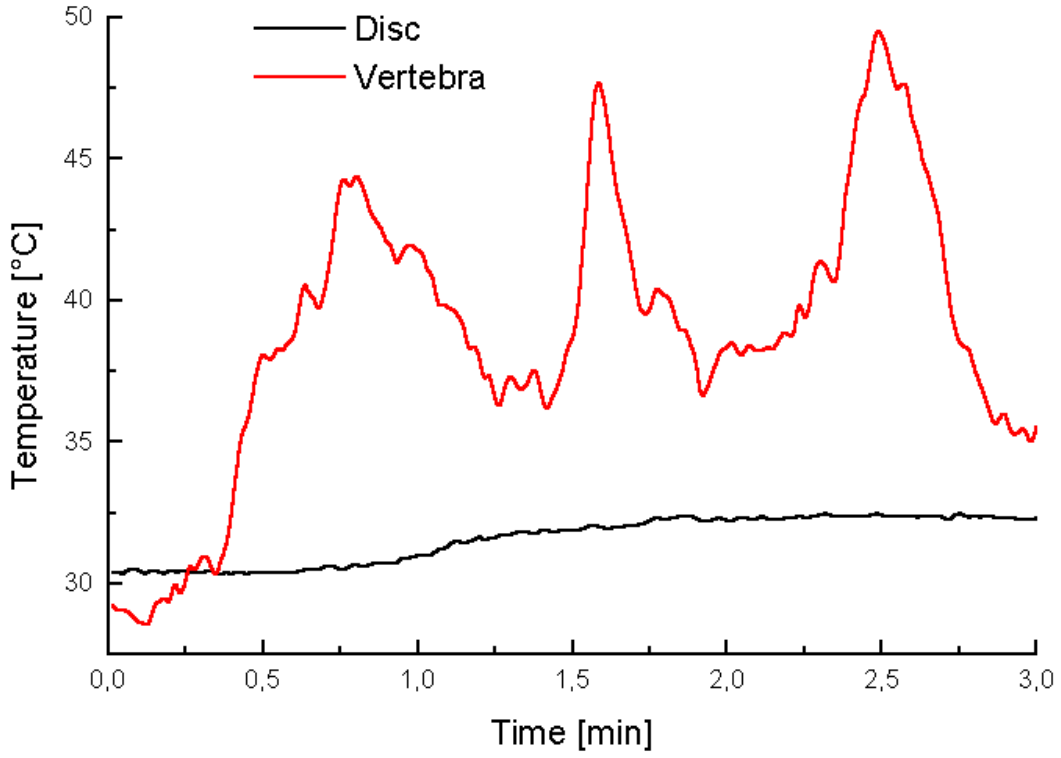

Fig. 5.20: Temperature inside the vertebral body and the adjacent disc during in vivo Ho:YAG laser ablation. The distance between the temperature probe and the fibre tip was about 4 mm.

5.5.7.2 MRI and x-ray investigation

After one year on the farm, the foxhounds were fully grown, but there was still hardly any sign of spinal deformities in the animals' appearance. However, the results from radiography and MRI investigations showed that all of the foxhounds developed alternations to

normal spinal growth within the region of the treated vertebrae. As can be seen in fig. 5.21, the spine showed scoliotic growth in 6 cases and in 2 cases the spinal deformity was kythotic as shown in fig. 5.22.

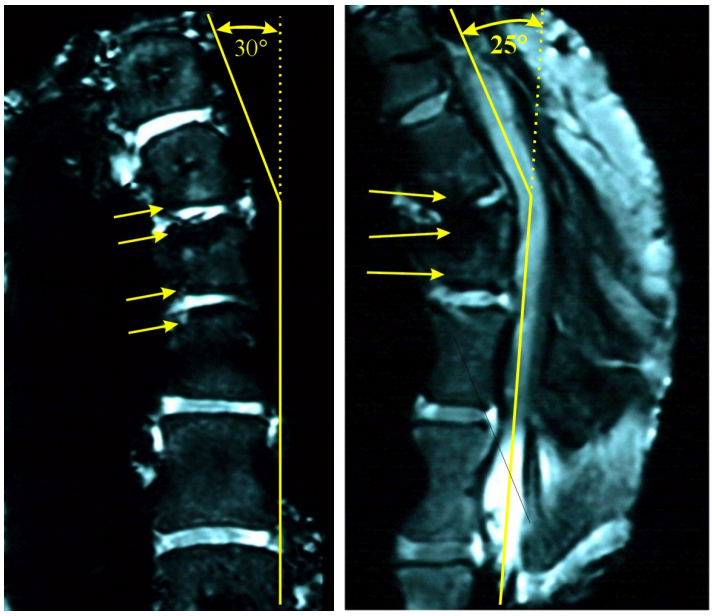

Fig. 5.21: Coronar (left) and sagittal (right) MR image of foxhound one year after laser hemiepiphysiodesis. The arrows in the left image show the epiphyseal plates which were treated with the laser. The scoliotic deviation of the spine is about 30 degrees. The image on the right shows a kythotic deviation of the spine with a curvature of about 25 degrees.

This result shows that all of the vertebral bodies that had been treated with the Ho:YAG laser developed abnormal growth. In 75% of the cases, the desired effect of inhibition of growth on one side, i.e. the side with laser hemiepiphysiodesis, could be achieved. However, the degree of curvature did not exceed 30° and might not be sufficient to compensate severe scoliotic growth.

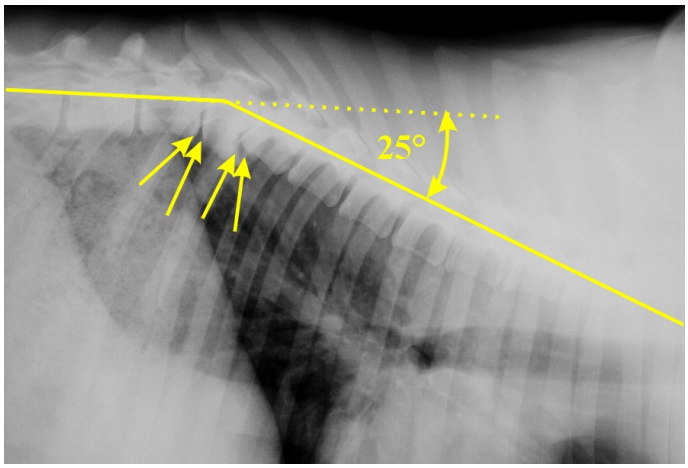

Fig. 5.22: X-ray image of foxhound one year after laser hemiepiphysiodesis showing a kythotic deviation of the spine of about 25 degrees. The arrows indicate the alternation in vertebral growth.

5.5.7.3 Cryo-mictrotome and histological investigation

The post-operative investigation with the cryomicrotome, which was proven to be very useful during in vitro experiments already, was also performed for in vivo investigation. After dissection, the spinal segments were cut in the coronal plane in order to show scoliotic deviation on spinal growth. The spine shown in fig. 5.23 corresponds to the MRI

image on the left in fig. 5.21. Alternations in vertebral growth due to laser treatment are clearly visible (arrows).

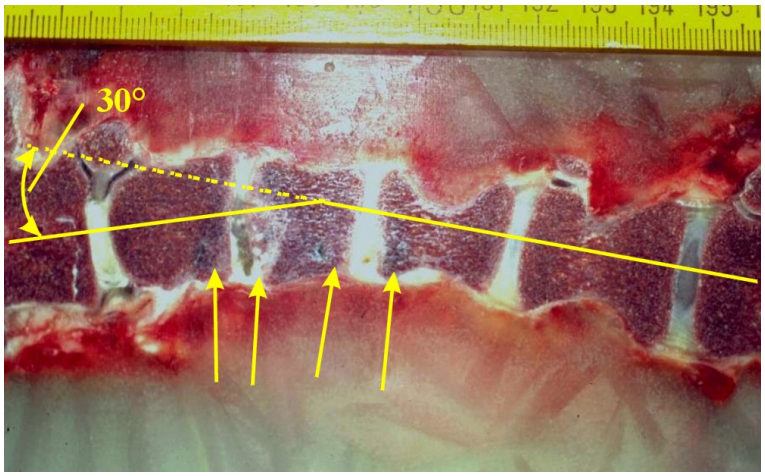

Fig. 5.23: Coronal cryomicrotome cut of the spine one year after laser treatment. The spine corresponds to the one shown on the left in fig. 5.21. A scoliotic deviation in spinal growth of 30° can be seen. Alternations in vertebral growth due to laser treatment are clearly visible (arrows).

5.6 Conclusion

During extensive in vivo experiments, the Ho:YAG laser has proven to be a powerful tool for the **precise**, **fast** and **effective ablation** of cartilage tissue, thus, providing a new gentle operation technique for the treatment of idiopathic scoliosis.
These initial results imply, that it is possible to produce a change in spinal growth through laser hemiepiphysiodesis. Nevertheless, in order to develop this operation technique for clinical application, it is necessary to determine a tight correlation between the number of ablated growth plates and the extent of scoliotic growth, thus, further investigations are necessary.
From a clinical point of view, the ablation of a maximum of six epiphyseal growth plates might not have been enough to induce significant scoliotic growth and might be a reason why the change in spinal growth was not as strong as might be needed for an effective treatment of severe idiopathic scoliosis. In addition, the neurocentral cartilage in the vertebral bodies of foxhounds might have had a negative influence on scoliotic growth.

Animal experiments with primates might have been more successful due to their similarity to humans with an upright position of the spine. These experiments, however, would be extremely costly and difficult to carry out due to ethical aspects. However, according to the given goal of partial removal of the vertebral growth plate as a minimally-invasive scoliosis treatment, it was shown that high-precision, minimal thermal damage to adjacent tissue and a sufficiently high ablation rate could be achieved during in vivo operations. The chosen 3-D thoracoscopic operation technique in combination with the Ho:YAG laser has proven to be successful and reliable with regard to laser tissue ablation, laser handling and safety in sensitive structures. In addition, the results of this work can be used to adapt the operation technique to other, similar clinical applications, where a precise ablation of hard tissue without thermal damage to adjacent structures is essential, such

as the treatment of herniated discs and stenosis of intervertebral foraminae.
Alternative laser ablation might be possible in the future due to newly developed sapphire optical fibres with high transmission rates of more than 80% at wavelengths of up to 3.5 microns. This would allow the endoscopic use of Erbium doped lasers at wavelengths of around 3 μm where water has its strongest absorption peak. These fibres, however, have not been available when our work was started.

Chapter 6

Plasma-mediated laser bone ablation

Very clean and well-defined removal of tissue without any evidence of thermal or mechanical damage to collateral structures can be achieved by means of plasma-mediated ablation, if the appropriate laser parameters are chosen (see section 2.3).
Picosecond and femtosecond laser pulses permit the generation of high peak intensities with considerably lower pulse energies than those of ns laser pulses. Plasma energy and, thus, disruptive effects can be reduced with these extremely short pulse durations (see section 2.3.1). Moreover, spatial confinement and predictability with regard to laser tissue interaction is strongly enhanced. This plays an important role in clinical laser applications based on very precise tissue ablation, such as photo-refractive surgery on the cornea of the eye [Bil97],[Mül97],[Lub99], glaucoma treatment [Keß00] or ablation of neural tissue [Göt96].
Since plasma-mediated laser ablation is capable of removing only small volumes of tissue, it as yet has only limited applications in clinical treatment. Nevertheless, due to the development of new powerful picosecond and femtosecond laser systems, the number of applications will soon increase. Another advantage of plasma-mediated ablation is the independence of tissue structure. Therefore, even hard tissue like cortical bone can be removed easily using this technique. In the following study, the main interest lies in the clinical application of **laser microsurgery** (LMS) used for treating stenosis on vertebral foraminae and necrosis of the head of femur [Bon99]. For all of these applications, precision in tissue ablation and non-thermal laser-tissue interaction is an essential requirement, whereas the ablation rate itself is of secondary importance.
In this work, two powerful ultra-short pulse laser systems were compared with regard to their ablation rates and precision of plasma-mediated ablation on cortical bone tissue (bovine thigh bone). In addition, histological cuts were made in order to show that the process of plasma-mediated tissue ablation caused no thermal damage to collateral tissue.

6.1 Model of plasma-mediated tissue ablation

As described in section 2.3, plasma-mediated tissue ablation is due to the mechanical decomposition of ionized molecules within the plasma. To determine the dependence of

ablation depth on incident laser intensity, a new model based on *Maxwell's equations*, was introduced by [Nie96]. Assuming that the plasma electrons are performing oscillations induced by the incident electromagnetic field at its frequency ω, the plasma absorption coefficient is derived as

$$\alpha_{pl} = \frac{\nu_{ei}}{nc} \frac{\omega_{pl}^2}{\omega^2 + \nu_{ei}^2} \tag{6.1}$$

with ν_{ei} being the mean collision rate of free electrons and ions. For cold laser plasmas, i.e. $\nu_{ei} \ll \omega$, equation 6.1 can be simplified to

$$\alpha_{pl} = \frac{\nu_{ei}}{nc} \frac{\omega_{pl}^2}{\omega^2} \tag{6.2}$$

Therefore, plasma absorption is enhanced in the IR region of the spectrum. Since $\omega_{pl}^2 \sim$ N and $\nu_{ei} \sim N$, the important relation $\alpha_{pl} \sim N^2$ is obtained stating that the absorption is a non-linear function of the free electron density and, thus, of the absorbed energy itself. This model describes laser tissue ablation very well. However, if the energy density reaches a second threshold I_{pl}, the ablation depth per pulse saturates. This is due to *plasma shielding* at high plasma temperatures or high electron densities within the plasma where succeeding laser radiation is absorbed, thereby heating up the plasma. All abundant energy is, thus, dissipated to heat and does not contribute to a further increase in ablation depth.

6.2 The laser systems

The investigation of plasma-mediated ablation of bone tissue was performed using a Ti:sapphire laser system at the Max-Born-Institute of Nonlinear Optics and Spectroscopy in Berlin. The system layout is shown in fig. 6.1. A Ti:Sapphire oscillator (Spectra Physics Tsunami) is pumped with an argon-ion laser (Spectra Physics 2080 A-12 Beamlok). Chirped pulse amplification is performed using a stretcher/compressor unit (Quantronix Model 4800) and a Ti:Sapphire regenerative amplifier (Quantronix 4800), pumped by the frequency doubled output of a Q-switched Nd:YLF laser (Quantronix 527). Pulses with durations down to 225 fs (autocorrelation function) and energies of up to 400 μJ were obtained at repetition rates of up to 1 kHz. The wavelength of the pulsed light is tunable and was about 820 nm during the experiments.

As a comparison, additional experiments were performed at MRC-Systems GmbH in Heidelberg using 20 ps pulses generated by a Nd:YAG laser system (*HARP*, Time Bandwidth Products). The HARP laser system consists of three components, a *seed laser oscillator*, a *regenerative amplifier* and a *power amplifier*. Pulse formation in the seed laser oscillator is based on a diode pumped Nd:YVO crystal in combination with a semiconductor saturable absorber mirror (SESAM) [Kel96]. The initial pulses of 10 nJ are amplified by a Q-switched Nd:YAG regenerative amplifier to pulse energies of

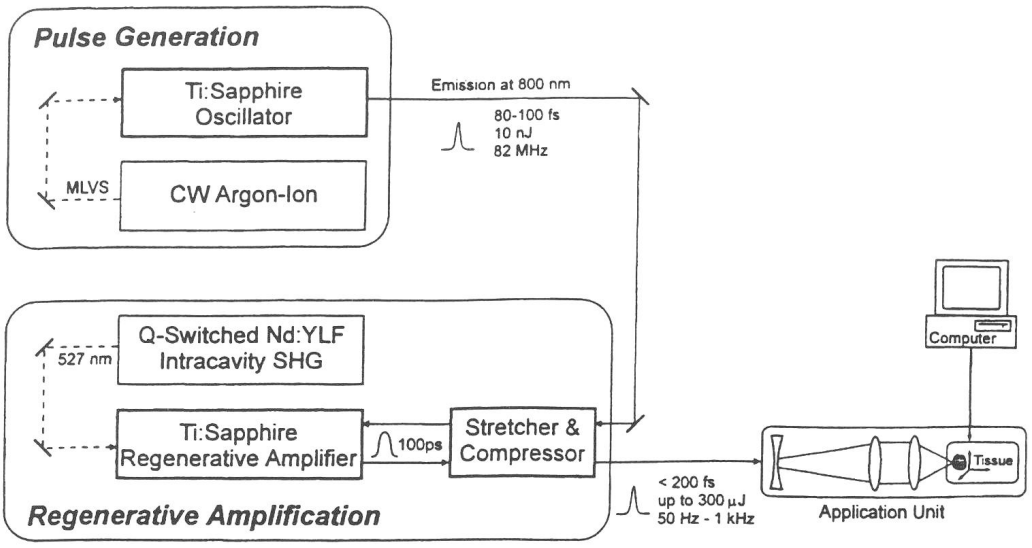

Fig. 6.1: Diagram of the experiments on plasma-mediated laser ablation of bone tissue with the Ti:Sapphire fs-laser system and the application unit. The ultrashort pulses are generated in the Ti:Sapphire oscillator (*top*), then regeneratively amplified (*bottom*) using chirped pulse amplification and directed into the computer controlled application unit (*right*).[Lös98]

400 μJ with repetition rates of 4 kHz and a mean power of up to 1.6 W. In a last stage the power amplifier consisting of a Nd:YAG laser head (CEO minirod) is passed four times leading to a sixfold amplification resulting in a maximum output power of 10 W.

The set-up for the experiments with the picosecond Nd:YAG laser is shown in fig. 6.2. Since the laser system has a fixed repetition rate of 4 kHz an optical "chopper" was used to reduce the mean repetition rate to 1 kHz. This was necessary because of thermal effects during plasma ablation at higher repetition rates (see chapter 4.3).
For both lasers the beam diameter was increased by means of a Galilean telescope and then focused onto the tissue surface at normal incidence. For the Ti:Sapphire laser a lens with 9 dpt (111 mm) focal length and for the Nd:YAG laser a lens with 50 mm focal length were used respectively. The bone sample was mounted onto a translation stage, which could be moved in the $x - y$ plane by means of computer-controlled stepping motors. During laser action, the sample was moved along parallel lines (2 mm) in the x axis at a velocity of 0.8 mm/s. The distance between the lines was 50 μm. Optimum plasma spark generation was used as alignment criteria for adjustment of the z-position along the optical axis.
Due to high power densities, the spot size diameter had to be measured with the "knife-edge" method. Thereby, a razor blade is moved through the beam at different positions along the beam axis close to the estimated z-position of the focal spot. The transmitted laser power is determined using a power meter. Data is then plotted and differentiation leads to a *Gaussian* curve from which the spot size diameter is determined ($1/e^2$ decay)

[Roh99].

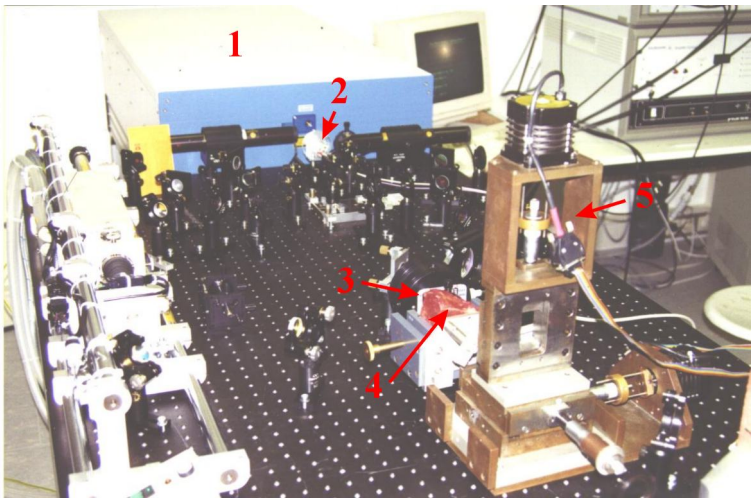

Fig. 6.2: Set-up of the experiments on plasma-mediated laser ablation of bone tissue with the *HARP*© ps laser system. (1) laser, (2) chopper, (3) focussing lens (f = 50 mm), (4) bone sample and (5) mount with stepping motors.

For plasma-mediated laser ablation fresh cortical bovine thigh bone was used. To ensure a uniform ablation the periosteum was dissected. During laser ablation the tissue surface was sprayed with saline solution to prevent drying. After laser ablation the tissue sample was put in mounting medium and remaining water was replaced with alcohol. The sample was then cut with a diamond saw to determine the ablation depth using a scanning electron microscope (SEM). For this investigation, the sample has to be absolutely dry, so that no material is vaporized inside the vacuum chamber of the SEM. Thus, after irradiation the specimens were preserved in a 10% formalin solution, dehydrated in a series of graded ethanol and dried using a *critical point dryer*[1] (CPD). Finally, the samples were coated with a gold layer (20 nm) using a sputter coater to prevent electro-static charge at the surface of the sample.
For histological investigation some samples were decalcified and dyed with *Ladewig* agent for examination with a light microscope (LM).

6.3 Results and discussion

Fig. 6.3 shows the results from the spot-size measurements. According to [Koe92] the beam width is given by

$$\omega(z) = \omega_0 \sqrt{1 + \left(\frac{\lambda z}{\pi \omega_0^2}\right)^2}. \tag{6.3}$$

From this, the spot-size diameter for the experiments with the Ti:Sapphire fs-laser was determined to be $44 \pm 4\ \mu m$ in horizontal and $50 \pm 4\ \mu m$ in vertical direction. Due to the smaller focal length the spot-size diameter for the Nd:YAG ps-laser reached 12 ± 2

[1]Inside a small pressure chamber the tissue samples are embedded with liquid CO_2 which is heated until a mixed phase (p >85 bar, T>40°C) is reached. The pressure is then reduced slowly resulting in a gentle drying without affecting tissue structures and with almost no shrinking (typically < 5%).

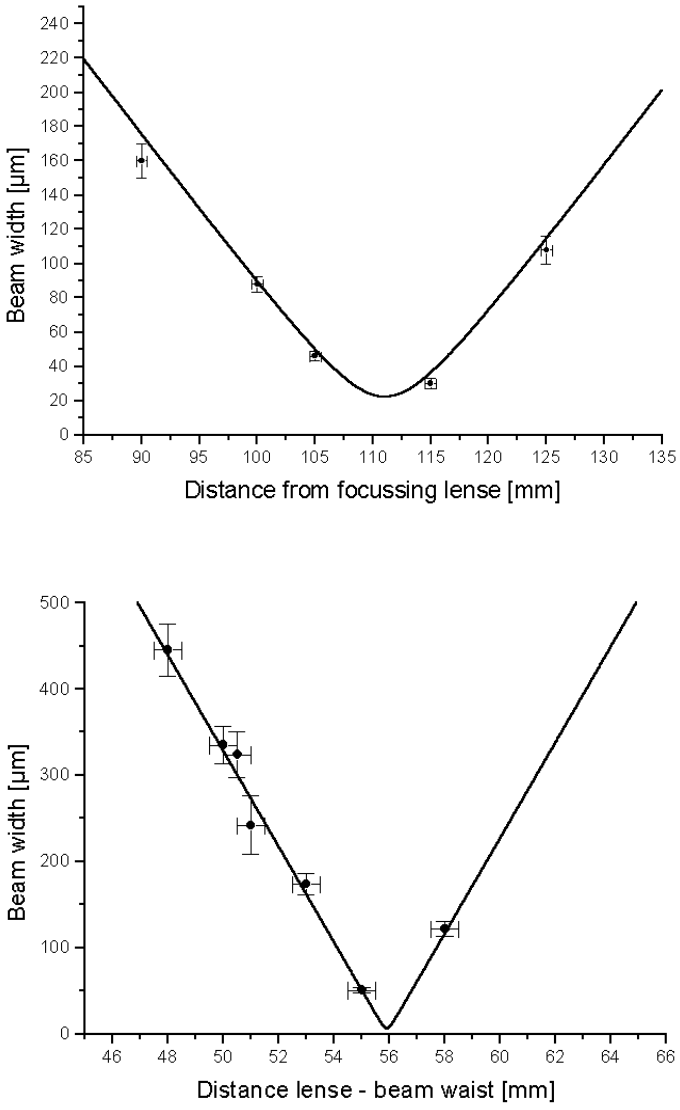

Fig. 6.3: Evaluation of the spot size diameter with data from the "knife-edge" measurements, using a two parameter fit (equation 6.3). For the Ti:Sapphire laser (top) a spot-size diameter of 44 ± 4 μm in horizontal and 50 ± 4 μm in vertical direction was determined. For the Nd:YAG laser (bottom) a spot-size diameter of 12 ± 2 μm in horizontal and 14 ± 2 μm in the vertical direction, was calculated respectively.

With a pulse energy of 400 μJ and a pulse duration of 225 fs, the focal energy density of the Ti:Sapphire laser reached about 21 J/cm^2, leading to a maximum power density of $9 \cdot 10^{13}$ W/cm^2. With a maximum pulse energy of 1.8 mJ for the Nd:YAG laser a focal energy density of up to $1.2 \cdot 10^3$ J/cm^2 could be achieved. The pulse duration of 20 ps led to a power density of $5.8 \cdot 10^{13}$ W/cm^2.

Fig. 6.4 and fig. 6.5 show quantitative results after laser irradiation using single pass ablations performed at various pulse energies at a repetition rate of 1 kHz. To evaluate the depth, the irradiated samples were cut in half and the depth of the excision was determined with the SEM using a micrometre scale. A slight scatter of the measured data occurred due to the inhomogeneous structure of the samples.

The ablation threshold for plasma mediated ablation of bone tissue with the

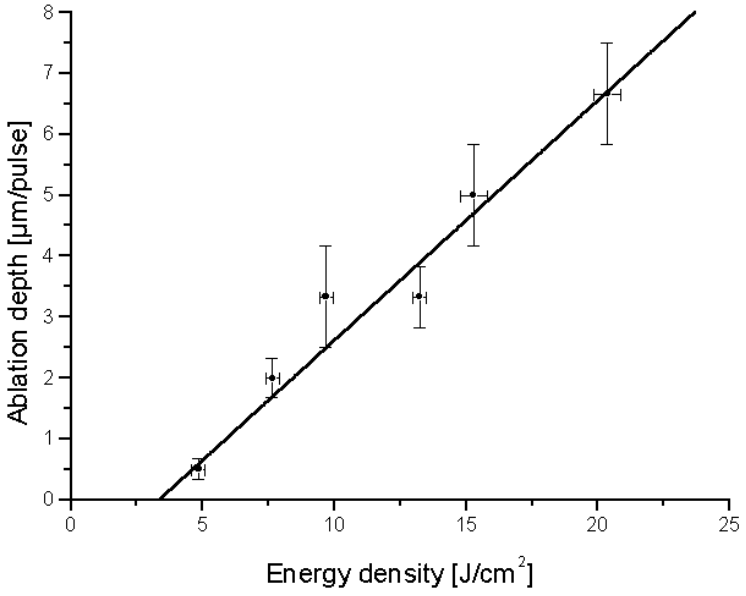

Fig. 6.4: Ablation curve of plasma-mediated laser ablation of cortical bone tissue (bovine thigh bone) with 225 fs pulses (autocorrelation function) from the Ti:Sapphire fs laser system at 820 nm . Using a linear fit (slope = 0.4) the ablation threshold was determined to be 3.5±1 J/cm^2.

Ti:Sapphire laser and the Nd:YAG laser could be determined to be 3.5±1 J/cm^2 and 80±10 J/cm^2 respectively.

According to fig. 6.4 and fig. 6.5 the shorter femtosecond pulses exhibit a significantly higher efficiency than the picosecond pulses. The slope for the fs pulses in fig. 6.4 is about 0.4. For the ps pulses in fig. 6.5 it is only about 0.05. Although the wavelength of the Ti:Sapphire laser (820 nm) and the Nd:YAG laser (1064 nm) differ by a factor of 1.3, this does not contribute to the phenomenon of increased femtosecond ablation efficiency, since interaction is based on a plasma effect, not on linear absorption [Nie96] [Lös98]. With shorter laser pulses induced breakdown already occurs at larger laser beam diameters before the focal spot is reached. Thus, the volume of the plasma is expected to be larger. This may result in larger volumes of material being ablated by a single pulse, thus, leading to a higher ablation efficiency.
Using the efficiency measurements, the time needed for the ablation of a given amount of tissue can be estimated.
The Ti:Sapphire laser is capable of generating 225 fs pulses with an energy of 400 μJ at a repetition rate of 1 kHz. Due to slow scanning of the laser beam over the tissue surface, pulse overlay was approximately 60-fold for the Ti:Sapphire laser and 18-fold for the Nd:YAG laser. Assuming an optimal scanning speed, i.e. single pulse excision, the calculated time needed for the ablation of 1 mm^3 of cortical bone tissue is about 60 seconds (spot size $\approx 50\ \mu m$).
The Nd:YAG laser generates 20 ps pulses with a maximum energy of 2.4 mJ at a repetition rate of 4 kHz. With a spot size diameter of 12 μm, the ablation time for 1 mm^3 would be about 25 seconds.

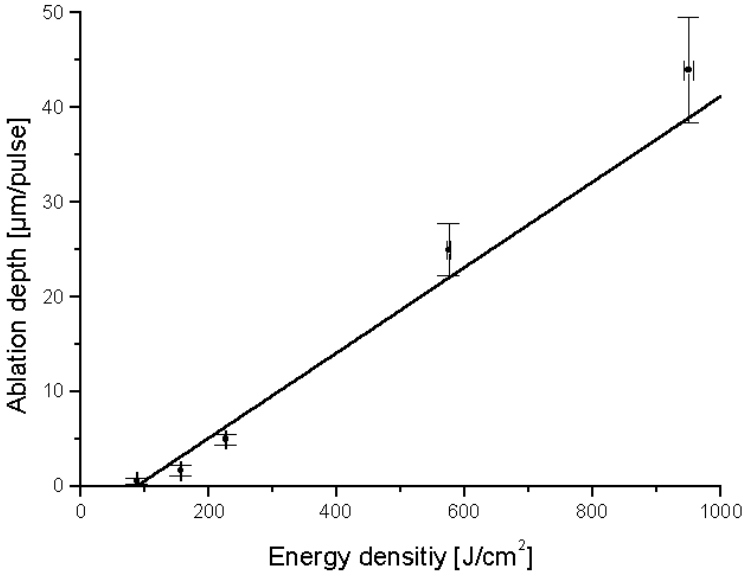

Fig. 6.5: Ablation curve of plasma-mediated laser ablation of cortical bone tissue (bovine thigh bone) with 20 ps pulses (FWHM) from the Nd:YAG ps-laser system at 1064 nm . Using a linear fit (slope = 0.05) the ablation threshold was determined to be 80±10 J/cm^2.

6.3.1 SEM and histological investigations

Fig. 6.6 shows an SEM image of a bone tissue sample after irradiation with 20 ps laser pulses at pulse energies of 2 mJ. Magnification is 50-fold (bar = 1 mm) on the left-hand side. The right-hand side shows a further twofold magnification of the marked section (bar = 100 μm). The size of the pattern was 2 × 2 mm and laser ablation was repeated 2 times.

It can be seen from SEM investigation that the tissue ablation has been very precise and cavitation and mechanical alterations of the edges can not be found.

In order to investigate the histopathological structure of the excisions, samples were cut in slices of 10 μm thickness. Fig. 6.8 shows two photomicrographs of *Ladewig* stained cortical bone tissue exposed to 350 μJ with 20 ps laser pulses. The image on the left-hand site shows an overview of the excision at a lower magnification (bar = 400 μm), demonstrating the absence of long-range structural changes caused by means of irradiation. The vertical edges and the lower horizontal edge mark the boundary of the laser excision. The right-hand image shows a magnification of the lower horizontal edge. The bar represents a distance of 10 μm. The quality of the laser cut is exceptionally high and exceeds a mechanical cut e.g. with a medical (pneumatic) saw.
If the scans are repeated more often, deeper excisions can be achieved. During laser ablation, tissue fragments are ejected. Thus, debris of ablated material can often be found covering the edges and the bottom of the excisions, as shown in fig. 6.8. After irrigation most of the debris can be removed by rinsing the tissue with saline solution. The geometry of the excisions often appears to be slightly distorted from its original shape. The top edges apparently moved outwards. These effects are due to the dehydration process of the tissue prior to SEM examination (see above).

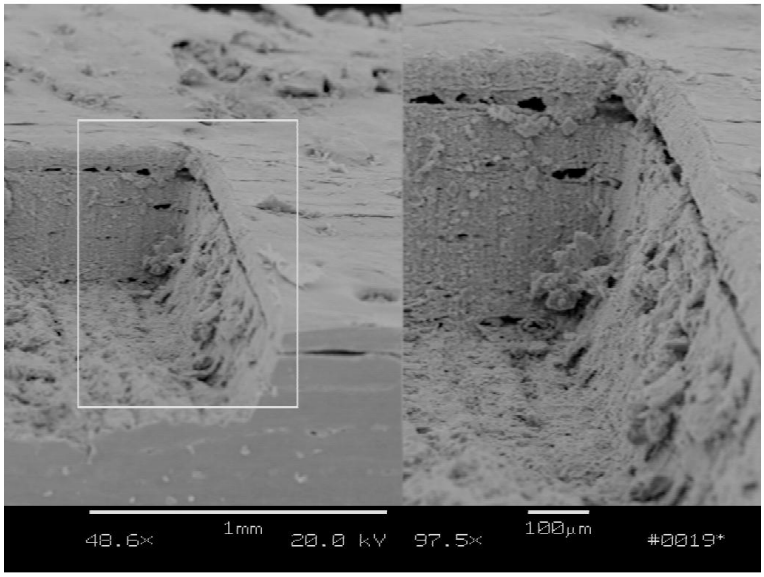

Fig. 6.6: SEM image after plasma-mediated laser ablation of bovine cortical bone tissue with 20 ps pulses from a Nd:YAG laser ($\lambda = 1064$ nm). Pulse energy was 2 mJ at a repetition rate of 1 kHz. Magnification on the left is $\times 50$ and on the right $\times 100$.

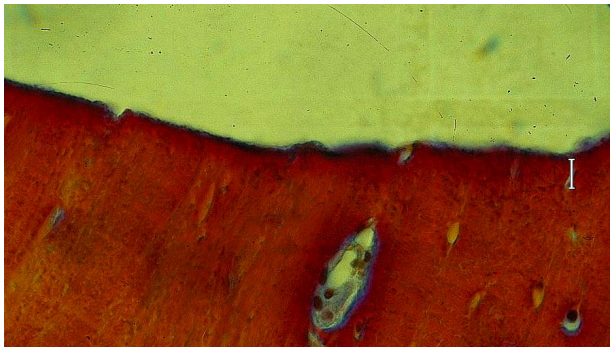

Fig. 6.7: LM image after plasma-mediated laser ablation on bovine thigh bone at 820 nm with 225 fs pulses. Pulse energy = 400 J, repetition rate = 1 kHz.

6.4 Conclusion

The experiments with the ps and fs-laser system showed that plasma-mediated tissue ablation of cortical bone is possible with sufficiently high ablation rates and accuracy for the clinical application of microsurgical treatment. In addition, according to the results from histological investigations, no thermal damage occurred to collateral structures. Compared to a zone of thermal damage of 50-100 μm for bone ablation with the Ho:YAG laser [Sch92][Cha90] and 100-200 μm for the CO_2 laser [Sch92][Fri00], plasma-mediated bone ablation is very safe, thus, the use of new compact ps and fs-lasers in combination with already existing laser probes [Göt99] enables the non-thermal ablation of bone tissue and, therefore, makes new clinical applications possible, especially in orthopaedics in the treatment of stenosis on vertebral foraminae, necrosis of the head of femur [Bon99] and ear-nose-throat (ENT) surgery. Since threshold fluence needed for initiating the ablation process is lower for the shorter femtosecond pulses than for picosecond pulses, lower pulse energies can be used for the removal of bone tissue if femtosecond laser pulses are applied.

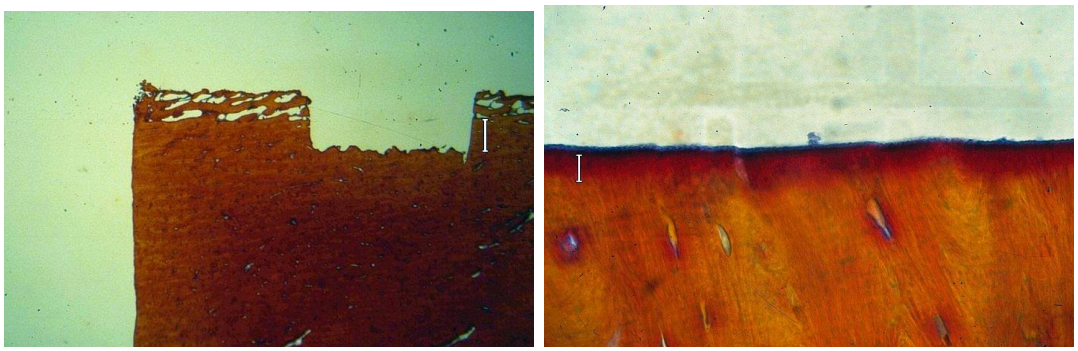

Fig. 6.8: LM image of histological cut after plasma-mediated laser ablation of bone tissue with the *HARP*© ps laser system. Left: very precise ablation with sharp edges and no signs of cavitation in the collateral tissue (bar = 100 μm). Right: no thermal damage to adjacent tissue (bar = 10 μm).

This results in reduced shockwave effects. In addition, in comparison to longer picosecond laser pulses from the Nd:YAG laser, the ablation with the Ti:Sapphire femtosecond pulses was found to be more efficient. However, due to its high pulse energy of up to 2.5 mJ and repetition rates of up to 4 kHz, the picosecond laser system may reach high ablation rates of cortical bone tissue of about 10 mm^3/min. This time is short enough to be of clinical relevance. For these laser parameters, the ablating beam should be scanned over the tissue surface ten times faster than in this experiment. From a technical point of view, such scanning speeds can be easily achieved.

Chapter 7

LITT of bone tumours under MRI temperature control

This part of the dissertation concentrates on laser-induced minimally-invasive treatment of benign bone tumours. There are many types of benign and malignant bone tumours of which the **osteoid osteoma** (OO) is the most common of the benign ones.
The aim of our new laser treatment was to thermally destroy the tumour by means of photo-coagulation which occurs at tissue temperatures above **50°C** applied for more than 30 seconds. Using an optical fibre, this technique allows for easy destruction of tumour cells without the removal of bone tissue.
During the study, 3 different laser systems including a Ho:YAG laser (Medilas H, Dornier, Germany), a Nd:YAG laser (SL 905 T, Spectron, Germany) and a compact diode laser (Medilas D, Dornier, Germany) were evaluated with regard to their applicability during laser induced interstitial thermotherapy (LITT).
To date, only one research group is known to use LITT as a treatment for OO [Gan98]. They use computer tomography (CT) for intra-operative tumour localization and navigation of the laser which exposes the patient to strong radiation [SDB98]. In addition, precise non-invasive temperature monitoring during the laser application is not possible using CT.
In contrast, our newly invented treatment is performed under MRI guidance and uses the latest imaging technology for fast, i.e. online, temperature control during the coagulation procedure.

7.1 The osteoid osteoma

An osteoid osteoma (OO) is an entity that, in spite of its completely benign behaviour and small size ($\leq$ 2 cm), is of great concern to the patient because of the severe pain with which it is associated [Pic89]. The lesion consists of a small, round or oval *nidus* of osteoid and/or woven bone in **highly vascularized** tissue evoking an intense reaction of the surrounding structures.
The nidus is blood red, soft and richly innervated by nerve fibres, thereby evoking **consid-**

erable pain which is frequently mistaken for a neurotic complaint, thus, causing delays in diagnosis ranging from months to years [O'Co98].
Some 70% of patients are less than 20 years old and more than 80% occur in long bones of which the most common are the femur (34%), tibia (23%), humerus (6%) and talus (5%). Fig. 7.1 shows the sex, age and skeletal distribution of OO.

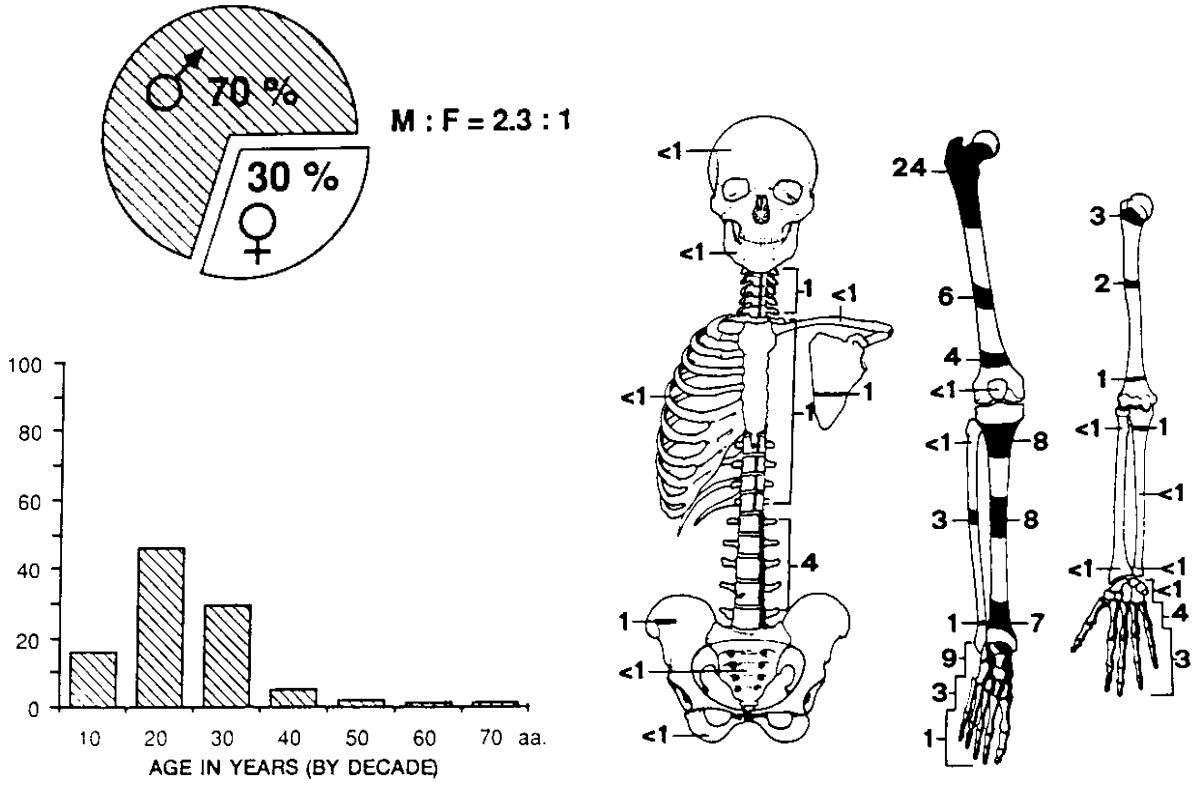

Fig. 7.1: Sex, age and skeletal distribution of osteoid osteoma (635 cases).[Pic89]

An OO located in the spine often results in muscular spasm due to irradiant effects from the nidus with a resultant curvature of the spine (scoliosis). Some OO of long bones present in infancy and located close to a growth epiphysis result in a lengthening of the segment. This acceleration in growth, if asymmetric, may result in varus or valgus joint deformity. Due to its high vascularization, the OO is clearly visible on x-rays as well as on MRI images. Fig. 7.2 shows an x-ray image in the frontal plane of an OO in the tibia bone. The nidus is clearly demarcated (arrow). In fig. 7.3, the MR image of a transversal cut through the tibia shows the OO (arrow) as a region of hyperintensity inside the otherwise dark cortical bone [Hac97].

Most nidi are buried deep within a tremendously thickened corticoperiostal reactive bone covering. The surgeon does not want to excise the entire extent of the perinidal reactive tissue, since removal of this covering would compromise the cortical strength of the bone with the **threat of fracture** on weight bearing, thus, requiring the use of a cast for extra weeks.

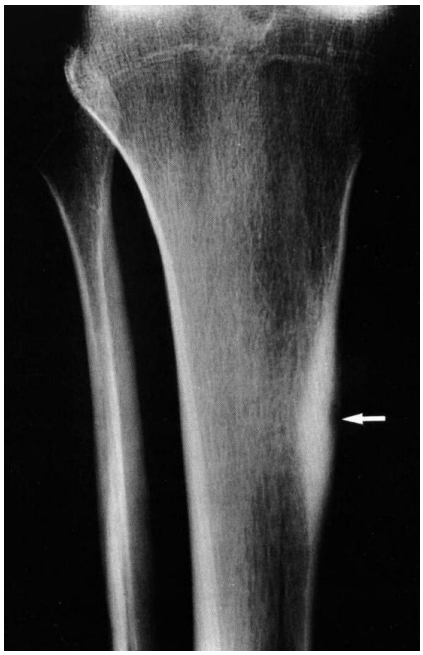

Fig. 7.2: X-ray image of 19 year old male. The arrow marks the OO of the medial tibia. The nidus is clearly demarcated.[Fre98]

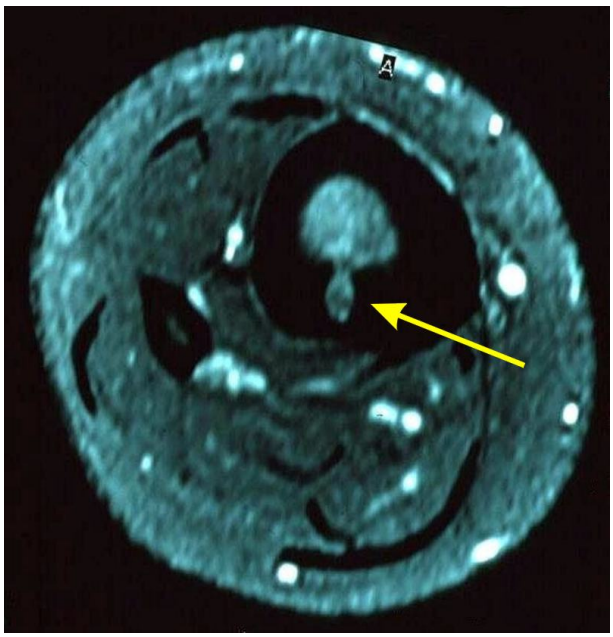

Fig. 7.3: T_1 weighted MR image of 22 year old male after application of contrast medium. The arrow marks the OO of the medial tibia. The nidus shows up as hyperintense region.

7.2 Experimental set-up

To facilitate the puncture of the nidus and to assure precise needle placement, a new fully MR compatible puncture system has been developed. Fig. 7.4 shows the device consisting of an outer ring with holes to assure precise guidance of the puncture needle. The ring is fixed on a plate which also acts as a fixation for the tissue sample. The ring allows for punctures in the transversal plane in steps of 5°. The device is made of acrylate and is invisible for MRI.
Sheep thigh bones were used for in vitro investigation. Since none of the sheep actually developed an OO, the tissue sample had to be preserved. Throughout this study, preservation was performed in the same manner to assure comparable conditions.

Using a pneumatic drilling machine, two to three holes of 2.1 mm in diameter were drilled into the cortical substance of the thigh bone. These holes were then filled with trabecular bone from the head of the femur. An artificial nidus was, thus, produced thereby. Holes for the fluoroptic temperature probes were drilled perpendicular to the artificial tumour, such that the distal end of the probes was located at a distance of a few millimetres from the artificial tumour. The tissue sample was then fixed on the MRI table and the nidus was located precisely using a hand receiver coil.

To make sure that our puncture method was precise and reliable ($p < 0.05$), we performed ten punctures using a Gadolinium pellet with a diameter of 0.8 cm, which represented the tumour (see fig. 7.5).

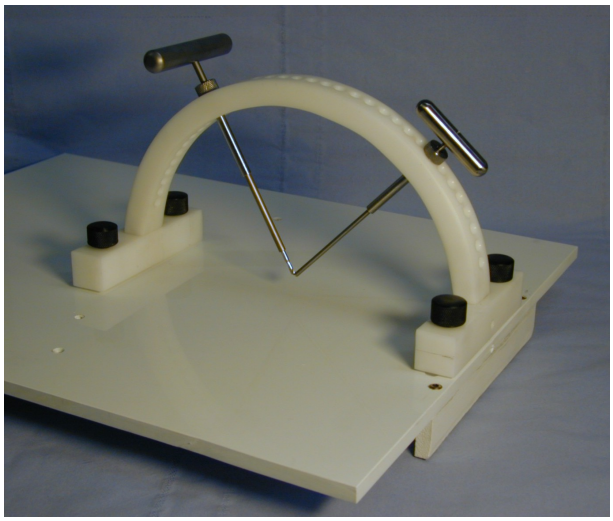

Fig. 7.4: Prototype of puncture fixation system. The ring allows for precise guidance of the puncture needle in the transversal plane in steps of 5°.

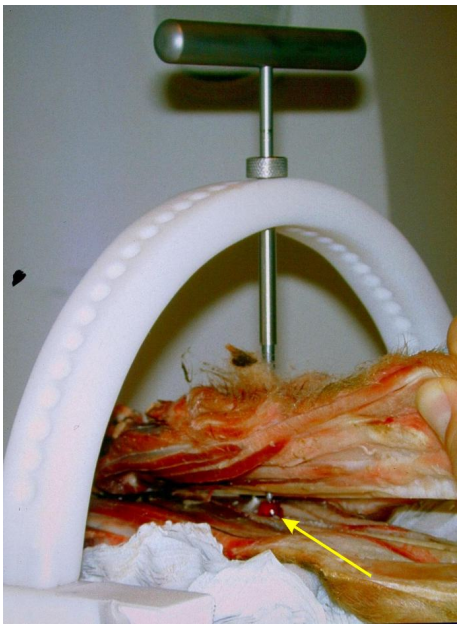

Fig. 7.5: Evaluation of the puncture algorithm and precision of the puncture device using a Gd pallet (arrow). The sheep thigh bone was cut in half so that easy positioning of the pallet could be achieved.

Throughout the evaluation of the three laser systems, application of laser light was performed using a fused silica bare fibre. During experiments with the Ho:YAG and the diode laser, the fibre was connected directly to the laser via a special mount. For the Ho:YAG laser, external calibration was needed whereas the diode laser performs self-calibration each time the system is started. Measured output power was between 90% and 95% of the chosen display value for the diode laser, and 75% to 90% for the Ho:YAG laser. Output power for the Nd:YAG laser was adjusted using a calibrated power meter (Vector, S 310 D, Laser 2000, Germany).
The typical optical fibres used for laser coagulation consist of three different layers as shown in the left-hand illustration of figure 7.6. The *core* - usually made of silica - is the light transmitting region. The *cladding* is the cylindric optical layer that, together with the core, builds the optical waveguide. Light guidance occurs due to total reflection on the boundary between the core and the cladding according to *Snellius' law*

$$sin\,\epsilon_g = \frac{n_{clad}}{n_{core}} \tag{7.1}$$

with n_{clad} being the refractive index of the cladding and n_{core} the refractive index of the core and $n_{core} > n_{clad}$. Thus, the maximum angle Θ for which light is guided inside the fibre is given by

$$\Theta = arcsin\sqrt{n_{core}^2 - n_{clad}^2} \tag{7.2}$$

For optical fibres, equation 7.2 is often written as

$$NA = \sqrt{n_{core}^2 - n_{clad}^2} = sin\,\Theta \tag{7.3}$$

with NA being the numerical aperture.

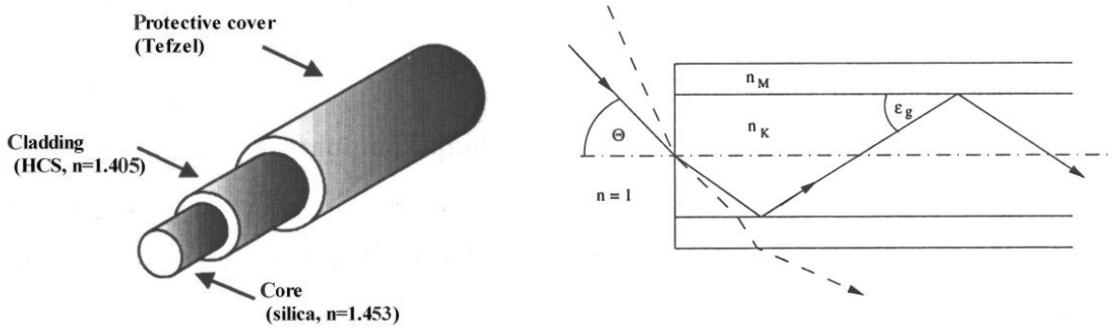

Fig. 7.6: Left: structure of bare fibre with step index. Right: guidance of light inside the fibre. The refractive index was 1.453 for the core and 1.405 for the cladding.[Kli99]

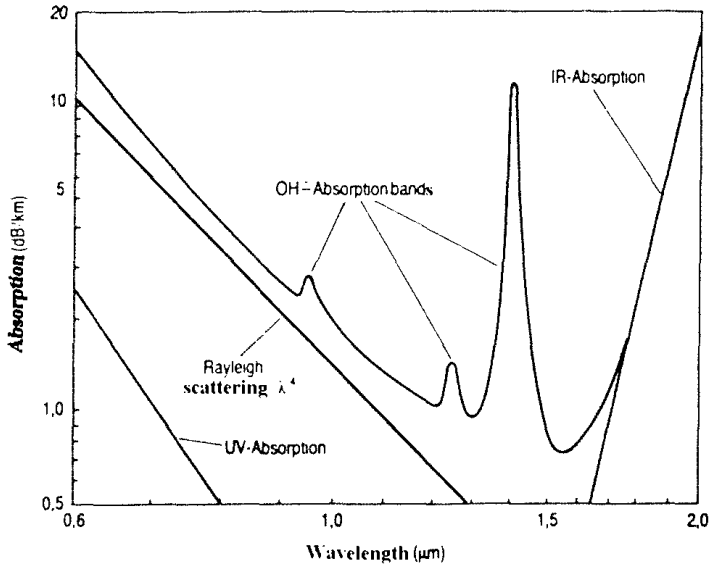

Fig. 7.7: Attenuation spectrum of typical fused silica bare fibre.[Sch90]

The minimization of intrinsic absorption in the ultraviolet (UV) and visible (VIS) spectral range, which is dominated by *Rayleigh scattering* and strongly depends on the

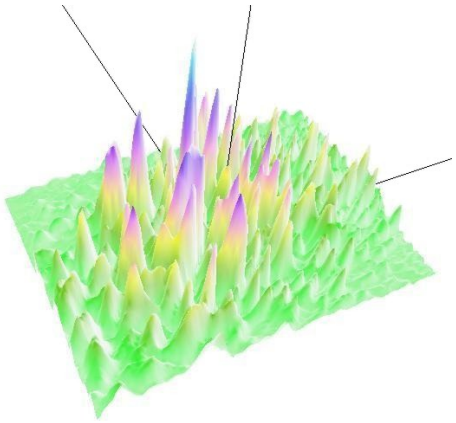

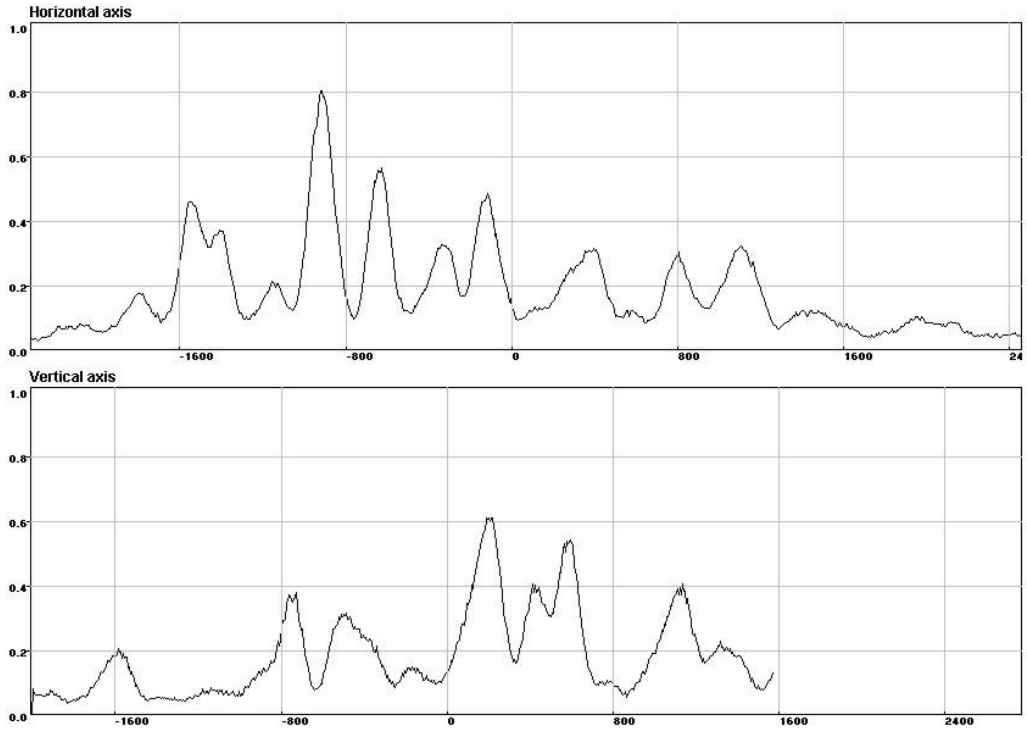

Fig. 7.8: Left: 3-D colour-coded beam analyser shot of intensity distribution of multi-mode bare fibre. Bottom: corresponding linear absorption spectrum.

wavelength, decreasing by the fourth power (see fig. 7.7) is important for the development of optical fibres .
Strong absorption bands of oxygen molecules are a major limitation for applications in the infrared (IR). Additional attenuation is caused by soiling especially due to hydroxyl ions with absorption peaks at 2.7 μm, 1.4 μm and 0.95 μm respectively.

The losses due to absorption are usually given by

$$\alpha = \frac{10}{l} log(\frac{P_0}{P}) \qquad [dB/km] \tag{7.4}$$

with l being the length of the fibre in kilometres. P_0 and P represent the incident laser power at $z = 0$ and the output power at $z = l$ respectively.

The fibre used during the experiments was a HCS© low OH^- step index bare fibre with an attenuation coefficient of 14 bB/km at 940 nm, and 12 dB/km at 1064 nm.

The left-hand image in fig. 7.8 shows a 3-D colour-coded intensity distribution recorded from a beam analyser. In contrast to single-mode fibres with Gaussian intensity distribution, here peak intensity is spread over the cross-section of the fibre. The plot in fig. 7.8 shows the corresponding intensity distribution along the x and y axis. Together with the high divergence of the fibre, a uniform irradiation of small tissue volumes with high intensities is possible. Since the majority of OO do not exceed 1.5 cm in diameter, LITT using bare fibres is a feasible treatment method. This allows for a much more simple laser application compared with LITT fibres with a diffusor tip, which are more fragile and often need external water cooling. Even at a maximum laser power of 12 watts, the bare fibre did not show any damage.
The deposition of debris or charred tissue fragments on the fibre tip, however, may lead to massive damage. In some cases, the distal tip may heat up so much that the fibre melts and the plastic cladding catches fire. This can be avoided using protection systems like the Lightguide Protection System (LPS) of the *MEDILAS D* diode laser that turns the laser off automatically if the distal end of the fibre is soiled with debris and white light is reflected back due to carbonization.

7.3 Bone coagulation with the Ho:YAG laser

Laser coagulation of cortical bone tissue was performed on pig thigh bones. Three different laser systems were compared with regard to thermal damage to collateral structures and the maximum size of tissue necrosis. All laser systems emit radiation in the infrared at wavelengths of 940 nm, 1064 nm and 2120 nm respectively.
The first laser evaluated for bone coagulation was the Ho:YAG laser ($\lambda = 2120$ nm), which was also used for laser hemiepiphysiodesis (see chapter 5). The *Medilas H* laser system is designed for clinical use with a compact mobile housing and closed cooling system.

7.3.1 Experimental set-up

Fig. 7.9 shows the set-up for the experiments with the Ho:YAG laser. For in vitro investigation, sheep thigh bones were cut in half with an anatomic saw and holes were drilled at distances of 5 mm for the fixation of both the laser fibre (600 μm bare fibre, see below) and the fluoroptic fibres.

The laser fibre was inserted into the first hole 3 to 4 mm inside the cortical bone. Fibre-optic probes were fixed in subsequent holes at distances of 5 mm, 10 mm and 15 mm. Laser energy was then applied for a period of 60 seconds and temperature distribution was recorded using a fluoroptic fibre thermometer. After each session, the distal end of the laser fibre was examined for any damage and new placement of the fibre and the temperature probes was repeated for the following measurements.

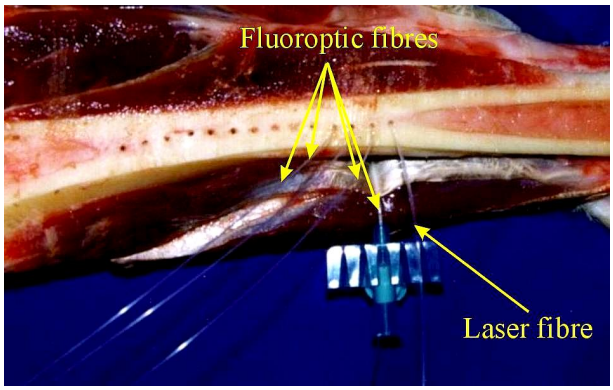

Fig. 7.9: Set-up for the bone coagulation experiments with the Ho:YAG laser. A 600 μm bare fibre was used for light transmittance.

Pulse energy	Repetition rate	Total energy	Distance from fibre	Maximum temp.
500 mJ	10 Hz	300 J	5 mm	65°C
1500 mJ	5 Hz	450 J	5 mm	> 80°C
1000 mJ	10 Hz	600 J	5 mm	60°C
1500 mJ	10 Hz	900 J	5 mm	> 80°C
1500 mJ	10 Hz	900 J	10 mm	50°C

Table 7.1: Comparison of the size of bone necrosis depending on applied laser energy after coagulation with the Ho:YAG laser.

Starting with a pulse energy of 500 mJ at a repetition rate of 10 Hz, pulse energy was increased in steps of 500 mJ up to a maximum energy of 1500 mJ. To evaluate the influence of the repetition rate, the treatment was also repeated with the same pulse energies at a repetition rate of 5 Hz.

7.3.2 Temperature control

An analysis of the temperature development during laser coagulation on trabecular bone is shown in fig. 7.10. The total energy applied was 300 J at pulse energies of 1000 mJ at a repetition rate of 5 Hz. Due to its higher water content, thermal diffusivity is much higher in trabecular bone and, thus, heat can be carried away more easily. The temperature reached more than 80°C at a distance of 5 mm from the fibre tip, whereas in cortical bone (see fig. 7.11), the temperature reached only 70°C. These differences may be even stronger in vivo, since the vascularization of trabecular bone is much stronger than that of cortical bone.

It can be seen in fig. 7.10 that even at a maximum pulse energy of 1500 mJ, the temperature does not exceed 70°C within a region of approximately 1 cm in diameter. Lower repetition rates of 5 Hz showed only minor difference (see table 7.1).

Table 7.1 gives an overview of the temperatures reached inside the cortical bone.

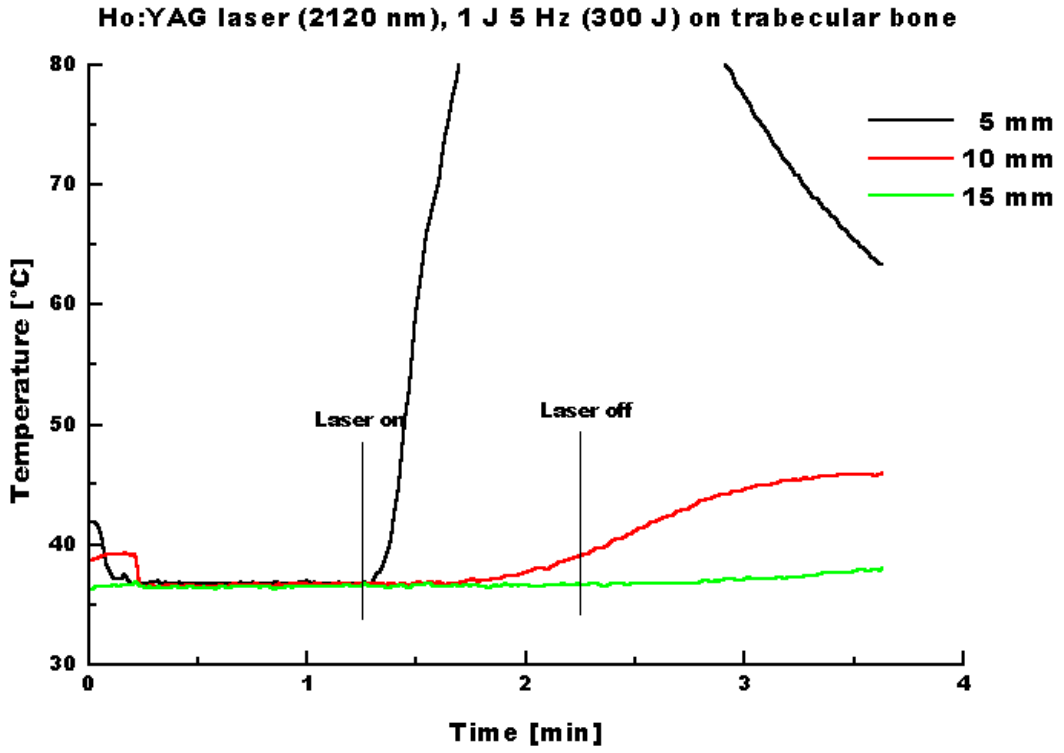

Fig. 7.10: temperature during laser coagulation of cortical bone with the Ho:YAG laser. The pulse energy was set at 1000 mJ at a repetition rate of 5 Hz. The laser was switched off after 60 seconds leading to a total application of 300 J.

7.3.3 Histological investigation

After laser coagulation, the tissue sample was prepared for histological investigation using cryomicrotome cuts as shown in fig. 7.12. We noticed that coagulation of bone tissue is accompanied by strong carbonization even at lower pulse energies. This is due to the high pulse energy of the Ho:YAG laser and the physical properties of cortical bone (see section 4.3). Laser pulses deposit a vast amount of energy within a small tissue volume (thermal penetration depth $\approx 250\ \mu m$), which is converted into heat through vibrational and rotational energy states of the water molecules. This leads to a sudden vaporization of water inside the tissue resulting in micro-explosions that also eject tissue fragments with high kinetic energy, thus, carrying away a vast amount of the pulse energy. In this case, however, ablation products could not escape, thus, most of the energy was kept within a small volume.

After all of the water within the focal volume has evaporated, subsequent pulses lead to a rapid heating up of the tissue. These high temperatures lead to a charring of the tissue surface within a zone of $\approx 50\ \mu m$ [Sch92], which results in even stronger light absorption and, thus, increases the heating up of the tissue. The temperature within the

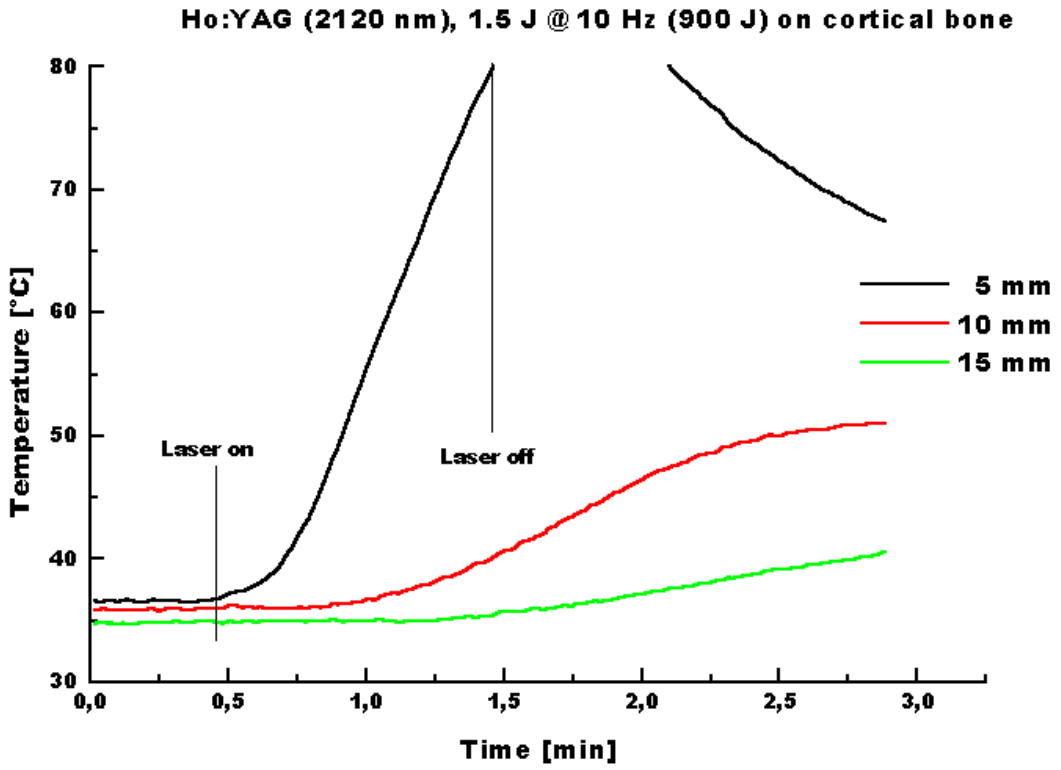

Fig. 7.11: Temperature during laser coagulation of trabecular bone with the Ho:YAG laser. Pulse energy was set to 1500 mJ at a repetition rate of 10 Hz. The laser has been switched off after 60 seconds leading to a total application of 900 J.

thermal volume may rise up to several thousand °C within a few microseconds, thereby igniting a thermal plasma [Hel92], [Kuh98]. This leads to a change in the structure of bone mineral which results in cracks inside the cortical bone (see arrows in fig. 7.12). This is accompanied by a typical noise and intense fluorescent light. Coagulation is limited to a region of approximately 1 cm in diameter as can be seen in fig. 7.12.

7.4 Bone coagulation with the Nd:YAG laser

The second laser which was evaluated was a powerful Nd:YAG laser system ($\lambda = 1064$ nm) constructed for laboratory use. The laser consists of a sealed cavity with a diode pumped crystal mounted in an open housing, which allows for easy adjustment and tuning of the mirrors. The system runs in the cw mode with a maximum output power of 28 W and a TEM_{00} beam.

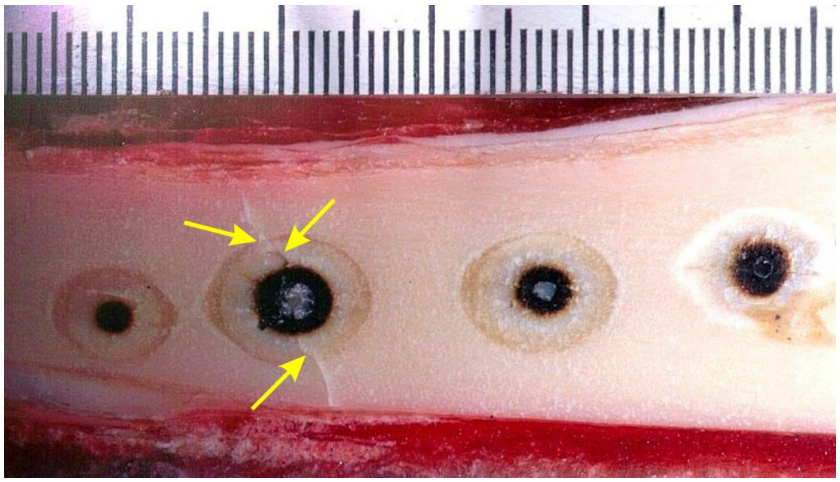

Fig. 7.12: Cryomicrotome cut after coagulation with Ho:YAG laser. The laser parameters were set to (from left to right): 500 mJ at 10 Hz, 1500 mJ at 10 Hz, 1000 mJ at 10 Hz and 1000 mJ at 5 Hz. The arrows show cracks due to melting and re-crytallization of bone matrix.

7.4.1 Experimental set-up

The laser was mounted on an optical board to provide easy connection to other components. With the use of a bending mirror, the laser beam was guided onto a spherical lens (f = 30 mm) focussing the beam into the optical fibre.
In contrast with the experiments with the Ho:YAG laser, the temperature probes in this experiment were located along the bone axis and perpendicular to it, i.e. in the lateral direction. Fig. 7.13 shows the arrangement of the laser fibre and the fluoroptic fibres for the experiments with the Nd:YAG laser on cortical bone.

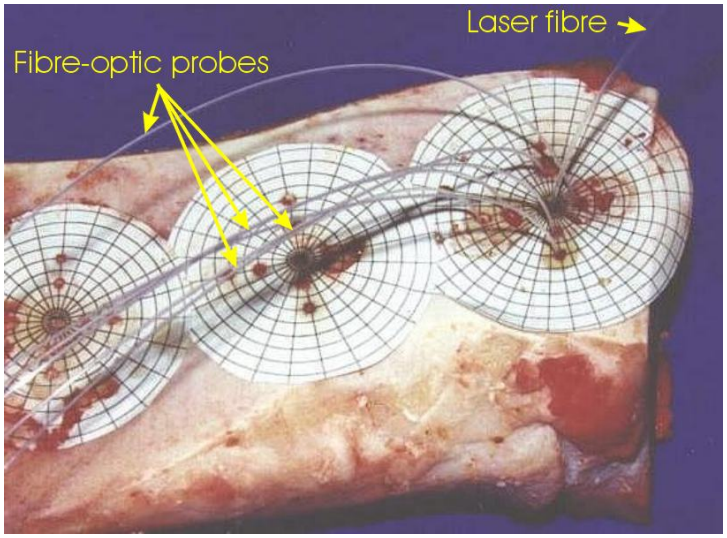

Fig. 7.13: Positioning of the optical fibre inside the cortical bone. A spherical template was used for precise positioning.

The laser fibre was fixed in the centre and fibre-optic probes were fixed at radial distances of 4 mm, 6 mm, 8 mm and 10 mm from the centre. Laser radiation was then applied for 180 seconds. As in the experiments with the Ho:YAG laser, the fibre was

examined after each session to check the distal surface.
In total, five measurements were carried out with total energies applied ranging from 360 J to 2000 J (see table 7.2). During the experiment, the tissue sample was placed inside a saline solution to simulate the cooling of surrounding tissue similar to in vivo conditions. The solution was heated externally and kept at a temperature of 37°C.

7.4.2 Temperature control

An analysis of temperature development during laser coagulation with the Nd:YAG laser is shown in fig. 7.14, and fig. 7.15.

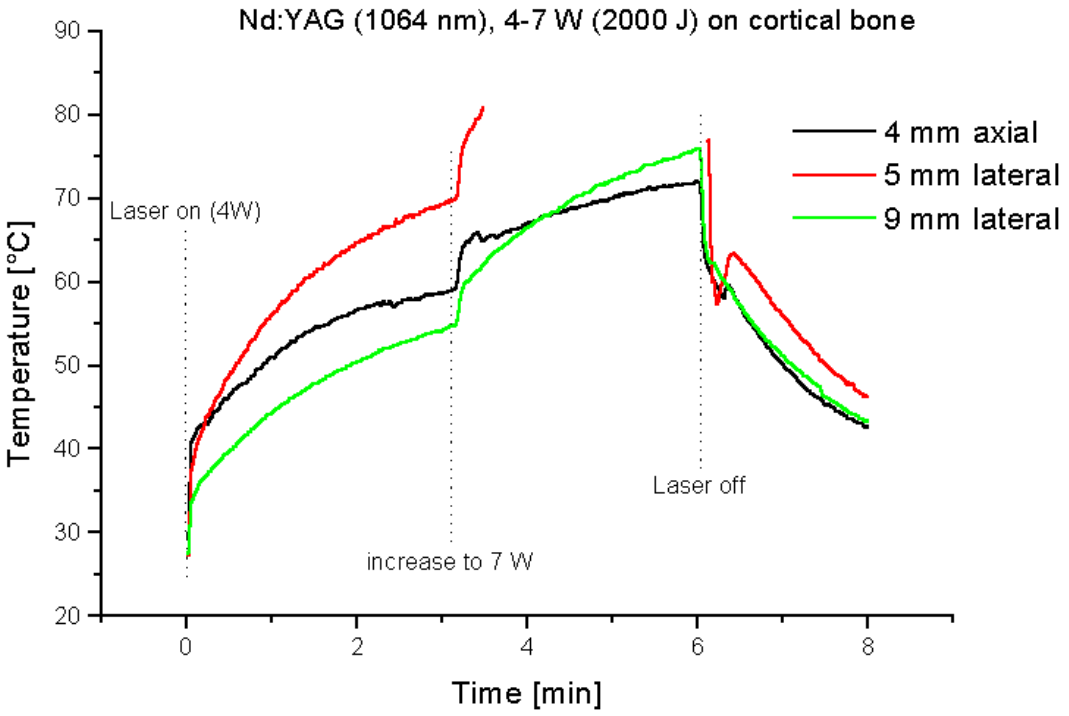

Fig. 7.14: Temperature during laser coagulation of cortical bone with the Nd:YAG laser. Laser power was set at 4 W and then increased to 7 W with a total energy application of 2000 J.

In fig. 7.14, initial laser power was set at 4 W and then, after 180, was increased to 7 W for another 180 seconds which led to a total energy application of 2000 J. An interesting result from temperature measurement is the difference in temperatures along the bone axis compared to those in the lateral direction. Fig. 7.14 shows that the rise in temperature in the lateral direction was twice as high as in the axial direction. This is due to the structure of cortical bone with its concentric lamellae in each osteon which contain collagen fibres oriented at a perpendicular angle to one another (see fig. 4.1). This structure leads to a preferential diffusion of temperature along the bone axis. Temperature measurement

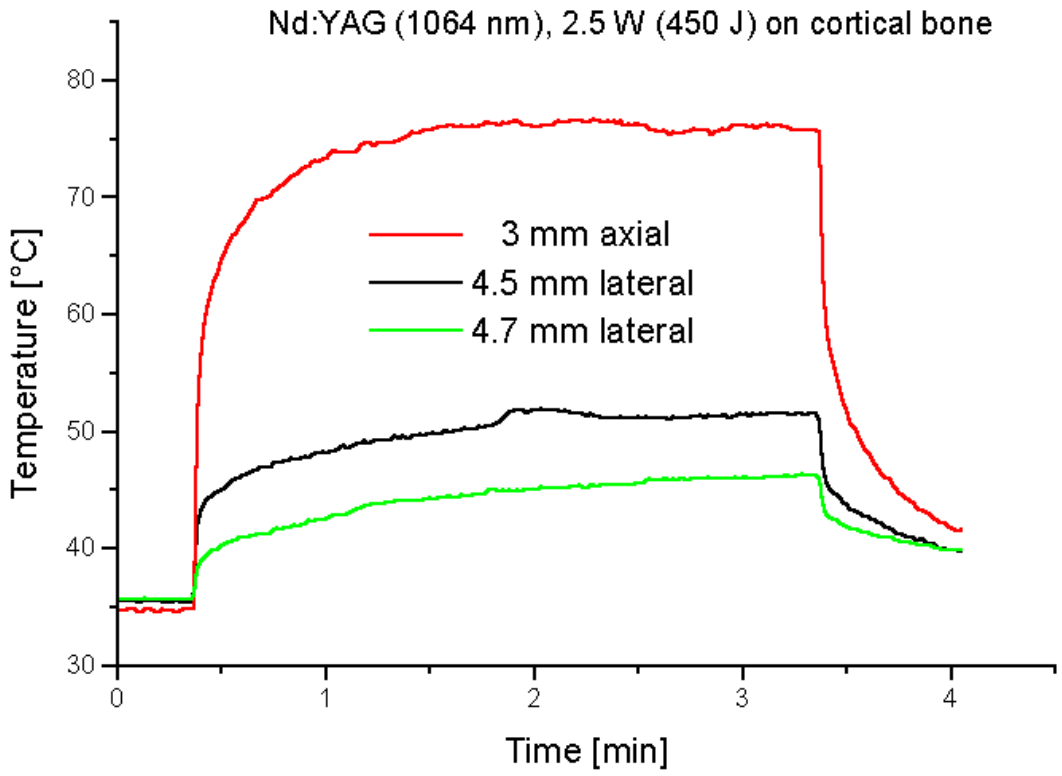

Fig. 7.15: Temperature during laser coagulation of cortical bone with the Nd:YAG laser. Laser power was 2.5 W with a total energy application of 450 J.

with the fluoroptic thermometer, however, is limited to a maximum temperature of 80°C, thus, the maximum values cannot be determined exactly.

Table 7.2 shows that an application of 360 J from the Nd:YAG laser is capable of heating up bone cells to more than 50°C within a distance of 5.5 mm from the laser fibre. At total energies of 2000 J, the size of tissue coagulation reaches more than 9 mm, thus, tumour sizes of up to 2 cm may be treated.

7.4.3 Histological investigation

Histological investigation of the tissue sample after irradiation with the Nd:YAG laser showed that there was only minimal charring (see fig. 7.16) even after application of 2000 J.

These results implied that the Nd:YAG laser is superior to the Ho:YAG laser with regard to LITT of bone tissue, since carbonization did not occur. This allows for deeper and faster penetration of laser radiation into the tissue resulting in larger coagulation volumes.

Total energy	Laser power	Distance from fibre	Maximum temperature
360 J	2 W	3.5 mm (lateral)	63°C
360 J	2 W	5.5 mm (lateral)	54°C
400 J	2.25 W	5 mm (lateral)	64°C
450 J	2.5 W	3 mm (axial)	76°C
500 J	2.8 W	4.5 mm (lateral)	58°C
2000 J	7 W (4 W)	4 mm(axial)	> 80°C
2000 J	7 W (4 W)	5 mm (lateral)	62 °C
2000 J	7 W (4 W)	9 mm (lateral)	62 °C

Table 7.2: Comparison of bone necrosis depending on applied laser energy.

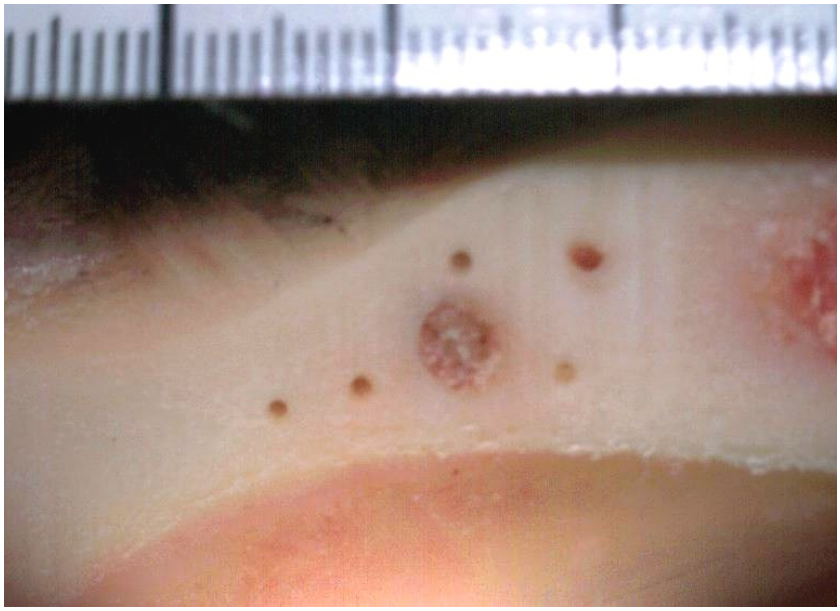

Fig. 7.16: Cryomicrotome cut after coagulation with Nd:YAG laser. Total energy applied was 2000 J.

7.5 Bone coagulation with the diode laser

The third laser system that was evaluated was a diode laser ($\lambda = 940$ nm) with a maximum output power of 50 W. The laser is a compact turnkey system for clinical applications. Due to its wavelength of 940 nm, laser tissue interaction is dominated by thermal interaction (see section 2.2).
In the standard mode, output power can be increased from 1 to 50 watts in steps of 1 watt. The laser is equipped with a special Lightguide Protecting System (LPS) which detects the white fluorescent light that occurs if tissue is carbonized and, thus, allows for easy protection against tissue carbonization. During the experiments, however, the LPS mode was switched off since the thermal properties of bone tissue required a minimal output power of 6 watts. This resulted in a small rim of charred tissue adjacent to the laser fibre.
As in the experiments with the Ho:YAG laser and the Nd:YAG laser, fibre-optic fluorescent temperature probes were fixed inside the cortical bone at distances of 3 to 10 millimetres

from the tip of the laser fibre. During the experiment the tissue sample was placed inside a saline solution to simulate the cooling of surrounding tissue similar to in vivo conditions. For laser coagulation, a maximum output power of 10 W was applied.

7.5.1 Temperature control

An analysis of temperature development during laser coagulation with the diode laser is shown in fig. 7.17.

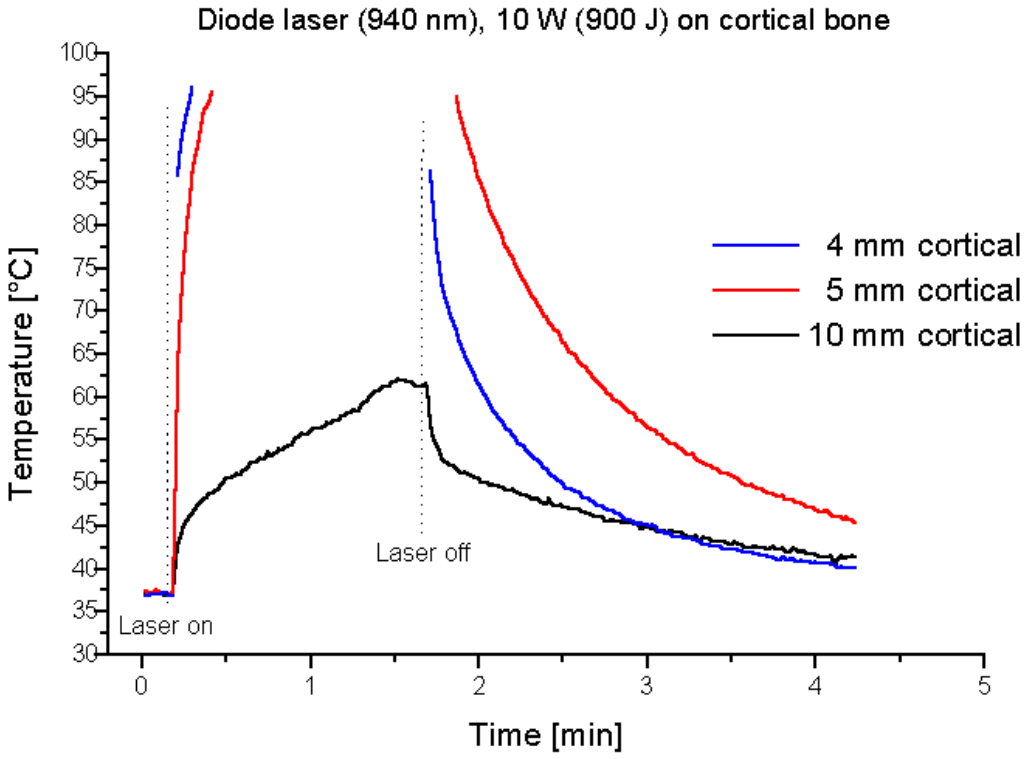

Fig. 7.17: Temperature during laser coagulation of cortical bone with the diode laser. Laser power was 10 W with a total energy application of 900 J.

LITT of bone tissue with the diode laser allows for maximum coagulation of tumour sizes up to 2 cm in diameter. This is comparable with the extent coagulation using the Nd:YAG laser. The total energy applied, however, was only half as much.

Similar to the results for the Nd:YAG laser, the diode laser allows for coagulation of tumour sizes up to 2 cm in diameter at total energies of less than 1000 J.

7.5.2 Histological investigation

Fig. 7.18 shows the cryomicrotome cut after irradiation of 900 J (10 W) with the diode laser. Charring was limited to a zone of two to three millimetres. Compared with the

Total energy	Laser power	Distance from fibre	Maximum temperature
380 J	7 W	5 mm	50 °C
500 J	5 W	5 mm	48 °C
720 J	12 W	8 mm	60 °C
900 J	10 W	10 mm	62 °C

Table 7.3: Comparison of bone necrosis depending on applied laser energy from diode laser.

results from previous investigations, charring was considered acceptable. In vivo investigations might result in a smaller amount of charring.

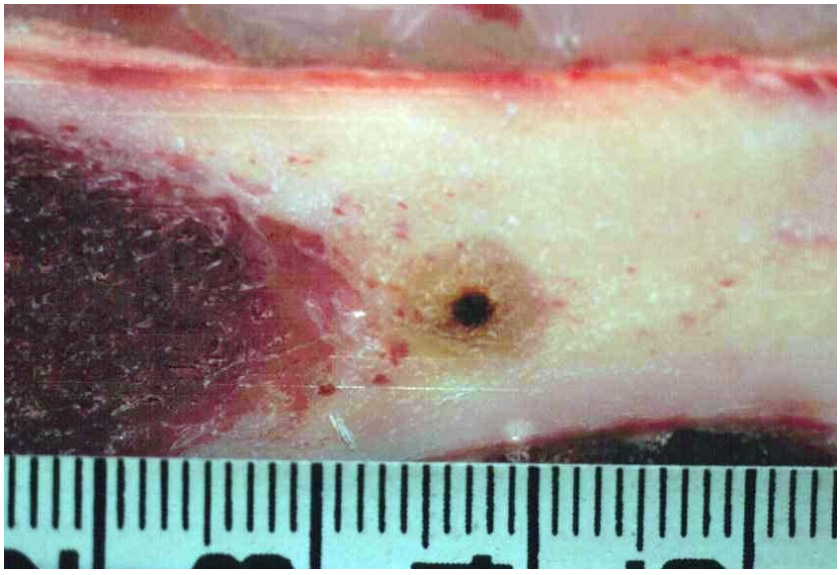

Fig. 7.18: Cryomicrotome cut after coagulation with diode laser. Total energy applied was 900 (10 W).

7.6 Online MRI temperature control of laser coagulation on bone tissue

One method of monitoring the efficiency of thermotherapy is to measure tissue temperature. Interstitial temperature monitoring conventionally requires the invasive placement of temperature probes. These probes provide only information about the temperature at discrete points. Thus, insufficient information about the continuous temperature distribution inside the tumour is provided. Precise information, however, is of great importance, since tumour cells can survive in "cold spots" and healthy tissue can be damaged in "hot spots".

The temperature dependence of several physical parameters that influence the MR image can be used as a for non-invasive method of temperature monitoring [Rei98] [Mül98] [Mor98] [Ols98] [Pal97] [Asc93] [Blü93]. Three different approaches for MR thermometry are currently available. The temperature dependence of the spin-lattice relaxation time T_1, the temperature dependence of the proton resonance frequency (PRF or chemical

shift) and the temperature dependence of the diffusion coefficient D (see section 3.3). All three methods were investigated to determine their feasibility during laser coagulation of bone tissue.
Following the evaluation of the three laser systems, the Ho:YAG laser turned out to be unsuitable for laser bone coagulation due to intense charring of the tissue. The Nd:YAG laser is not a turnkey system and needs special installations for power supply and water cooling, which were not available at the MRI scanner. Thus, only the diode laser could be tested under online MRI temperature control.

7.6.1 Experimental set-up

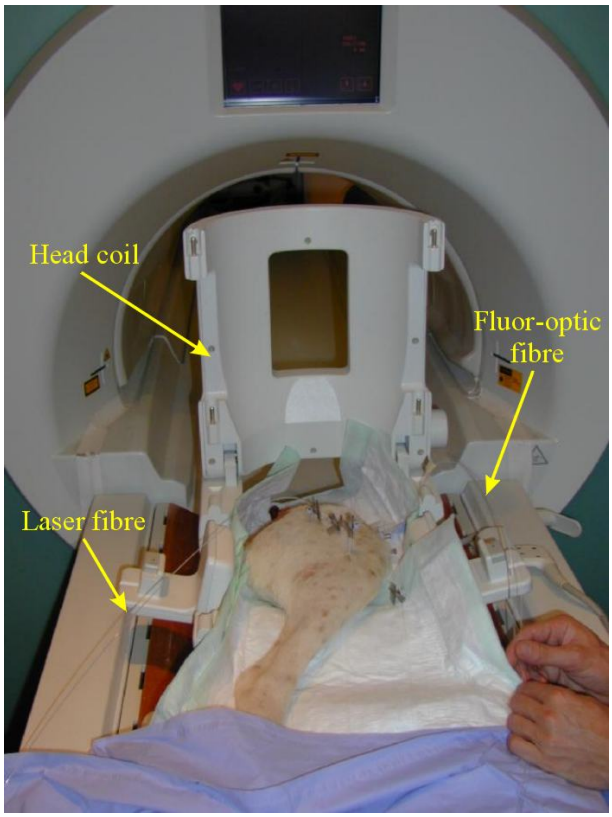

Fig. 7.19: Set-up of the experiments regarding laser coagulation under online MRI temperature control using a 1.5 Tesla scanner and a head coil for signal acquisition. To protect the laser fibre and the fluor-optic fibres from breakage they were fixed inside a venous catheter.

All experiments were carried out on a 1.5 Tesla super-conducting whole body scanner (Magnetom Vision, Siemens AG, Germany) at the German Cancer Research Centre. A standard circular polarized head coil was used for signal detection. The invasive temperature data were acquired using a 4-channel fibre-optic fluorescent thermometer (Model 755, Luxtron, USA). Fig. 7.19 shows the experimental set-up.
Before laser coagulation was started, anatomical scans were acquired to locate the artificial tumour and to match the region of interest (ROI) in the corresponding planes. To determine changes due to laser coagulation in the anatomical scans, data acquisition was repeated after laser coagulation. Fig. 7.20 shows two T_1 weighted scans before (left) and after (right) laser coagulation with 600 J (120 seconds).

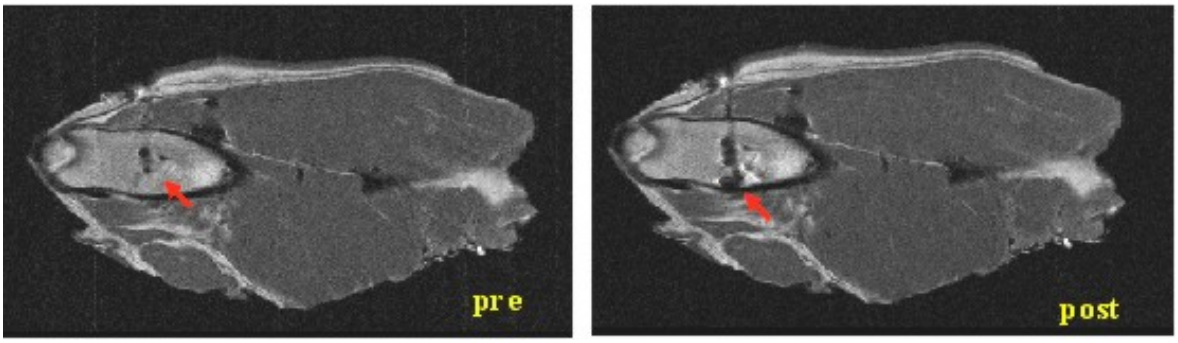

Fig. 7.20: Coronal T_1 weighted MRI before (left) and after (right) laser coagulation with 600 J (120 s). After application of contrast medium the laser lesion in the bone marrow appeared as a hypo-intense region (arrow).

7.6.2 Temperature control using the PRF-method

Phase images were acquired using a conventional FLASH sequence without phase correction. Parameters were set to: TR = 50 ms, TE = 15 ms, flip angle = 30°, MA = 256 × 256. This resulted in a total acquisition time of 15 seconds and a nominal resolution of 0.98 × 0.98 mm^2.

Fig. 7.21 shows first results from PRF temperature monitoring. Total energy applied was 300 J.

The colour-coded phase images were calculated using a 3 × 3 pixel filter and by subtracting the initial grey-scale image acquired immediately before laser coagulation, from all subsequent images acquired during laser action. The update time throughout the experiment was limited to 15 seconds due to the long acquisition time of the MRI sequence. Invasive temperature monitoring was performed using fibre-optic probes located in the cortical bone at a distance of 3-4 mm and in the adjacent muscle simultaneously to the PRF temperature measurements.

7.6.3 Temperature control using the T_1 relaxation time

SRTF images (see section 3.3.1) were acquired for T_1 relaxation temperature control using the following parameters: TR = 10.2 ms, TE = 4 ms, T_{REC} = 1100 ms, flip angle = 12°, MA = 128 × 128, with a total acquisition time of 1.5 seconds. The spatial resolution was 1.95 × 1.95 mm^2. Fig. 7.22 shows the results from rapid MRI temperature imaging during laser coagulation using the T_1 method.

The colour-coded images in fig. 7.22 show that the temperature adjacent to the laser fibre exceeded 100°C. This concurred with the fibre-optic measurements, where the maximum temperature reached 130°C. Fig. 7.23 shows the results of rapid MR temperature monitoring after application of 1080 J. The colour-coded images were calculated using calibration on fat tissue and were then superimposed on the anatomical image using a 3 × 3 pixel filter. There is, however, a problem in calibrating temperatures exceeding 65°C,

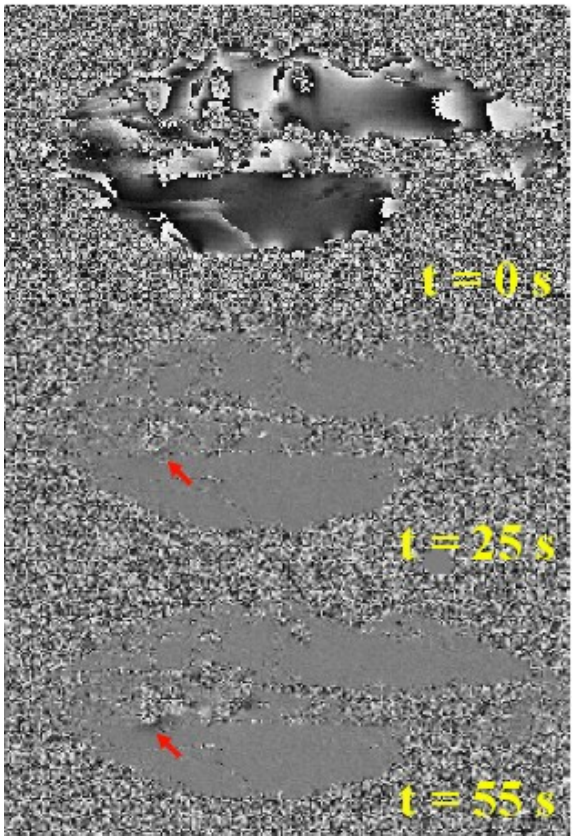

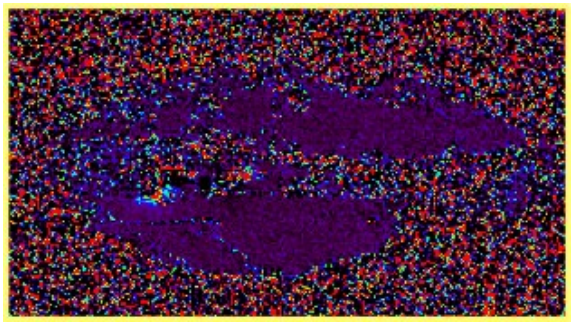

Fig. 7.21: Left: phase image before (top), after 25 seconds (middle) and after 55 seconds (bottom) of laser coagulation. Right: colour-coded image after application of 300 J without superimposition of the anatomical image and without filtering.

since temperature changes no longer correlate linearly to changes in T_1 relaxation time.

As the right-hand plot in fig. 7.23 shows, temperature falls rapidly in the lateral direction. This concurs with the data from fibre-optic measurements.

7.6.4 Temperature control using the diffusion method

Single shot (HASTE) spin-echo sequences with asymmetric timing table (SLICE-technique) and Stejskal-Tanner preparation were used for diffusion weighted images [Rad00]. The parameter settings were: TR = 5000 ms, TE = 116 ms, b-value up to 400 s/mm^2 with G_{max} = 18.5 mT/m, MA = 128 × 128, with a total acquisition time of 1 second and a nominal resolution of 1.88 × 0.94 mm^2.

Fig. 7.24 shows the results of the temperature measurements using diffusion weighted MRI. The colour-coded image shows only minor changes in temperature. Due to the long TE which is limited by system paramters and due to the short T_2 relaxation time the MR signal is very small, thus, image quality is not as good as for T_1 weighted images with shorter TE.
Since none of the images showed great changes, it is thought that the diode laser might not have worked properly. Simultaneous invasive temperature measurements with fibre-optic probes produced similar results.

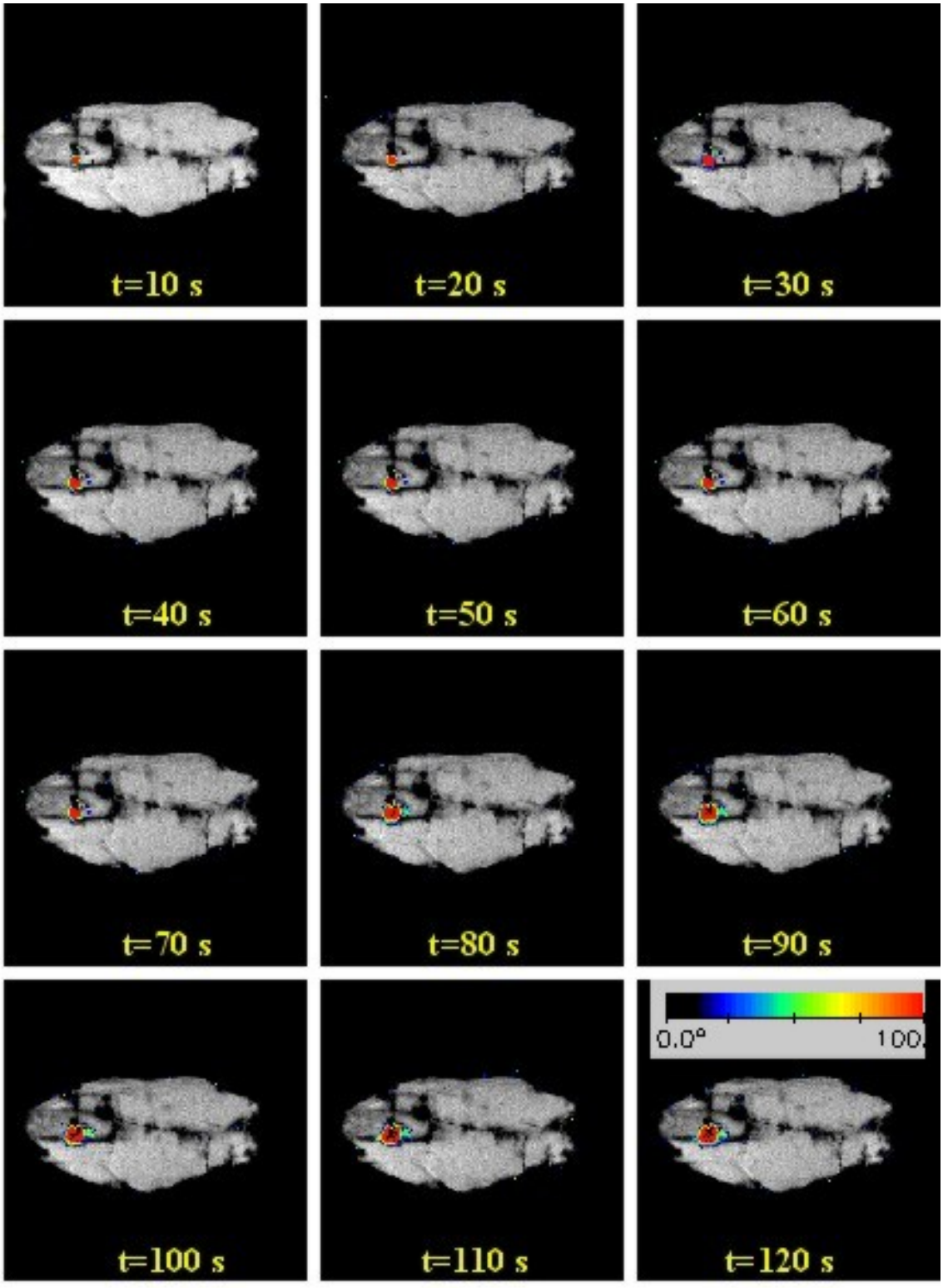

Fig. 7.22: Chronological temperature control during laser coagulation using T_1 weighted MRI. Total energy application was 960 J (120 seconds). Image acquisition was carried out every 10 seconds. Colour-coded images were calibrated on T_1 relaxation time of fat (Δ T_1 = 3 ms/°C).

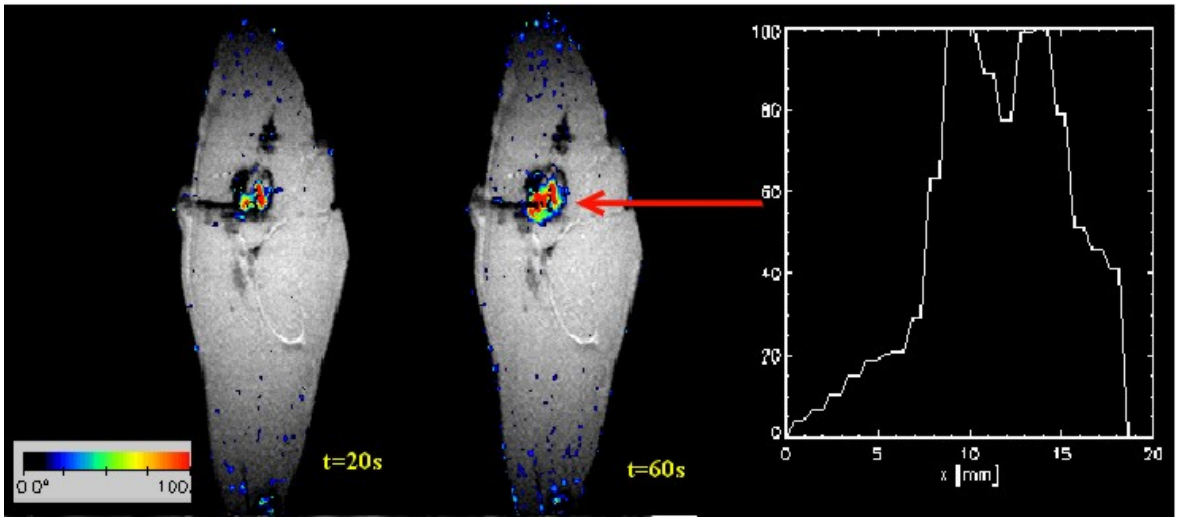

Fig. 7.23: Comparison of colour-coded temperature images with corresponding temperature plot calibrated on fat (Δ T_1 = 3 ms/°C).

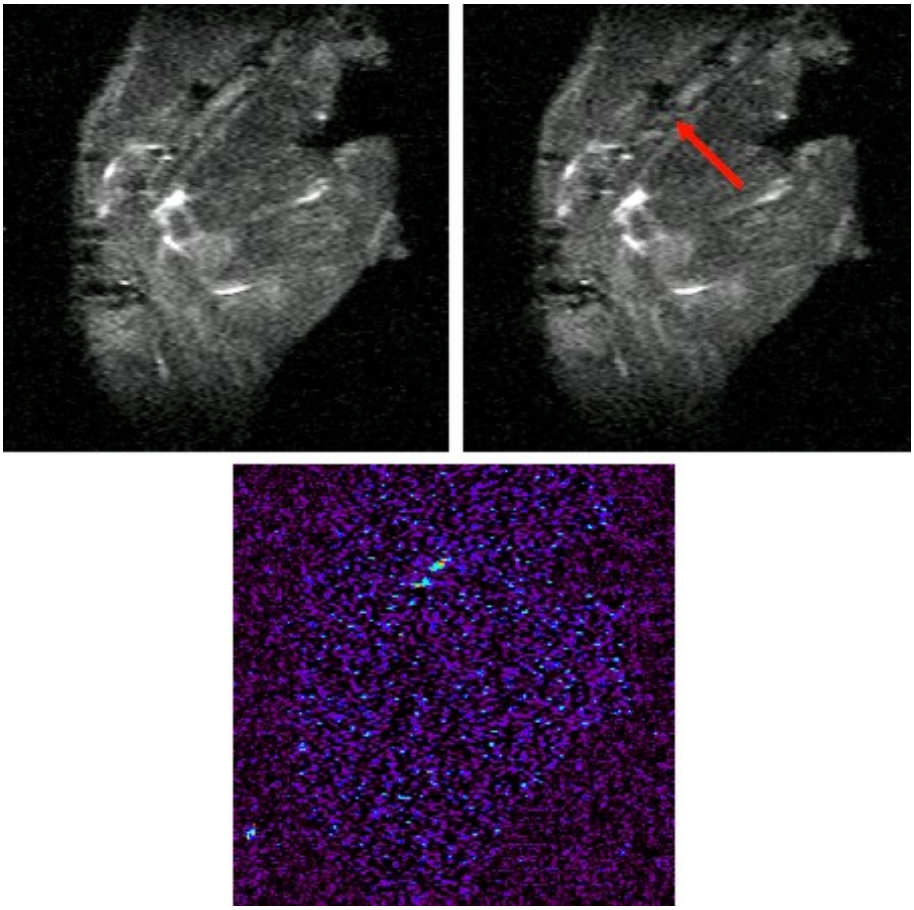

Fig. 7.24: Top: diffusion weighted MR image before (left) and after (right) laser coagulation with 100 J (10 seconds). Bottom: colour-coded image after application of 100 J (without superimposition of anatomical image).

7.7 Conclusion

We have demonstrated LITT on non-perfused bone tissue to be a promising, simple, precise and minimally-invasive treatment for osteoid osteoma and an alternative to existing surgical and percutaneous operation techniques.
After evaluating three different laser systems (Ho:YAG, Nd:YAG and diode), we found that thermal penetration and thus coagulation of bone tumours is possible even for tumours of up to 2 cm in diameter. The **Nd:YAG laser** (λ = 1064 nm) provided the best results with regard to **fast coagulation** and **little charring**. However, blood flow during in vivo experiments together with the Lightguide Protection System (LPS) means that charring can be minimized [Whe95]. Thus, the diode laser cab be regarded as the most appropriate laser for future in vivo investigations.

Temperature measurements during laser coagulation of cortical bone tissue using the Ho:YAG laser showed that, due to its high pulse energies of up to 1800 mJ, strong carbonization occurred. In addition, due to high temperatures, bone mineral melted and re-crystallization led to a cracking of the bone. Due to its strong carbonization and limited coagulation of approximately 1.2 cm in diameter, the Ho:YAG laser is considered to be unsuitable for laser coagulation of cortical bone.

Throughout the experiments, the bare fibre proved to be efficient, which meant that the use of LITT fibres with diffusor tips was not necessary due to the small size of the osteoid osteoma. These fibres are much more fragile and often additional cooling of the fibre is needed. LITT fibres, however, would be needed for the coagulation of larger bone tumours such as ostoe-blastoma or bone metastasis.
Our new puncture system was developed and tested for the puncture of the nidus and proved to be perfect with regard to accuracy, stability and compatibility, showing no artefacts during MRI. We also compared conventional MRI puncture needles made for application on bone tissue.
We developed new fast MRI sequences for online temperature monitoring together with the German Cancer Research Centre. Measurements showed that the T_1 method is the most reliable one at the moment, although the results from the diffusion method and the PRF (proton resonance frequency) are more sensitive. A precise estimation of absolute temperature for phase and diffusion images, however, requires further investigation. First results demonstrate that visualization and control of the heating procedure during LITT on bone tissue based on MR thermometry is possible. Data acquisition within a few seconds allows for rapid temperature monitoring. Time resolutions are 1 s for diffusion weighted images, 1.5 s for the T_1 weighted images and 15 s for the PRF method. Spatial resolutions are 0.98×0.98 mm^2 for PRF, 1.88×0.94 mm^2 for diffusion and 1.95×1.95 mm^2 for T_1 weighted images [Rad01].

Chapter 8

Conclusion and Outlook

After an evaluation of four different laser systems during extensive in vivo studies on lamb's spines, the Ho:YAG laser turned out to be the most appropriate laser system for in vivo studies using the new minimally-invasive operation technique for a gentle treatment of spinal deformities. A special laser applicator suitable for sterilization and endoscopic usage was developed for this purpose.
In contrast to the results of the in vitro experiments, the temperature fell rapidly to a value close to body temperature immediately after the laser had been switched off, whereas during the in vitro experiments the temperature remained at a relatively high level due to the lack of blood flow. Although the peak temperature reached 75°C in the vertebral body during in vivo treatment, it fell very quickly so that no lasting effects to the nerve roots in the vertebral bodies and the spinal cord are to be expected. None of the animals showed any neurological conspicuousness.
These first results imply, that it is possible to produce a **change in spinal growth by laser hemiepiphysiodesis**. Nevertheless, in order to develop this operation technique for clinical application it is necessary to determine a tight correlation between the number of ablated growth plates and the extent of scoliotic growth, thus, further investigations are necessary.
In 75% of all cases, the desired effect of inhibiting growth on one side, i.e. the side with laser hemiepiphysiodesis, could be achieved. However, the degree of curvature did not exceed 30° and might not be sufficient to compensate severe scoliotic growth of up to 70°. Thus, from a clinical point of view, the ablation of a maximum number of six epiphyseal growth plates might not have been enough to induce significant scoliotic growth and might be a reason why the change in spinal growth is not as strong as might be needed for an effective treatment of severe idiopathic scoliosis. In addition, the neurocentral cartilage in the vertebral bodies of foxhounds might have had a negative influence on scoliotic growth. However, for minor scoliotic growth, the invented technique would be sufficiently successful.
Animal experiments with primates might have been more successful due to their similarity to the human with an upright position of the spine. These experiments, however, would be extremely costly and difficult to carry out for ethical reasons. However, according to the given objective of partially removing the vertebral growth

plate as a minimally-invasive scoliosis treatment, it was shown that high-precision, minimal thermal damage to adjacent tissue and a sufficiently high ablation rate could be achieved during in vivo operations. The chosen 3-D thoracoscopic operation technique in combination with the Ho:YAG laser proved to be successful and reliable with regard to laser tissue ablation, laser handling and the safety of sensitive structures. In addition, the results of this work can be used to apply the operation technique to other, similar clinical applications where a precise ablation of hard tissue without thermal damage to adjacent structures is essential, such as the treatment of herniated discs and stenosis of intervertebral foraminae.
Alternative laser ablation might be possible in the future due to newly developed sapphire optical fibres with high transmission rates of more than 80% at wavelengths of up to 3.5 microns. This would allow the endoscopic use of Erbium doped lasers at wavelengths of around 3 μm at which water has its strongest absorption peak. These fibres were, however, not available when we carried out our work.

In a second application, the experiments with the ps and fs-laser system showed that plasma-mediated tissue ablation of cortical bone is possible with sufficiently high ablation rates and accuracy for the clinical application of microsurgical treatment. In addition, according to the results from histological investigations, no thermal damage occurred to collateral structures. Compared to a zone of thermal damage of 50-100 μm for bone ablation with the Ho:YAG laser [Sch92][Cha90] and 100-200 μm for the CO_2 laser [Sch92][Fri00], plasma-mediated bone ablation is very safe, thus, the use of new compact ps and fs-lasers in combination with already existing laser-probes [Göt99] enables the non-thermal ablation of bone tissue and, therefore, makes new clinical applications possible, especially in orthopaedics in the treatment of stenosis on vertebral foraminae, necrosis of the head of femur [Bon99] and ear-nose-throat (ENT) surgery. Since threshold fluence needed for initiating the ablation process is lower for the shorter femtosecond pulses than for picosecond pulses, lower pulse energies can be used for the removal of bone tissue if femtosecond laser pulses are applied. This results in reduced shockwave effects. In addition, in comparison to longer picosecond laser pulses from the Nd:YAG laser, the ablation with the Ti:Sapphire femtosecond pulses was found to be more efficient. However, due to its high pulse energy of up to 2.5 mJ and repetition rates of up to 4 kHz, the picosecond laser system may reach high ablation rates of cortical bone tissue of about 10 mm^3/min. This time is short enough to be of clinical relevance. For these laser parameters, the ablating beam should be scanned over the tissue surface ten times faster than in this experiment. From a technical point of view, such scanning speeds can be easily achieved.

In a third application, we demonstrated the feasibility of LITT on bone tissue as a promising, simple, precise and minimally-invasive treatment for Osteoid Osteoma that may be an alternative to traditional surgical and percutaneous ablations.
After evaluating three lasers (Ho:YAG, Nd:YAG and diode (λ = 940 nm)), we found that thermal penetration and, thus, coagulation of the bone tumour is possible even with

tumour sizes of up to 2 cm in diameter. The **Nd:YAG laser** provided the best results with regard to **fast coagulation** and **little charring**. However, due to blood flow during in vivo experiments together with the Lightguide Protection System (LPS), charring can be minimised. Thus, the diode laser was regarded being the most appropriate laser for future in vivo investigations.

Due to its strong carbonisation and limited coagulation of approximately 1.2 cm in diameter, the Ho:YAG laser is considered being unsuitable for laser coagulation of cortical bone.

Throughout the experiments, the bare fibre proved to be sufficient due to the small size and round shape of the Osteoid Osteoma. Thus, no LITT fibres with diffusor tip and additional cooling were necessary. This, of course, is not applicable to larger bone tumours such as ostoeblastoma or bone metastasis. Those tumours were not part of this investigation.

Our new puncture system was developed and tested for the puncture of the nidus and proved to be perfect with regard to accuracy, stability and compatibility, showing no artefacts during MRI acquisition. We also compared conventional MRI puncture needles made for an application on bone tissue to our own newly invented puncture needle. It turned out that the conventional needle becomes blunt, i.e. useless, after one single puncture whereas our needle proved to be far more rigid and could be used for at least 10 punctures.

We developed new fast MRI sequences for online temperature monitoring together with the German Cancer Research Centre. Measurements showed that the T_1 method is the most reliable one at the moment, although the results from the diffusion method and the PRF (proton resonance frequency) are more sensitive. This, of course, puts high demands on the MRI scanner too. A precise estimation of absolute temperature for phase and diffusion images requires further investigation. First results, however, demonstrate that visualization and control of the heating procedure during LITT and data acquisition within intervals of 1.5 seconds is possible.

Future investigation will have to verify the results during in vivo experiments. This will have to include verification of laser parameters, MRI temperature control, and histological investigation. We think that our operation technique will we ready for a first clinical use within the next two years.

References

[Abr61] A. Abragam, *Principles of Nuclear Magnetism*, Oxford University Press, 1961

[Ada88] G.Adam, O. Hittmar, *Wärmetheorie*, Vieweg, Braunschweig, 1988

[Alv77] A. Alves, J.A. Resina, *Techniques of correction and internal fixation for scoliosis*, Journal of Bone Joint Surgery, 59B:159, 1977

[Asc93] P.W. Ascher, M. Fan, O. Schröttner, F. Ebner, R. Kleinert, *Interstitielle laserassistierte Thermotherapie zentraler Hirntumore unter direkter Manget Resonanz Kontrolle*, in H.-P. Berlien, G.J. Müller *Angewandte Lasermedizin*, Ecomed, Landsberg/Lech, 1993

[Bac96] P. Bachert, L.R. Schad, M. Bock, M.V. Knopp, M. Ebert, T. Grossmann, W. Heil, D. Hofmann, R. Surkau, E.W. Otten, *Nuclear magnetic resonance imaging of airways in humans with use of hyperpolarized ^3He*, Magnetic Resonance in Medicine, 36(2):192-196, 1996

[Bad87] P. Bado, M. Bouvier, J.S. Coe, *Nd:YLF mode-locked oscillator and regenerative amplifier*, Optics Letters 12:319, 1987

[Ben93] A. Benninghoff, *Makroscopische Anatomie, Embryologie und Histologie des Menschen*, Urban und Schwarz, 1993

[Ben82] R. Bensasson, *La photochimiotherapie par l'hematoporphyrine. Introduction, mechanismes moleculaires*, Laser Medical, 1982

[Ber92] H.-P. Berlien, G.J. Müller, *Angewandte Lasermedizin*, Ecomed, Landsberg/Lech, 1992

[Ber98] F. Bertsch, J. Mattner, M.K. Stehling, U. Müller-Lisse, M. Peller, R. Loeffler, J. Weber, K.Messmer, W. Wilmanns, R. Issels, M. Reiser, *Non-invasive temperature mapping using MRI: Comparison of two methods based on chemical shift and T_1-relaxation*, Magnetic Resonance Imaging, 16:393-404, 1998

[Bih89] D. Le Bihan, J. Delannoy, R. L. Levin, *Temperature mapping with MR imaging of molecular diffusion: Application to hyperthermia*, Radiology, 171:853-857, 1989

[Bil97] J.F. Bille, S. Gölz, R. Kessler, I. Müller-Vogt, M.H. Götz, F.E. Kruse, A.M. Joussen, H.E. Völcker, *Comparative Investigation of Corneal Ablation by Different UV-Laser Sources at 193 nm and 211 nm*, in JERMOV Montpelier, 1997

[Bis40] J.D. Bisgard, M.M. Musselman, *Scoliosis; It' s Experimental Production and Growth Correction; Growth and Fusion of Vertebral Bodies*, Surg. Gynecol. Obset., 70:1029-1036, 1940

[Bit92] E. Bitrolf, *Flexible Endoscope*, in [Ber92], *Angewandte Lasermedizin*, Ecomed, Landsberg/Lech, 1992

[Blü93] S. Blüml, L.R. Schad, B. Stepanow, W.J. Lorenz, *Spin-Lattice Relaxation Time Measurement by Means of a TurboFLASH Technique*, Magnetic Resonance in Medicine, 30:289-295, 1993

[Blo46] F. Bloch, *Nuclear induction*, Physical Review 70:460-474, 1946

[Boc00] M. Bock, S.O. Schoenberg, F. Floemer, L. R. Schad, *Separation of Arteries and Veins in 3D MR Angiography using Correlation Analysis*, Magnetic Resonance in Medicine, 43:481-487, 2000

[Boh99] C. Bohris, *Temperaturmessung mit der Magnet-Resonanz-Tomographie zur Überwachung von medizinischen Thermotherapien mit Laser oder Ultraschall*, Dissertation, University of Heidelberg, 1999

[Bon99] B. Bonni*Laserablation von spongiösem Knochengewebe im Hinblick auf die Behandlung der Hüftkopfnekrose*, Diploma thesis, University of Heidelberg, 1999

[Bou86] J.-L. Boulois, *Photophysical Processes in Recent Medical Laser Developments: a Review*, Lasers in Medical Science Vol. 1, 1986

[Boy65] G.D. Boyd, A. Ashkin, J.M. Dziedzic, D.A. Kleinman, *Second-Harmonic Generation of Light with Double Refraction*, Phys. Rev. 137:1305, 1965

[Bro87] I.N. Bronstein, K.A. Semendjajew, *Taschenbuch der Mathematik*, Teubner, Leibzig, 1987

[Cam93] M. Campos, *Ablation Rates and Surface Ultrastructure of 193 nm Excimer Laser Keratomies*, Investigative Ophthalmology & Viral Science, 1993

[Can79] J. Canadell, J.L. Beguiristain, *Experimental Scoliosis by Epiphysiodesis of the Neurocentral Cartilage in Pigs*, Journal of Bone Joint Surgery, 61-B:121, 1979

[Cha90] A. Charlton, M.R. Dickinson, T.A. King, A.J. Freemont, *Erbium-YAG and Holumium-YAG Laser Ablation of Bone*, Lasers in Medical Science, 5:365-373, 1990

[Cra88] A.P. Crawley, R.M. Henkelmann, *A comparison of one-shot and recovery methods in T_1 imaging*, Magnetic Resonance in Medicine 7:23-34, 1988

[Cro73] P. Crock, *Befunde zur topographischen und funktionellen Anatomie der intravertebralen Venen*, 1973

[Duc90] F.A. Duck, *Physical properties of tissue*, Academic Press, London, 1990

[Dou83] T.J. Dougherty, *Hematoporphyrin as a photosensitizer of tumors*, Photochemical Photobiology, 38:377, 1983

[Fra00] E. Frank, J. Hollinger, S. Winn, *Endoscopes Integrated into Instruments for Spinal Surgery*, Laser-Tissue Interaction XI: Photochemical, Photothermal, and Photomechanical, Proceedings of SPIE, Vol. 3914, 2000

[Fre98] J. Freyschmidt, H. Ostertag, G. Jundt, *Knochentumoren*, Springer, Berlin, 1998

[Fri00] N.M. Fried, D. Fried, *Laser Ablation of Skull Tissue using Transverse Excited 9.6-μm CO_2 Lasers with Pulse Durations of 1-100 μs*, Proceedings of SPIE, Vol. 3914:128-135, 2000

[Gan98] A. Gangi, J.-L. Dietemann, S. G, L. Vinclair, J. Sibilia, R. Mortazavi, J.P. Steib, C. Roy, *Percutaneous Laser Photocoagulation of Spinal Osteoid Osteomas under CT Guidance*, American Journal of Neuroradiology, 19:1955-1958, 1998

[Gew94] B. Gewiese, J. Beuthan, F. Fobbe, D. Stiller, G. Müller, J. Böse-Landgraf, K.-J. Wolf, M. Deimling, *Magnetic Resonance Imaging-Controlled Laser-Induced Interstitial Thermotherapy*, Investigative Radiology 29:345-351, 1994

[Göt96] M.H. Götz, S.K. Fischer, B.A. Groh, M.H. Ott, S. Gölz, J.F. Bille, *Plasma-mediated ablation of brain tissue in liquid media and application in stereotactic laser neurosurgery*, Proceedings of the SPIE: Laser Interaction with Hard and Soft Tissue, Vienna, 1996

[Göt99] M.H. Götz, S.K. Fischer, A. Velten, J.F. Bille, V. Sturm, *Computer-guided laser probe for ablation of brain tumors with ultrashort laser pulses*, Physics in medicine and biology, 44:119-127, 1999

[Haa39] S.L. Haas, *Experimental Production of Scoliosis*, Journal of Bone Joint Surgery, 21-A:963-969, 1939

[Haa86] A. Haase, J. Frahm, D. Matthai, W. Hänike, K. Merboldt, *FLASH imaging, Rapid NMR imaging using low flip-angle pulses*, Journal of Magnetic Resonance, 67:258, 1996

[Haa90] A. Haase, *Snapshot-FLASH MRI. Applications to T_1, T_2 and chemical shift imaging*, Magnetic Resonance in Medicine, 13:77-89, 1990

[Hac97] K. Hachem, S. Haddad, N. Aoun, J. Tamraz, N. Attalah, *Intérêt De L'IRM Dans Le Diagnostic D'Ostéome Ostéoïde*, Journal de Radiologie, 78:635-641, 1997

[Hah50] E.L. Hahn, *Spin echos*, Physical Review, 80:580, 1950

[Har62] P.R. Harrington, *Treatment of scoliosis: Correlation and internal fixation by spine instrumentation*, Journal of Bone Joint Surgery, 44A:591-610, 1962

[Hei00] A. Heisterkamp, T. Ripken, G. Maatz, H. Lubatschowski, H. Welling, *Intrastromal cutting effects in rabbit cornea using femtosecond laser pulses*, European biomedical optics week (EBIOS), Amsterdam, Netherlands, 2000

[Hel92] J. Helfmann, Nichtlineare Prozesse, in [Ber92], Ecomed, Landsberg/Lech, 1992

[Hon95] J. Honerkamp, H. Römer, *Klassische Theoretische Physik*, Springer, Heidelberg, 1995

[Hor93] W.A. Horton, *Connective tissue and its hertable disorders*, Wiley-Liss, New York, 183-200, 1993

[Iva98] M.M. Ivanenko, P. Hering, *Wet bone ablation with mechanically Q-switched high-repetition-rate CO_2 laser*, Applied Physics B 67:395-397, 1998

[Jak97] P.M. Jakob, C. Hendrich, T. Breitling, A. Schäfer, A. Berden, A. Haase, *Real time monitoring of laser-induced thermal changes in cartilage in vitro by using snapshot FLASH*, Magnetic Resonance in Medicine, 37:805-808, 1997

[Juh94] T. Juhasz, X.H. Hu, T. Laszlo and Z. Bor, *Dynamics of shockwaves and cavitation bubbles generated by picosecond laser pulses in corneal tissue and water*, Laser in Surgery and Medicine 15:91-98, 1994

[Kee93] R.J. Keeman, P.F. Ferson, R.J. Landreneau, S.R. Hazelrigg, *Use of Lasers in Thoracoscopy*, Seminars in Thoracic and Cardiovascular Surgery, 5:294-297, 1993

[Kel96] U. Keller, K.J. Weingarten, F.X. Kertner, D. Kopf, B.Braun, I.D. Jung, R. Fluck, C. Henninger, N. Matuschek, *Semiconductor saturable absorber mirrors (SESAMs) for femtosecond to nanosecond pulse generation in solid-state lasers*, IEEE, Journal of selected Topics in Quantum Electronics (JSTQE), 2:435-453, 1996

[Ker98] J.B. Kerr, *Atlas of Functional Histology*, Mosby, Sydney, 1998

[Keß00] R. Kessler, *Ab-interno Trabekulotomie unter Einsatz verschiedener Kurzpuls-Lasersysteme*, Dissertation, University of Heidelberg, 2000

[Kli96] M. Klingenberg, *Simulation und in-vitro Messungen bei Temperaturerhöhung in Gewebe zur Koagulation bei der laserinduzierten Thermotherapie*, Diploma thesis, University of Heidelberg, 1996

[Kli99] M. Klingenberg, *Entwicklung einer Therapie-Einheit zur volumenkonformen Laserbehandlung von Tumoren*, Dissertation, University of Heidelberg, 1999

[Kne86] F.K. Kneubühl, M.W. Sigrist, *Laser*, Teubner, 1986

[Koe92] W. Koechner, *Solid-State Laser Engineering*, Springer, 1992

[Kre88] E. Krestel, *Bildgebende Systeme für die medizinische Diagnostik*, Siemens AG, 1988

[Kuh98] O. Kuhne, *Photoablation an Hartgewebe*, Diploma thesis, Fachhochschule Aachen, 1998

[Lau72] W. Lauterborn, *High-Speed photography of laser-induced breakdown in liquids*, Applied Physics Letters 21:27-29, 1972

[Lis90] J. Lissner, M. Seiderer, *Klinische Kernspintomographie*, Ferdinand Enke Verlag, 1990

[Lös92] F. Lösel, *Aufbau eines regenerativ verstärkten Nd:YLF-Lasersystems und Entwicklung von Femtosekunden-Laserpulsen in der Neurochirurgie*, Dissertation, University of Heidelberg, 1995

[Lös95] F. Lösel, *Entwicklung von Femtosekunden-Festkörperlasern und erste Anwendungen von Femtosekunden-Laserpulsen in der Neurochirurgie*, Dissertation, University of Heidelberg, 1995

[Lös98] F. Lösel, J.P. Fischer, M.H. Götz, C. Horvath, T. Juhasz, F. Noack, N. Suhm, J.F. Bille, *Non-thermal ablation of neural tissue with femtosecond laser pulses*, Applied Physics B, 66:121-128, 1998

[Lon95] J.E. Lonstein, D.S. Bradford, R.B. Winter, J.W. Ogilvie, *Textbook of Scoliosis and other Spinal Deformities*, W.B. Saunders, 3rd Edition, 309, 1995

[Lub99] H.Lubatschowski, G. Maatz, A. Heisterkamp, H. Welling, W. Ertmer, *Intrastromal refractive surgery by fs laser pulses*, Biomedical Optics: New Concepts in Therapeutic Laser Applications, OSA Technical Digest, 5-7, 1999

[Lun72] J. Lundskog, *Heat and bone tissue. An experimental investigation of the thermal properties of bone and threshold levels for thermal injury*, Scandinavian Journal of Plastic Reconstruction Surgery, suppl.9:1-80, 1972

[Mac96] J.R. MacFall, D.M. Prescott, H.C. Charles, T.V. Samulski, *MRI phase thermometry in vivo in canine brain, muscle, tumor tissue*, Medical Physics, 23:1775-1782, 1996

[Mar63] D.W. Marquardt, *An algorithm for least-square estimation of non linear parameters*, J. Soc. Industr. Appl. Math., 11:431, 1963

[Mes94] C.J. Messer, *Weiterentwicklung einer stereotaktischen Lasersonde*, diploma thesis, University of Heidelberg, 1994

[Mil52] F.A. Miller, C.H. Wilkins, *Infrared spectra and characteristic frequencies of inorganic ions*, Analytical Chemistry, 24:1253-1275, 1952

[Mor95] H. Morneburg, *Bildgebende Systeme für die medizinische Diagnostik*, Publicis MCD Verlag, Erlangen, 1995

[Mor98] P.R. Morrison, F.A. Jolesz, D. Charous, R.V. Mulkern, S.G. Hushek, R. Margolis, M.P. Fried, *MRI of Laser-Induced Interstitial Thermal Injury in an In Vivo Animal Liver Model with Histologic Correlation*, Journal of Magnetic Resonance Imaging, 8:57-63, 1998

[Mül95] G. Müller, A. Roggan (*EDITORS*), *Laser-induced interstitial thermotherapy*, SPIE-The International Society for Optical Engineering, Bellingham, Washington, 1995

[Mül97] I. Müller-Vogt, R. Kessler, S. Gölz, M.H. Götz, J.F. Bille, *Corneagewebe-Ablation durch gepulstes UV-Laserlicht verschiedener Systeme mit einem Scanner in 3 Dimensionen*, DGMP, Hamburg, Germany, 1997

[Mül98] U.G. Müller-Lisse, A.F. Heuck, M. Thoma, R. Mutscher, P. Schneede, E. Weninger, S. Faber, A. Hofstetter, M.F. Reiser, *Predictability of the Size of Laser-Induced Lesions in T_1-Weighted MR Images Obtained During Interstitial Laser-Induced Thermotherapy of Benign Prostatic Hyperplasia*, Journal of Magnetic Resonance Imaging, 8:31-39, 1998

[Mul97] R.V. Mulkern, A.H. Chung, F.A. Jolesz, K. Hynynen, *Temperature monitoring of ultrasonically heated muscle with RARE chemical shift*, Medical Physics, 24:1899-1906, 1997

[New77] H. Newesely, *High temperature behaviour of hydroxy- and fluorapatite*, Journal of Oral Rehabilitation, 4:97-104, 1977

[Nie95] M.H. Niemz, *Threshold dependence of laser-induced optical breakdown on pulse duration*, Applied Physics Letters 66:1181, 1995

[Nie96] M.H. Niemz, *Laser Tissue Interactions*, Springer Verlag Berlin, Heidelberg, New York, 1996

[Nus88] R.C. Nuss, R.L. Fabian, R. Sarkar, C.A. Puliafito, *Infrared Laser Bone Ablation*, Lasers in Surgery and Medicine, 8:381-391, 1988

[Nyq71] R.A. Nyquist, R.O. Kagel, *Infrared spectra of inorganic compounds*, Academic Press, New York, 1971

[O'Co98] J.X. O'Connell, S.S. Nanthakumar, G.P. Nielsen, A.E. Rosenberg, *Osteoid Osteoma: The Uniquely Innervated Bone Tumor*, Modern Pathology, 11:175-180, 1998

[Ols98] J. Olsrud, R. Wirestam, S. Brockstedt, A.M.K. Nilsson, K.-G. Tranberg, F. Ståhlberg, B.R.R. Persson, *MRI thermometry in phantoms by use of the proton resonance frequency shift method: application to interstitial laser thermotherapy*, Physics in Medicine and Biology, 43:2597-2613, 1998

[Pac39] W. Pacher, *Operative Erzeugung einer Skoliose im Tierversuch*, Z. Orthop., 69:140-154, 1939

[Pal97] M. Paley, M. Clemence, M.A. Hall-Craggs, I.D. Wilkinson, W.R. Lees, M.J.G. Harrison, *High magnetic susceptibility coatings for visualisation of optical fibers on a specialised interventional MRI system*, European Radiology, 7:1341-1342, 1997

[Pas96] E.P. Paschalis, O. Jacenko, B. Olsen, B. Decrombrugghe, A.L. Boskey, *The Role of Type X Collagen in Endochondral Ossification as Deduced by Fourier Transform Infrared Microscopy Analysis*, Connective Tissue Research, 35:371-377, 1996

[Pic89] P. Picci, M. Mirra, *Bone tumors - Clinical radiology and paphologic relations*, Lea & Febiger, Philadelphia, London, 1989

[Poh76] R.W. Pohl, *Optik und Atomphysik*, Springer, Berlin, Heidelberg, New York, 1976

[Poo95] J. de Poorter, C. de Wagter, Y. de Denne, C. Thomsen, F. Ståhlberg, E. Achten, *Noninvasive MRI thermometry with the proton resonance frequency (PRF) method: In vivo results in human muscle*, Magnetic Resonance in Medicine, 33:74-81, 1995

[Pul84] C.A. Puliafito, R.F. Steinert, *Short-pulsed Nd:YAG laser microsurgery of the eye: biological considerations*, IEEE Journal of Quantum Electronics 20:1442, 1984

[Rad00] G. Rademaker, K. Baudendistel, M. Bock, L. Schad, *MR-Temperaturverlaufskontrolle mittels schneller diffusionsgewichteter HASTE-Sequenz und Vergleich zu T1 gewichteter FLASH-Sequenz*, DGMP, 2000

[Rad01] G. Rademaker, J. Simiantonakis, C. Rumpf, J. Jenne, R. Rasrert, W. Daecke, L.R. Schad, *Rapid MR Temperature imaging for Control of Focussed Ultrasound (FUS) and Laser induced Thermptherapy (LITT)*, submitted to: International Society of Magnetic Resonance in Medicine (ISMRM), 2001

[Rei90] M. Reiser, *Magnetresonanztomographie*, Springer Verlag, 1990

[Rei98] P. Reimer, C. Bremer, C. Horch, C. Morgenroth, T. Allkemper, G. Schuierer, *MR-Monitored LITT as a Palliative Concept in Patients with High Grade Gliomas: Preliminary Clinical Experience*, Journal of Magnetic Resonance Imaging, 8:240-244, 1998

[Roa60] R. Roaf, *Vertebral Growth and it's Mechanical Control*, Journal of Bone Joint Surgery, 42-B:40-59, 1960

[Rog93] A. Roggan, G. Müller, *Computer simulations for the irradiation planning of LITT*, Medical Technology 4:18-24, 1993

[Roh99] M. Rohwedder, *Konzeption und Aufbau diodengepumpter Festkörperlaser und in-vitro-Gewebeabtragung mit Pikosekunden*, Dissertation, University of Heidelberg, 1999

[Rum98] C. Rumpf, *Anwendung verschiedener Lasersysteme in der Orthopädie*, Diploma thesis, University of Heidelberg, 1998

[Sch90] K.-H. Schönborn, *Lichtwellenleiter*, from "Angewandte Lasermedizin", Ecomed, Landsberg/Lech, 1990

[Sch92] C. Scholz, Umkirch, M. Grovthves-Spork, *Die Bearbeitung von Knochen mit dem Laser*, in [Ber92], 1992

[Sch93] L.R. Schad, W. Semmler, M.V. Knopp, M. Deimling, H.J. Weinmann, W.J. Lorenz, *Preliminary evaluation: Magnetic resonance of urography using a saturation inversion projection spin-echo sequence*, Magnetic resonance imaging, 11:319-327, 1993

[SDB98] B. Schuknecht, W. Daecke, L. Bernd, D. Lange, J. Hoffend, *Erfahrungen mit der intraoperativen Lokalisation von Osteoidosteomen mit einem Szintillationsdetektor*, Aktuelle Traumatologie, 28:105-109, 1998

[Sch98] H.-J. Schwarzmaier, I.V. Yaroslavsky, A.N. Yaroslavsky, V. Fiedler, F. Ulrich, T. Kahn, *Treatment Planning for MRI-Guided Laser-Induced Interstitial Thermotherapy of Brain Tumors- The Role of Blood Perfusion*, Journal of Magnetic Resonance Imaging, 8:121-127, 1998

[Sch99] T.H. Schiebler, W. Schmidt, K. Zilles, *Anatomie*, Springer, 1999

[Sie86] A.E. Siegman, *Lasers*, University Science Books, 1986

[Sli89] C.P. Slichter, *Principles of magnetic resonance*, Springer Series in Solid State Sciences 1, Springer Verlag Berlin, Heidelberg, New York, 1989

[Ste89] D. Stern et. al., *Corneal ablation by nanosecond, picosecond and femtosecond lasers at 532 nm and 625 nm*, Arch. Ophthalmol. 107-587, 1989

[Ste95] B. Stepanow, *Entwicklung einer Methode der Magnet-Resonanz-Tomographie (MRT) zur schnellen Erfassung und Darstellung von Temperaturverteilungen im Gewebe*, Dissertation, University of Heidelberg, 1995

[Stu95] C. Sturesson, S. Andersson-Engels, S. Svanberg, *Numerical model for the temperature increase in surface-applied laser-induced thermotherapy with applications to tumor blood flow estimations*, in [Mül95], pp 157

[Tan76] J.M. Tanner, R.H. Whitehouse, *Clinical longitudinal standards for height, weight, height velocity, weight velocity and stages of puberty*, Arch. Dis. Child, 51:170-179, 1976

[Til89] C.L. Tillotson, A.E. Rosenberg, D.I. Rosenthal, *Controlled thermal injury of bone report of a percutaneous technique using radiofrequency electrode and generator*, Investigation Radiology, 24:888-892, 1989

[Tru95] M. Truppe, W. Freysinger, A. Gunkel, W. Thumfart, *The Artma Virtual Patient: 3D monitoring of endoscopic surgery*, Medicine Meets Virtual Reality II, pp.221, San Diego, 1994

[Vog94] A. Vogel, S. Busch, K. Jungnickel, R. Birngruber, *Mechanisms of intraocular photodisruption with picosecond and nanosecond laser pulses*, Lasers in surgery and medicine, 15:32-43, 1994

[Wei76] K.R. Weishaupt, C.J. Gomer, T.J. Dougherty, *Identification of singulett oxygen as the cytotoxic agent in photoinactivation of a murine tumor*, Cancer Research, 36:2316, 1976

[Wei84] W.S. Weinberg, R. Birngruber, B. Lorenz, *The change in light reflection of the retina during therapeutic laser photocoagulation*, IEEE Journal of quantum electronics, QE20, 1481-1489, 1984

[Whe95] W.H. Whelan, D.R. Wyman, B.C. Wilson, *Investigation of large vessel cooling during interstitial laser heating*, Medical Physics, 22:105-115, 1995

[Wil87] B.C. Wilson, M.S. Patterson, S.T. Flock, *Indirect versus direct techniques for the measurement of the optical properties of tissue*, Photochemistry and Photobiology, 46:601-608, 1987

[Wit24] H. Wittek, *Operative Behandlung der Skoliose*, Zeitschrift für Orthopädische Chirurgie, 44:226-235, 1924

[Wym95] D.R. Wyman, M.W. Whelan, B.C. Wilson, *Investigation of large vessel cooling during interstitial laser heating*, Medical Physics 22, pp105, 1995

[Zie76] K. Zielke, R. Stundat, F. Beaujean, *Ventrale Derotation Spondylodese*, Vorläufiger Ergebnisbericht über 26 operierte Fälle, Archiv der Orthopädischen Unfall-Chirurgie, 85:257, 1976

Publications

Oral presentations

- C. Rumpf, M. Götz, W. Seelig, J.F. Bille, *Bewertung verschiedener Lasersysteme zur Zerstörung von Wachstumsfugen an den Wirbelkörpern*, DPG-Frühjahrstagung, 16.3.-20.3.1998, Konstanz, Germany
- C. Rumpf, *Anwendung verschiedener Lasersysteme in der Orthopädie*, Kichhoff-Institute of Physics, 12.04.1998, Heidelberg, Germany
- C. Rumpf, *Thorakoskopische laserinduzierte Hemiepiphysiodese an der Wirbelsäule*, Stiftung Orthopädische Universitätsklinik, 26.01.2000, Heidelberg, Germany
- C. Rumpf, *Temperaturmessungen während minimal-invasiver Laserapplikation in der Orthopädie und Neurochirurgie*, German Cancer Research Center (DKFZ), 24.02.2000, Heidelberg, Germany
- C. Rumpf, R. Lang, M. Götz, *Minimally-invasive scoliosis treatment with a Ho:YAG laser*, European Biomedical Optics Week 2000, 4. - 8.07.2000, Amsterdam, Holland

Poster presentations

- C. Rumpf, R.D. Lang, F. Becker, N. Henkel, G. Hundt, V. Ewerbeck und J. Bille, *Vergleich vier verschiedener Lasersysteme zur Hemiepiphysiodese an der Wirbelsäule* und *Thorakoskopische laserinduzierte Hemiepiphysiodese an der Wirbelsäule*, Projektpresentation, Stiftung Orthopädie Universitätsklinik, 14.11.1998, Heidelberg, Germany
- C. Rumpf, R.D. Lang, M. Götz, J.F. Bille, *Thorakoskopische laserinduzierte Wachstumsfugenverödung an der Wirbelsäule* , DPG-Frühjahrstagung, 15.-19.4.1999, Heidelberg, Germany
- R.D. Lang, C. Rumpf, *Suitability of different lasers in experimental spinal hemiepiphysiodesis* , XXXIV European Society of surgical research Congress, 21.4.-24.4.1999, Bern, Switzerland
- C. Rumpf, R.D. Lang, N. Henkel, G. Hundt, D. Parsch, *Experimental thoracoscopic hemiepiphysiodesis - first findings*, I^{s}t International Polish-Czech-Slovak Symposium on Videosurgery, 28.04. - 30.04.1999, Ustron, Polland
- C.Rumpf, W. Daecke, M. Götz und J. Bille, *Laserstudie zur minimal-invasiven Behandlung von Osteoid Osteomen*, DPG Frühjahrstagung, 3.-7.4.2000, Bonn, Germany

International Journals

- C.Rumpf, R.D. Lang, M.H. Götz, J.F. Bille, *Evaluation of four different laser systems for a minimally-invasive scoliosis treatment* , IEEE Journal of selected topics in quantum electronics, August 1999
- C.Rumpf, R.D. Lang and M.H. Götz, *Minimally-invasive scoliosis treatment with a Ho:YAG laser*, Proceedings of the SPIE on Laser-Tissue Interaction and Tissue Optics VI, Amsterdam, June 2000
- Paper for publication in veterinarian journal in preparation

Acknowledgements

My thanks go to ...

Prof. Dr. Josef Bille for the possibility to do such an interesting work in the field of medical physics and his great interest in interdisciplinary work in the field of orthopaedics and oncology

Prof. Dr. Wolfgang Schlegel for his interest in this work and his willingness to take on the second referee

Dr. Robert Lang for his great support in all medical and clinical belongings, especially for his skills in endoscopic surgery and the possibility to present our work on an international forum

Dr. Wolfgang Daecke for his support and enthusiasm during the experiments and his contribution to this work

Dr. Marcus Götz for his great support in all sorts of queries throughout the entire work, his ideas, skills and wide knowledge, not only in the field of medical physics

graduate physicist Guido Rademaker for his assistance during the MRI experiments and his knowledge with regard to the temperature measurements, Prof. Dr. Lothar Schad and Prof. Dr. Wolfhard Semmler for their help during the experiments at the German Cancer Research Centre

Sarah Ellis who spent her precious time in reading this dissertation and without whose expertise my English would sound a lot more German

Dr. Werner Rother of Dornier MedTech for the possibility to use the diode laser

Dagmar Gass and Suzanne Wagner for her cooperation during the MRI measurements

Dr. Kristianne Becker for her great assistance and skills during the animal experiments

Dr. Ralf (Ralfik) Keßler for the unforgettable time inside and outside the lab

Dr. Ingo (Pingo) Müller-Vogt for arousing my sports skills and the sweaty mountain bike trips around Heidelberg

Dr. Andreas Velten and the people at MRC systems for their help with the experiments at the laser lab

Naima Henkel for her support during the in vivo experiments

graduate physicist Michael (Schotti) Schottner for his computational skills and knowledge

graduate physicist Karaneh Razavi for the time we shared

graduate physicist Jürgen (vorneweg) Fröhlich for the good laughs and the time outside the lab

graduate physicist Maurizio (Mauri) Daneluzzi and Marc Seemann for the unique Italian coffee breaks

and all people from the lab for the unique working conditions

Brunhild Schagen, Gerhart Buchmann, Dr. Rudolf Büchele and Prof. Burkhard Krempin, for their support with the SEM and histological investigations

Dr. Claus Schulz of the Max-Born institute in Berlin for his hospitality and assistance during the experiments with the fs-laser

and all who contributed to this work and helped to make it possible, especially

my parents who always believed in me and without whose support throughout the entire studies all this would not have been possible.